Deep inelastic scattering off hydrogen and deuterium

Jan Visser

Cover: Photograph by Y.J. Visser van Rietschoten

The work described in this thesis is part of the research program of the 'Stichting voor Fundamenteel Onderzoek der Materie (FOM)', which is financially supported by the 'Nederlands organisatie voor Wetenschappelijk Onderzoek (NWO)'.

RIJKSUNIVERSITEIT GRONINGEN

Deep inelastic scattering off hydrogen and deuterium

Proefschrift

ter verkrijging van het doctoraat in de
Wiskunde en Natuurwetenschappen
aan de Rijksuniversiteit Groningen
op gezag van de
Rector Magnificus, dr. F. Zwarts,
in het openbaar te verdedigen op
vrijdag 20 september 2002
om 14:15 uur

door

Jan Visser

geboren op 5 oktober 1972
te Dordrecht

Promotores:	Prof. dr. G. van der Steenhoven
	Prof. dr. P.K.A. de Witt Huberts
Co-promotor:	Dr. J.J.M. Steijger
Beoordelingscommissie:	Prof. dr. M. Düren
	Prof. dr. M.N. Harakeh
	Prof. dr. J.A. Tjon

CONTENTS

1. INTRODUCTION

When considering very small scales, hadronic matter consists of partons, more specifically quarks and gluons. Clusters of quarks and gluons form the proton and neutron, the constituents of the atomic nucleus. The proton and neutron each consist of three valence quarks and a large number of relatively low momentum quark-anti-quark pairs (the so-called sea quarks), which are held together by the exchange of gluons between the quarks. These gluons are the mediators of the strong force, which is described by Quantum ChromoDynamics (QCD).

When studying the structure of the proton with particles of high energy (larger than 10 GeV) very small length scales are probed: 10^{-16} to 10^{-17}m. At these distance scales the dynamics of the quarks correspond to that of almost free particles, a phenomenon referred to as asymptotic freedom. Because the interactions are relatively weak, QCD can be treated in a perturbative manner (pQCD). At larger distance scales the interactions become considerably stronger and perturbative techniques cease to be applicable. In this non-perturbative domain of QCD, correlations between quarks and gluons emerge and give rise to bound states, i.e. the hadrons.

In order to obtain information on such partonic correlations, we need to carry out precision high energy scattering experiments at somewhat larger distance scales, which correspond to low to intermediate Q^2 values, where the transferred four-momentum squared, Q^2, determines the distance scales probed. When Q^2 is larger the scales probed are smaller.

The experimental tool of choice to study partons and their correlations is Deep Inelastic Scattering (DIS), which corresponds to scattering a lepton off a parton in the nucleon. Partonic correlations are manifest in DIS because additional gluons are exchanged in the scattering process. In the theoretical framework used to describe DIS processes diagrams involving additional gluons are known as higher twist contributions. By carrying out high precision lepton scattering experiments on hydrogen and deuterium one can search for experimental evidence of such higher-twist effects.

The experimental data used to search for such higher-twist effects have been obtained in the HERa MEasurement of Spin (HERMES) experiment, which is based at the Deutsches Elektronen SYnchrotron (DESY) and designed to clarify the spin structure of the nucleon. As the HERMES spectrometer system is optimised to measure cross-section ratios we searched for possible differences in higher twist effects between the proton and the deuteron. In the framework of this thesis, we focus on two specific kinematic regions where possible deviations are most likely to become visible. The differences between the quark distributions in the proton and neutron are most prominent at high x (high fractional momentum of the quark in the nucleon) where valence quarks dominate the quark distribution. Therefore, in this domain one can search for differences between the u and d quark distributions that are possibly related to higher twist effects. To perform these studies one has to investigate the behaviour of the cross-section ratio of deuterium over hydrogen as a function of Q^2. By combining the present data with those of previous measurements, collected a t higher Q^2, one can search with better accuracy for differences between the data and the pQCD calculations, that do not include higher-twist effects.

At low x one can investigate whether higher twist effects can be identified that can be associated with differences in the sea quark distributions of the proton and the deuteron. The search for possible higher-twist effects is performed by measuring the ratio of the longitudinal to transverse DIS cross sections, $R = \sigma_L/\sigma_T$. At high Q^2 values the DIS cross section is purely transverse, leading to $R = 0$, which is also observed experimentally [1], [2]. Deviations from $R = 0$ have been observed on the proton at low Q^2 and low x. These deviations are associated with higher twist effects. The sensitivity for higher twist effects increases at low Q^2, since they are expected to scale with a factor $1/Q^{2n}$ [3], where $n = 1, 2$ stands for the order of twist. The data presented in this thesis are used to investigate whether R^d differs from R^p, which could be indicative of higher-twist effects that are different in hydrogen with respect to deuterium at low x.

To achieve these goals, high statistics DIS data on unpolarised proton and deuteron targets have been collected at HERMES. As compared to earlier high statistics DIS experiments, such as those reported by the New Muon Collaboration (NMC) at the Centre Européenne pour la Recherche Nucléaire (CERN) [1], the average Q^2 is lower. In some cases the data are combined with these NMC data. The resulting large coverage in Q^2 is essential in searching for higher twist effects.

One of the difficulties encountered when trying to extract neutron DIS data from the difference between data collected on proton and deuteron targets is represented by nuclear effects that possibly affect the deuteron data. As a result possible higher-twist effects that are different in the deuteron as compared to the proton, cam either be due to proton-neutron differences or be of nuclear origin. In order to determine 'neutron' data, these nuclear effects need to be accounted for, which is difficult as they cannot be determined unambiguously. A cleaner method to obtain information on DIS neutron data is provided by tagging experiments, where the events occurring on the neutron can be positively identified by detecting the low momentum spectator proton simultaneously. So far, this method has only been explored with low statistics in neutrino-induced experiments on heavy nuclei [4].

In the second part of this thesis the construction and operation of a prototype silicon recoil-detector is described. It was used to perform a first direct tagging measurement of DIS events on the neutron in electron scattering on the deuteron. In practice the observation of a DIS event in the HERMES spectrometer was used to trigger the readout of the recoil detector. The purpose of the prototype detector was to demonstrate the feasibility of operating a silicon recoil-detector very close to an electron scattering target. Using the prototype it has been investigated whether it is indeed possible to tag DIS events on the neutron in deuterium. For that reason it had to be demonstrated that the spectator protons have a momentum distribution which is very close to the momentum distribution as measured in quasi-elastic electron scattering on the deuteron. If the tagging technique has thus been validated, it can be investigated whether the tagged DIS data on the neutron are similar or different from those derived from inclusive measurements, where only the scattered electron is detected. In addition it can be studied whether the neutron to proton DIS cross-section ratio is dependent on the initial momentum of the nucleon in deuterium. This is of interest since a nucleon momentum dependence of the DIS cross section could be at the origin of the EMC-effect [5]. The EMC-effect is the observed nuclear mass dependence of deep inelastic scattering. It is noted that the recoil detector studies presented in this thesis are exploratory because of the rather low statistics obtained. In the future these first results can be improved significantly after the installation of a large recoil detector at HERMES, which is currently under development [6].

The outline of this thesis is as follows. The necessary theoretical background is introduced in chapter 2. The HERMES detector system used in the experiments is briefly described in chapter 3, mainly focusing on the parts crucial for analyses of the type presented in this thesis. The analysis of precise σ^d/σ^p data is the topic of chapter 4 in which the behaviour of the longitudinal and transverse components of the cross section ratio in the deuteron is compared to that in the proton. Also, the results of our search for higher twist effects at low and high x are presented. In chapter 5 the prototype silicon recoil-detector (known as the silicon test counter) is described and first physics results are presented on the nucleon momentum distribution in deuterium obtained in DIS. Also, a first attempt is presented to study the origin of the EMC-effect through the extraction of the structure-function ratio of the tagged neutron data and the proton data. The final part of the thesis contains a summary of the results obtained.

2. THEORETICAL FRAMEWORK

2.1 Introduction

The experiments presented in this thesis are about Deep Inelastic Scattering (DIS). A DIS event is characterised by the high 4-momentum transfer involved when a lepton scatters off a nucleon. The high momentum of the exchanged boson corresponds to short time intervals and to a wavelength, which is small compared to the size of the nucleon. Therefore, the inner structure of the nucleon can be investigated with this type of interaction.

In deep inelastic scattering experiments three different event classes can be distinguished. In each subsequently listed event class the requirements are more restrictive.

- Inclusive events, when only the scattered lepton is identified.
- Semi-inclusive events, when also one or more of the produced hadrons are detected.
- Exclusive events, corresponding to scattering processes in which the target nucleon remains intact or ends up in a lowly excited baryon resonance state; experimentally, it is required that both the scattered lepton and all produced particles are detected (or indirectly reconstructed).

In this thesis the emphasis is on inclusive measurements on hydrogen and deuterium. The analysis of such data is presented in chapter 4. In chapter 5, although of a more technical character, also some semi-inclusive data are presented. However, once more the emphasis is on inclusive DIS events as the additional hadron observed in these data is actually used as a 'tag' of the inclusive event, i.e. to identify whether the DIS event involved a proton or a neutron in deuterium. In true semi-inclusive events, on the contrary, the additional hadron serves as a tag of the quark flavours involved.

The present chapter provides the theoretical framework needed for the discussion of the experimental results presented in chapters 4 and 5. The remainder of this chapter is organised as follows. In the next two sections the DIS kinematics and cross-section formalism is described. The Quark

Parton Model (QPM) is introduced in section 2.4, to provide an intuitive interpretation of the DIS observables. In section 2.5 it is shown how Quantum ChromoDynamics (QCD), the theory of the strong interaction, can be used to relate DIS observables in different kinematic regions. Following this general introduction of the DIS formalism, some specific aspects of DIS are presented, which are relevant for the analysis of the inclusive DIS cross section ratio σ^d/σ^p, presented in chapters 4 and 5. In section 2.6 the Gottfried sum rule is introduced, which provides information on possible differences between the sea-quark distribution in the proton and the neutron. The measurements of tagged neutron DIS events, presented in chapter 5 are motivated in section 2.7. As these tagged structure-function measurements may have a bearing on the nuclear effects observed in DIS, i.e. the EMC-effect, the last section gives a short description of these effects.

2.2 DIS kinematics

A schematic view of a DIS event in the laboratory system is shown in figure 2.1. This diagram serves to illustrate the kinematics of a DIS event, which involves the coupling of a virtual photon to a parton in the nucleon, and to introduce the key parameters. The relevant observables are the energy of

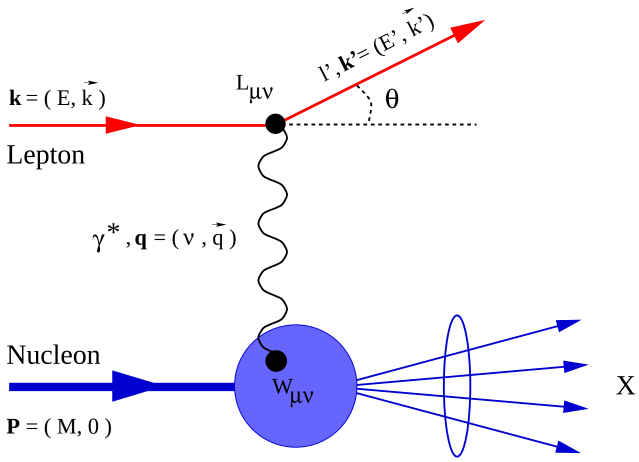

Fig. 2.1: Schematic view of a DIS event in the laboratory system.

the scattered lepton E' and the lepton scattering angle θ. Starting from the measured values of E' and θ, and the precisely known beam energy ($E =$ 27.55 GeV) several quantities can be calculated in the laboratory frame. Note that all equations are given in the laboratory frame. The energy transfer of the lepton to the target is given by $\nu = E - E'$, which can be associated with the energy of the virtual photon γ^*. The squared four-momentum of the virtual photon is given by $Q^2 = 4EE'\sin^2(\theta/2)$. The value of Q^2 is a measure of the inverse of the wavelength of the virtual photon. When Q^2 gets larger the spatial resolution increases and smaller objects are probed in the scattering process. Given these basic quantities, the invariant variable W, as well as dimensionless quantities such as x and y can be defined. These quantities are listed below accompanied by a short explanation, with M the mass of the nucleon and m mass of the incident lepton, which is set to zero for these expressions.

- $x = \frac{Q^2}{2M\nu}$, the nucleon momentum fraction carried by the struck parton, which is a measure of the inelasticity of reactions: the smaller x, the higher the inelasticity;
- $y = \frac{\nu}{E}$, the fraction of the beam energy carried by the virtual photon (relative energy transfer);
- $W^2 = M^2 + 2M\nu - Q^2$, the total invariant mass squared of the virtual photon-nucleon system.

For the study of inclusive DIS in general it suffices to investigate the x and Q^2 dependences of the cross-section data, with certain restrictions imposed on y and W^2.

2.3 DIS cross section

The DIS cross-section formalism is presented in this section. As a starting point the most general way to describe the DIS cross section is given[1]

$$\mathrm{d}\sigma \sim L_{\mu\nu} W^{\mu\nu}. \tag{2.1}$$

In this equation $L_{\mu\nu}$ represents the lepton tensor and $W^{\mu\nu}$ the hadronic tensor. $L_{\mu\nu}$ describes the lepton virtual-photon vertex, which can be calculated in the framework of Quantum ElectroDynamics (QED), and has the following mathematical appearance, when summed and averaged over the spins:

$$L_{\mu\nu} = 2(k'_\mu k_\nu + k'_\nu k_\mu - (k' \cdot k - m^2) g_{\mu\nu}), \tag{2.2}$$

[1] The presentation follows the DIS formalism of Halzen & Martin, Chapters 6 and 8 from ‘Quarks & Leptons: An Introductory Course in Modern Particle Phyics’ (John Wiley and sons, New York, 1984).

where k and k' represent the four-momentum vector of the incident and outgoing lepton, m the mass of the lepton, and $g_{\mu\nu}$ the metric tensor. The hadronic tensor $W^{\mu\nu}$ is related to the interaction of the virtual photon and the target nucleon. As it is not possible to calculate $W^{\mu\nu}$ from first principles, information on the hadronic structure is usually obtained through fits of the data in a QCD framework or by means of model calculations. The hadronic tensor $W^{\mu\nu}$ can be written as:

$$W^{\mu\nu} = W_1 \left(-g^{\mu\nu} + \frac{q^\mu q^\nu}{q^2} \right) + W_2 \frac{1}{M^2} \left(p^\mu - \frac{p \cdot q}{q^2} q^\mu \right) \left(p^\nu - \frac{p \cdot q}{q^2} q^\nu \right). \quad (2.3)$$

The target four-momentum vector is given by $p = (M; 0, 0, 0)$, while $q = (\nu; 0, 0, \sqrt{\nu^2 - q^2})$ is the four-momentum vector of the virtual photon and W_1 and W_2 are two independent inelastic scalar structure functions.

These two structure functions remain from the four that appear in the most general expression for $W^{\mu\nu}$, when requiring current conservation at the hadronic vertex. Relation 2.3 has been written in a simplified manner by neglecting the dependence of W_1 and W_2 on ν and Q^2. Furthermore, the anti-symmetric contributions have been omitted, as they would vanish when contracted with the symmetric lepton tensor. Also the above expression is already summed and averaged over the spins. When performing the contraction of the lepton tensor and the hadronic tensor, as indicated by equation 2.1, using the expressions of $L_{\mu\nu}$ and $W^{\mu\nu}$ given by equations 2.2 and 2.3 respectively, one obtains a relation for the DIS cross section, which consists of two independent components:

$$\left. \frac{d\sigma}{dE' d\Omega} \right]_{lab} = \frac{\alpha^2}{4E^2 \sin^4 \frac{\theta}{2}} \left\{ W_2(\nu, q^2) \cos^2 \frac{\theta}{2} + 2W_1(\nu, q^2) \sin^2 \frac{\theta}{2} \right\}. \quad (2.4)$$

The structure functions W_1 and W_2 can be rewritten in two other independent components, which are the longitudinal (σ_L) and transverse (σ_T) virtual-photon absorption cross sections. They are investigated separately in chapter 4. Intuitively the scattering of the longitudinally oriented virtual photons can be interpreted as a charge-like interaction with a parton in the nucleon, while reactions involving transversely oriented virtual photons can be visualised as corresponding to a spin flip of the struck parton. In order to clarify the difference between the longitudinal and transverse cross-section components it is necessary to develop the DIS formalism further such that it can be shown how (σ_L) and (σ_T) are related to measurable quantities. For this purpose it is important to realise that the lepton tensor can also be expressed as a function of the polarisation vectors ϵ_λ^μ of the virtual photon. The vectors ϵ_λ^μ depend on the helicity state, labelled by the subscript λ, of the virtual photon. Four different states can be identified: two transverse states ($\lambda = \pm 1$), a longitudinal state (λ=0), and a scalar state (λ=0). Since the scalar and longitudinal states are at all times related three independent polarisation states are left. For the different helicity states λ, the polarisation vectors ϵ^μ_λ of the virtual photon are defined in the following way:

$$\lambda = \pm 1: \qquad \epsilon_\pm = \mp\sqrt{\frac{1}{2}}(0; 1, \pm i, 0), \tag{2.5}$$

$$\lambda = 0: \qquad \epsilon_0 = \frac{1}{\sqrt{-q^2}}(\sqrt{-\nu^2 - q^2}; 0, 0, \nu), \tag{2.6}$$

with the z-axis chosen along $\vec{q}$. Using the photon polarisation vectors the total DIS cross section for the interaction of virtual photons of polarisation state (λ) takes the following appearance:

$$\sigma^{tot}_\lambda = \frac{4\pi^2\alpha}{K}\epsilon^{\mu *}_\lambda \epsilon^\nu_\lambda W_{\mu\nu}, \tag{2.7}$$

with K a normalisation factor. For real photons only the two transverse states remain. In that case the photon flux factor is given by $4MK$, with $K = \nu$. However, in the case of virtual photons this flux factor is not uniquely defined and a definition for K has to be chosen, with $K = \nu$ as the limit at $Q^2 = 0$. In the Hand convention this becomes:

$$K = \frac{W^2 - M^2}{2M} = \nu + \frac{q^2}{2M}. \tag{2.8}$$

When one inserts the polarisation vectors ϵ^μ_λ from equations 2.5 and 2.6 and $W^{\mu\nu}$ from equation 2.3 into equation 2.7 one can extract expressions for the cross-section components, which are accessible experimentally (although not directly): the transverse and longitudinal cross sections.

$$\sigma_T \equiv \frac{1}{2}(\sigma^{tot}_+ + \sigma^{tot}_-) = \frac{4\pi^2\alpha}{K}W_1(\nu, q^2), \tag{2.9}$$

$$\sigma_L \equiv \sigma^{tot}_0 = \frac{4\pi^2\alpha}{K}\left[\left(1 - \frac{\nu^2}{q^2}\right)W_2(\nu, q^2) - W_1(\nu, q^2)\right]. \tag{2.10}$$

In order to relate σ_T and σ_L to the total inclusive DIS cross section we need to combine equation 2.4 with 2.5 and 2.6. When replacing W_1 and W_2 by expressions involving σ_T and σ_L one obtains:

$$\left.\frac{d\sigma}{dE' d\Omega}\right]_{lab} = \Gamma(\sigma_T + \epsilon\sigma_L), \tag{2.11}$$

where

$$\Gamma = \frac{\alpha K}{2\pi^2 |q^2|} \frac{E'}{E} \frac{1}{1-\epsilon} \tag{2.12}$$

and

$$\epsilon = \left(1 - 2\frac{\nu^2 - q^2}{q^2} \tan^2 \frac{\theta}{2}\right)^{-1}. \tag{2.13}$$

The direct way to obtain information on σ_L and σ_T is to use the Rosenbluth separation method. It is based on measurements of the DIS cross section at various beam energies at the same value of x and Q^2, and hence at different values of ϵ. Two (or more) cross section measurements at different values of ϵ make it possible to extract values of σ_T and σ_L using equation 2.11. In chapter 4 examples are given of determinations of the value of σ_T and σ_L (for deuterium relative to hydrogen). Often the results of longitudinal-transverse cross section separations are expressed in terms of the ratio R:

$$R = \sigma_L / \sigma_T. \tag{2.14}$$

The quantity R can also be used to compare L-T separated results for DIS on hydrogen and deuterium. The method used in this thesis to determine R^d/R^p, σ_L^d/σ_L^p, and σ_T^d/σ_T^p from the HERMES data is explained in chapter 4.

2.4 Quark parton model

The discovery of hard point-like scattering centres in the nucleon came about when the scattering cross section at large angles was found to be much larger than expected, much like the discovery of the nucleus by Rutherford. Simultaneously it was found that the cross section at fixed x does not strongly depend on Q^2. This behaviour was interpreted by Björken and is known as Björken scaling. Considering these discoveries, the two independent inelastic scalar structure functions, W_1 and W_2, can be reformulated in terms of two independent structure functions F_1 and F_2:

$$F_1 = MW_1(\nu, Q^2), \tag{2.15}$$

$$F_2 = \nu W_2(\nu, Q^2). \tag{2.16}$$

Based on these expressions for F_1 and F_2, we can derive the following expression for R

$$R(x, Q^2) = (1+\gamma^2)\frac{F_2(x, Q^2)}{2xF_1(x, Q^2)} - 1 \tag{2.17}$$

with

$$\gamma^2 = \frac{Q^2}{\nu^2} = \frac{4M^2x^2}{Q^2}. \tag{2.18}$$

This framework seems to imply the existence of point-like scattering centres in the nucleon, which were associated with the partons proposed by Gell-Mann to explain hadron spectroscopy data. This led to the Quark-Parton Model (QPM) in which the partons are viewed in the following manner. In the nucleon rest frame the partons are tightly bound, so no free partons can be observed. However, in the Lorentz frame, in which the nucleon has very large momentum the lifetime of the virtual partons can become large through time dilation. Hence, the partons 'seen' by a photon with large Q^2 appear to be quasi free. It is further assumed that the total cross section is the sum of the incoherent scattering cross sections of the individual partons.

As the structure functions $F_{1,2}$ are related to $W_{1,2}$ it is possible to relate $F_{1,2}$ to σ_T and σ_L as well. In the discussion below, we use the DIS limit, ($E \gg E'$, $\nu \gg Q^2$) to simplify the resulting equations. In this manner we can obtain the following equations:

$$\sigma_T = 2\sigma_0 F_1 \tag{2.19}$$

and

$$\sigma_L = 2\sigma_0 \left(\frac{F_2}{2x} - F_1 \right) \tag{2.20}$$

with

$$\sigma_0 \equiv \frac{4\pi^2 \alpha}{2MK}. \tag{2.21}$$

In the same DIS limit the following expression for R is obtained, which corresponds to eq. 2.17.

$$R \equiv \frac{\sigma_L}{\sigma_T} = \frac{F_2}{2xF_1} - 1. \tag{2.22}$$

In the quark-parton model DIS events are associated with a spin flip of the struck quark, which corresponds to an exclusively transverse cross section. As $\sigma_L = 0$ in this framework, the quark-parton model assumes $R = 0$ and this leads to the following relation:

$$2xF_1(x) = F_2(x), \tag{2.23}$$

which is known as the Callan-Gross relation [7]. Equation 2.23 turns out to be a consequence of the assumption that the partons are spin 1/2 particles (fermions). In fact, if partons would have been spin 0 particles (bosons), no spin flip could occur when struck by a virtual photon, implying that W_1 and hence F_1 would vanish, thus violating the Callan-Gross relation. When it was shown that equation 2.23 is satisfied by the experimental data [8], the partons were identified as the quarks described in the quark-parton model. It should be realised though that the quark-parton model does not hold exactly, since $R \neq 0$ at small values of x and Q^2 due to higher twist effects, discussed in the next subsection.

The structure functions F_1 and F_2 can be given the following physical interpretation as a function of x, where x can be identified with the fractional momentum of the struck quark in the nucleon. In the expressions below e_i is the electric charge of the quarks (e_u^2=4/9 and e_d^2=1/9).

$$F_1(x) = \frac{1}{2}\sum_i e_i^2 q_i(x), \tag{2.24}$$

$$F_2(x) = \sum_i e_i^2 x q_i(x), \tag{2.25}$$

where $F_1(x)$ is the incoherent sum of the individual quark momentum distributions, $q_i(x)$, for quarks of flavour i. This sum represents the total parton density distribution or structure function $F_1(x)$, while the sum weighted with the parton momentum fraction, x, is known as the structure function $F_2(x)$.

2.5 Quantum chromodynamics

The theory which provides us with a precise description of the strong interaction at high energies is Quantum ChromoDynamics (QCD). One of the major successes of QCD is its ability to precisely describe the experimentally obtained deviations from the Q^2 independence of the DIS data, which are also known as scaling violations. In order to achieve such a precise description of the DIS structure functions over a large range of Q^2 a perturbative approach in QCD is used. It is noted that the QCD framework cannot be used to calculate the structure functions from first principles, as this would require a non-perturbative approach, which is not yet possible. Instead an accurate measurement at one Q^2 value is needed as a starting point. One can use perturbative QCD (pQCD) to evolve, e.g., a structure function from one Q^2 to any other Q^2 (both larger than 1 GeV^2), this is known as Q^2 evolution. The equations developed in the pQCD framework to perform the Q^2 evolution are the so-called DGLAP [9] equations for the quark and gluon distribution functions $q(x, Q^2)$ and $g(x, Q^2)$, which in leading order are written as:

$$\frac{\mathrm{d}q_i(x,Q^2)}{\mathrm{d}\ln Q^2} = \frac{\alpha_s}{2\pi}\int_x^1 \frac{\mathrm{d}y}{y}\Big(q_i(y,Q^2)P_{qq}\Big(\frac{x}{y}\Big) + g(y,Q^2)P_{qg}\Big(\frac{x}{y}\Big)\Big), \tag{2.26}$$

$$\frac{\mathrm{d}g(x,Q^2)}{\mathrm{d}\ln Q^2} = \frac{\alpha_s}{2\pi}\int_x^1 \frac{\mathrm{d}y}{y}\Big(\sum_{q_i} q_i(y,Q^2)P_{gq}\Big(\frac{x}{y}\Big) + g(y,Q^2)P_{gg}\Big(\frac{x}{y}\Big)\Big), \tag{2.27}$$

where α_s is the strong coupling constant and the contribution from the splitting of gluons into quarks is given by:

$$P_{g\to q}\Big(\frac{x}{y}\Big) \equiv P_{qg}\Big(\frac{x}{y}\Big) \tag{2.28}$$

and $\mathrm{P}_{qq}\big(\frac{x}{y}\big)$,$\mathrm{P}_{gq}\big(\frac{x}{y}\big)$, and $\mathrm{P}_{gg}\big(\frac{x}{y}\big)$ are defined accordingly.

The pQCD calculations of cross sections are based on Parton Distribution Functions (PDF's) which are extracted from the currently available high energy scattering data. The main component of the calculated cross section is obtained from leading order $(1/Q^2)$ calculations. In addition to these terms next to leading order (NLO $(1/Q^4)$) terms and NNLO $(1/Q^6)$ terms can be included. This is done by expanding the splitting functions presented in equation 2.28. With the calculations in NLO and NNLO more diagrams that contribute to the hard (parton level) scattering process are included. Apart from refined calculations of the hard scattering, one can also investigate additional contributions to the hadronic (soft) part of the scattering process. These so-called higher twist effects include diagrams with, e.g., more gluon lines, which complicate the process. As the soft part cannot be calculated in a perturbative approach, it is consequently described with phenomenological models which are also based on $(1/Q^{2n})$ terms, where n represents the order of twist of the included term. Experimentally it is difficult to distinguish between higher order NLO and NNLO terms and contributions due to e.g. quark-gluon correlations, i.e. higher twist effects. Initially higher twist effects were found to be significant at high x, but the inclusion of NLO and NNLO effects in the leading twist calculations reduced the experimentally determined size of the higher twist terms on the proton [10]. The remaining question is whether the same result can be found when searching for higher twist effects in the ratios such as R^d/R^p and F_2^d/F_2^p, which are potentially less sensitive to NLO and NNLO effects. These ideas will be explored in section 4.6.3 and 4.7.

2.6 Gottfried sum rule

Besides the structure function ratio F_2^n/F_2^p, also the difference of these structure functions is of interest. The integral of this difference over x, known as the Gottfried sum rule, is written as:

$$S_0 = \int_0^1 \frac{1}{x}(F_2^p(x) - F_2^n(x))\mathrm{d}x \tag{2.29}$$

$$= \frac{1}{3} + \frac{2}{3}\int_0^1 (\mathrm{u}_s(x) - \mathrm{d}_s(x))\mathrm{d}x. \tag{2.30}$$

The second equation follows from the first under the assumption of iso spin symmetry between the proton and neutron ($u_v^p = d_v^n, d_v^p = u_v^n, u_s = u_s^p = \overline{u}_s^p = d_s^n = \overline{d}_s^n$ and $d_s = d_s^p = \overline{d}_s^p = u_s^n = \overline{u}_s^n$), where the subscripts refer to the valence (v) and sea (s) quark distributions. The contribution of the strange quarks is assumed to be the same for the proton and the neutron. Experimentally the Gottfried sum rule was determined by NMC [1] and a value of $S_0 = 0.2281 \pm 0.0065$ (stat.) was found. This measurement indicates that the light quark sea is flavour asymmetric and that $u_s < d_s$ in the investigated Q^2-range. With the data presented in chapter 4 it will be possible to derive a new value of S_0 at an - on average - somewhat lower Q^2 value.

2.7 The structure function ratio F_2^n/F_2^p

The structure function F_2 can be interpreted as the momentum-weighted quark distribution within the nucleon. As there are two different nucleons, the proton and the neutron, it is interesting to see how the ratio of F_2^n/F_2^p behaves. At low x the ratio is expected to be close to unity as this region is dominated by sea quarks (i.e. quark-anti-quark pairs of any flavour) and there are no indications to assume a different behaviour when comparing the sea quarks of the proton and the neutron.

However, at high x the sensitivity of F_2^n/F_2^p shifts from the sea to the valence quarks. For the high x region there are several predictions for the behaviour of F_2^n/F_2^p when $x \to 1$. When exact $SU(6)$ symmetry is assumed, the u and d quarks would be identical and only the difference in charge would be responsible for a deviation of F_2^n/F_2^p from unity at $x \to 1$. Therefore, the prediction of $SU(6)$ for $F_2^n/F_2^p = \frac{2}{3}$. However, in nature spin-flavour $SU(6)$ symmetry is broken; the mass of the u and d quark are different and so are their momentum distributions. One explanation for the breaking of $SU(6)$ symmetry is the suppression of the "diquark" configuration having $S = 1$ relative to $S = 0$ [11, 12]. This is understood because the $S = 1$ state is believed to have a higher energy than the $S = 0$ state [13]. When this $S = 0$ scalar state is dominant, in the limit $x \to 1$, F_2 is essentially given by a single quark distribution, i.e. the u-quark in case of the proton and the d-quark in the neutron case. In this case:

$$\frac{F_2^n}{F_2^p} \to \frac{1}{4} \qquad \text{[S = 0 dominant].} \tag{2.31}$$

An alternative prediction, based on perturbative QCD [14], argues that the relevant component of the proton valence wave function at large x is associated with states in which the total "diquark" spin projection S_z is zero.

Consequently, scattering from a quark polarised anti-aligned with the proton spin is suppressed by a factor $(1-x)$ relative to the helicity-aligned configuration. This leads to a prediction of:

$$\frac{F_2^n}{F_2^p} \to \frac{3}{7} \qquad [\mathrm{S_z} = 0 \text{ dominant}]. \tag{2.32}$$

A similar result was reached by Brodsky et al. [15] using counting rules. Melnitchouk and Thomas [16], in their model, have taken into account also Fermi motion, binding and nucleon off-shell effects in the deuteron to predict a value for F_2^n/F_2^p of also $\sim 3/7$ in the limit of $x \to 1$. The re-analysis of the

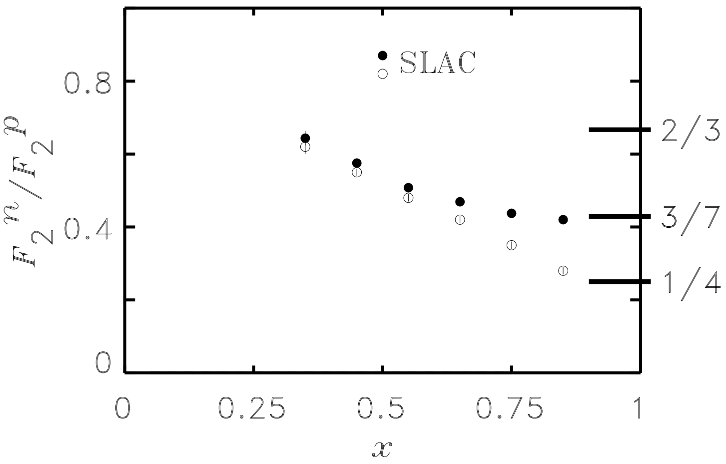

Fig. 2.2: Analysis of SLAC F_2^n/F_2^p data with (full circles) and without (open circles) a correction for off-shell effects [16], compared with the predictions discussed in the text.

SLAC proton and deuteron data, corrected for these effects, seem to confirm their model as shown in figure 2.2. In this figure two analyses are shown of the F_2^n/F_2^p ratio extracted from the SLAC proton and deuteron data, at an average $Q^2 \approx 12$ GeV^2. The results represented by the open circles do not include a correction for off-shell effects, while the full circles represent the results of an analysis including a correction for off-shell effects. The results of this analysis seem to prefer the pQCD prediction of 3/7, but this result is model dependent and relies on an insecure extrapolation to $x \to 1$. Hence, no unambiguous value for F_2^n/F_2^p at $x \to 1$ exist to date. One of the reasons is that so far F_2^n has not been measured directly in DIS. Instead, F_2^n has always been extracted from F_2^d and F_2^p data using

$$F_2^n/F_2^p = 2\frac{\sigma^d}{\sigma^p} - 1, \tag{2.33}$$

which is an approximation of the real value of F_2^n, as possible nuclear corrections are ignored and it is assumed that $R^d = R^p$. In this thesis F_2^n/F_2^p is extracted directly from the σ^d and σ^p data using equation 2.33, ignoring possible off-shell effects and nuclear corrections at high x. In this way model-independent experimental data are provided, which can be compared to, e.g., the results of NMC. Moreover, values of F_2^n/F_2^p are extracted based on a fitting procedure, which allows for $R^d \neq R^p$. In conjunction with F_2^n/F_2^p, information on $R = \sigma_L/\sigma_T$ is obtained from the fitting procedure, as either the value of R^d/R^p or $\Delta R = R^d - R^p$ is used as a second free parameter. The method used is described in chapter 4. The new data on F_2^n/F_2^p presented in this thesis cover the same x-range as previous data, but on average at Q^2 values, which are a factor of five smaller than those covered by NMC [1]. Moreover, the fitting procedure provides data for R^d/R^p in a kinematic region at low x and low Q^2, where little or no data exist so far.

Whereas the data presented in chapter 4 are not constrained by any requirements on R, it is still assumed that nuclear corrections in deuterium can be neglected. In order to avoid the ambiguities introduced by applying nuclear corrections an alternative method to obtain data on F_2^n is presented in chapter 5. The method is based on the use of a recoil detector, of which a prototype has been developed. A recoil detector enables a direct measurement of F_2^n, by tagging DIS events on a neutron in a deuterium target. The recoil detector identifies the recoil protons originating from the target. They can be detected in coincidence with the DIS lepton. A positive identification of a recoil proton in a DIS event indicates that the scattering process took place on the neutron in the deuteron and that F_2^n is being probed directly. In order to distinguish data obtained in the usual fashion from those obtained by means of a recoil detector, the latter are referred to as $F_2^n\rfloor_{tag}$. In chapter 5 it will be shown that recoil detection in the vicinity of an intense electron beam is possible amd low statistics data for $F_2^n\rfloor_{tag}/F_2^p$ are presented.

2.8 Nuclear effects in DIS

When conducting DIS experiments it was initially thought not to really matter which nuclear target was used. As the energy scale of DIS interactions (GeV) is much larger than the energy scale of nuclear processes (MeV), no interference was expected. Therefore, it came as a surprise when the EMC experiment discovered a dependence of F_2 on the target nucleus in 1982 [5]. The EMC data indicate that the nucleon structure functions are affected by the nuclear environment. The partonic distributions are apparently modified inside the nucleus in such a way that the ratio of nuclear and deuteron structure functions, $R_A = F_2^A/F_2^D$, deviates from unity. The data, of which examples are shown in figures 2.4 and 2.3, exhibit an oscillatory behaviour with respect to $R_A = 1$. In the region of 0.3< x <0.8 we find the original EMC

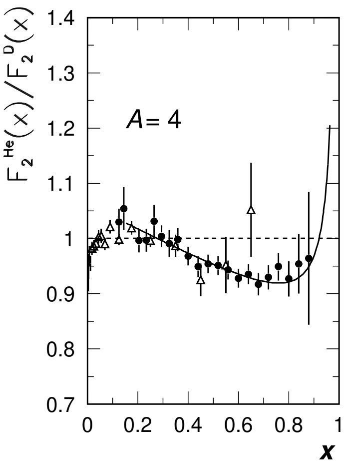

Fig. 2.3: EMC effect as measured on helium [17]. The data are from NMC (filled circles) [18] and SLAC [19] (open triangles).

effect, where $R_A < 1$, which is usually attributed to nucleon dynamics in the nucleus. For $x < 0.1$ another region is found where $R_A < 1$, which is known as the shadowing region. One explains shadowing as a reduction of the DIS cross section in nuclei (A >2) due to coherent strong interactions of hadronic components of the virtual photon with the nucleon in the nucleus. As the interaction is strong, surface nucleons in the target nucleus shadow other nucleons. The region in between the two aforementioned regions is known as the anti-shadowing region, where R_A is slightly larger than unity. The DIS cross section can be expressed in terms of F_2 and $R = \sigma_L/\sigma_T$. As F_2^A/F_2^D deviates from unity it is of interest to investigate whether $R = \sigma_L/\sigma_T$ is also different for various target materials. A possible A-dependence of R could be related to the modification of the gluon distribution in nuclei or meson-exchange contributions to DIS. However, most existing data have not revealed any A-dependence of R. Only recently a deviation from unity was reported by HERMES for $\sigma_L/\sigma_T\rfloor_A$ / $\sigma_L/\sigma_T\rfloor_D$ at $x < 0.06$ and Q^2 < 1.5 GeV/c on ^{3}He and ^{14}N [20]. However, further measurements on heavier targets revealed that the deviation was due to a peculiar detector inefficiency caused by radiated photons in the electron scattering process. Bremsstrahlung photons can be radiated in various directions, but the ones radiated along q have a large probability of hitting detector frames in the mentioned kinematic region, thereby creating showers and very high multiplicity events, which were

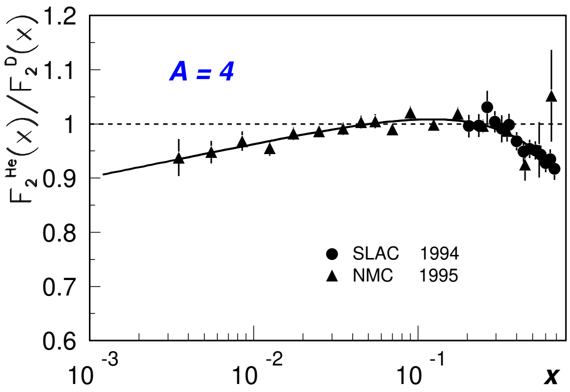

Fig. 2.4: Shadowing region shown for helium [17], data same as above except for the logarithmic scale.

rejected for analysis. This effect is further discussed in section 4.3.4 as the present data were collected using the same equipment. Nonetheless, it is important to search for possible remaining differences in σ_L/σ_T between the proton and the deuteron, as the data presented in chapter 4 partly cover an (x, Q^2) domain where no previous data on $\sigma_L/\sigma_T\rfloor_d / \sigma_L/\sigma_T\rfloor_p$ are available. In this respect it is important to note that the A-dependence of R enters many DIS analyses.

Among the various explanations of the EMC effect it has often been argued that the EMC-effect could be associated with the momentum of the parent nucleon in the nucleus. If this is true the EMC effect can also be observed on deuterium if the momentum dependence of $F_2(x)$ is measured. As an interesting by-product of the first physics analysis obtained with the prototype recoil detector presented in chapter 5, we have studied the momentum depndence of $F_2^n\rfloor_{tag}/F_2^p$ as well. Such data will be presented in chapter 5 for the first time.

3. THE HERMES EXPERIMENT

3.1 Introduction

The HERMES (HERa MEasurement of Spin) experiment [21] is based at the German Institute for high-energy physics DESY (Deutsches Elektron SYnchrotron) in Hamburg. The main objective of the HERMES experiment is the study of the spin structure of the nucleon by means of deep inelastic lepton scattering off nucleon targets. The sensitivity to the spin arises from the use of the polarised lepton beam of HERA and polarised target nuclei.

At HERMES the beam is passing through an open-ended storage cell, in which either polarised or unpolarised gases are injected. The particles emerging from the target are detected in a forward-angle spectrometer, consisting of several tracking and particle identification detectors. In this chapter the HERMES experimental set-up is briefly discussed, focusing on the features important for the analyses described in chapters 4 and 5 of this thesis. For further details we refer to the article [22] in which the HERMES spectrometer is described.

3.2 The HERA storage ring

In the HERA (Hadron Elektron Ring Anlage) storage ring protons and electrons are stored and both beams can be used simultaneously by four different experiments. Two of these experiments, ZEUS and H1, are colliding-beam experiments. HERA-B uses only the proton beam whereas HERMES only uses the polarised lepton beam.

The lepton beam is accelerated to an energy of 27.5 GeV, reaching intensities (at injection) of at most 50 mA. The typical lifetime of the beam is 10 hours. The beam is usually dumped at 10 mA. The lepton beam is transversely polarised by the Sokolov-Ternov effect [23]. In this process, the leptons predominantly align their spins in the vertical direction, parallel to the magnetic field of the storage ring, by radiating photons. However, for the study of the helicity structure of the nucleon a longitudinally polarised beam is required, i.e. the lepton spins have to be aligned parallel to their propagation direction. Therefore, spin rotators are placed before the HERMES experiment. These devices rotate the spin of the electrons from the transverse to the longitudinal orientation. As the Sokolov-Ternov effect [23] aligns the lepton spins in the vertical direction, spin rotators are placed behind the HERMES experiment to rotate the spin of the electrons from the longitudinal orientation back to the transverse one, otherwise it would not be possible for the polarisation to be built up.

3.3 The HERMES target

The target consists of a windowless storage cell in which a gas can be injected. In this way a gas density is reached of $\sim 10^{14} \mathcal{N}\mathrm{cm}^{-2}$, which is two orders of magnitude higher than can be obtained with a gas jet target [24] ($\sim 10^{12} \mathcal{N}\mathrm{cm}^{-2}$).

To limit the influence of the target gas on the beam lifetime a powerful pumping system is used. The gas is pumped away at both ends of the target-cell. The cell, with an elliptically shaped cross section, is 29 mm wide, 9.8 mm high and 40 cm long. Polarised gases can be injected from an Atomic Beam Source (ABS) [25]. The polarisation of the target atoms is measured by a Breit-Rabi polarimeter (BRP) [26]. Unpolarised gases can also be injected into the target cell through a separate capillary near the ABS outlet. In this way target densities of about 10^{15} $\mathcal{N}\mathrm{cm}^{-2}$ have been reached with a contribution to the lifetime of the beam of only 45 hours, for hydrogen and deuterium [1].

3.4 The HERMES spectrometer

The HERMES spectrometer is a forward-angle spectrometer located in the East Hall of the HERA accelerator complex. It is a general purpose instrument that is used to track and identify both the scattered lepton and the produced hadrons. It has a box acceptance, which ranges from 40 mrad to 140 mrad in the vertical direction, both above and below the beam-line, and from -170 mrad to +170 mrad in the horizontal direction. The possible scattering angles range from 40 mrad to 220 mrad. The layout of the spectrometer is illustrated in figure 3.1. The various components of the spectrometer, the trigger system and the data-acquisition system are discussed in separate subsections below.

[1] Unpolarised gas densities in access of 10^{16} $\mathcal{N}\mathrm{cm}^{-2}$ have also been used at HERMES. In this case the beam lifetime is reduced to a few hours.

3.4.1 Spectrometer magnet

In combination with the tracking system the magnet is used to determine the momentum of the particles. The spectrometer magnet is of the H-frame type with a deflecting power of 1.3 Tm. The variation of the field is less than 10% over the whole acceptance. Field clamps both in front and behind the magnet reduce the field strength in the nearest tracking chambers to less than 0.1 T .

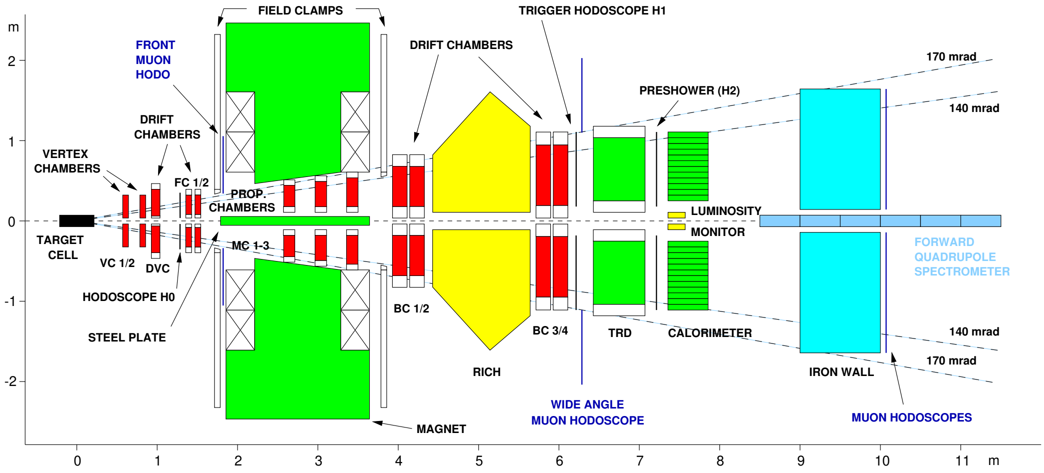

Fig. 3.1: The HERMES spectrometer. The horizontal and vertical scales represent the actual distances in metres.

3.4.2 Tracking

The tracking system consists of several detectors, before, inside and behind the spectrometer magnet. To establish tracks which traverse the whole spectrometer, tracks before and behind the magnet are reconstructed [27] by two sets of detectors. From the two sets of reconstructed tracks matching pairs are selected possibly involving the magnet chambers, which are situated in the spectrometer magnet. These pairs are used to determine the particle momentum from the deflection of the tracks in the spectrometer magnet. Moreover, the reconstructed tracks can be correlated with hits in the particle identification detectors.

The vertex chambers [28], drift vertex chambers and front chambers before and two sets of back chambers [29] behind the magnet provide the hit information. The vertex chambers comprise a set of multi-strip gas chambers. During part of the data-taking period, in which the data described in this thesis were collected the vertex chambers were inactive due to radiation damage incurred by the read-out chips. The drift vertex chambers, the front chambers and the back chambers are conventional drift chambers. In addition there are magnet chambers, which are multi-wire proportional chambers. They are used to reconstruct front tracks that are passing outside the acceptance of the back chambers. The momentum resolution of the HERMES spectrometer ranges from 0.7 to 1.25% over the measured kinematic range. The angular resolution is better than 0.6 mrad.

3.4.3 Particle identification

In order to achieve lepton identification with a high efficiency and a low hadron contamination the responses of various dedicated detectors are combined. The particle identification system consists of a Čerenkov detector, a transition radiation detector, two sets of hodoscopes, and an electro-magnetic calorimeter [30]. The hodoscope in front of the calorimeter is preceded by two radiation lengths of lead such that it acts as a pre-shower counter. In 1998 the existing threshold Čerenkov counter was replaced by a Ring Imaging Čerenkov Hodoscope (RICH) [31] to improve the identification of protons, pions and kaons.

The combined outputs of the calorimeter, the pre-shower counter, the Transition Radiation Detector (TRD) and the threshold Čerenkov provide an electron detection efficiency larger than 95% with a hadron contamination of only 1% in the lowest x-bin. The signals of the four detectors are combined using likelihood distributions. First the results of the calorimeter, pre-shower and Čerenkov are used to form the following quantity for the Particle IDentification, PID3:

$$\mathrm{PID3} = \log_{10}\left[\frac{(P^e_{Cal}P^e_{Pre}P^e_{Cer})}{(P^h_{Cal}P^h_{Pre}P^h_{Cer})}\right], \tag{3.1}$$

where P^i_j is the conditional probability that a particle of type i produced a given response in detector j. These P's are determined by comparing the measured detector responses for each track to a library of response functions, which are obtained either from data or modelled using Monte Carlo techniques. For the TRD, which consists of six independent chambers PID5 is calculated:

$$\mathrm{PID5} = \log_{10}[P^e_{TRD}/P^h_{TRD}]. \tag{3.2}$$

In general, requirements on the sum of PID3 and PID5 are used to select leptons and hadrons. By only using conditional probabilities the effect of the non-uniform flux of particles incident on the detectors is neglected. This results in a momentum and scattering-angle dependence of the PID distributions. To calculate real probabilities one needs to perform a Bayesian iterative procedure. The conditional probabilities and the flux ratio, Φ, which is the ratio of hadrons to positrons incident in the detector, serve as input for this procedure. One starts with Φ^0=1 and uses this to calculate $P^1_{e^+}$ and Φ^1, which enters the procedure to give $P^2_{e^+}$ and Φ^2. This scheme is repeated until $|\Phi^{n-1} - \Phi^n|$ becomes smaller than the uncertainty of Φ^n, which usually occurs within 10 steps. The end-result is a log-likelihood distribution with PID efficiencies and contamination factors which are momentum and scattering angle independent.

3.4.4 Luminosity measurement

For a proper weighting of the data collected in different time periods, the number of selected events have to be normalised. The normalisation is obtained by measuring the luminosity, which is the product of the target-gas density and the beam current. To achieve this, a luminosity monitor is installed 7.2 m downstream of the centre of the target. The luminosity detector consists of two small electro-magnetic calorimeters, which are moved close to the beam line before data taking is started. Both calorimeters are retracted during injection and ramping of the lepton beam. The measurement is based on elastic scattering of the beam leptons off the target-gas electrons. Both the scattered lepton and the hit electron are detected in coincidence, with the requirement of each depositing at least 5 GeV in the calorimeters. In case of an electron beam the process is $e^-e^- \rightarrow e^-e^-$, known as Møller scattering. For a positron beam the processes are $e^+e^- \rightarrow e^+e^-$, known as Bhabha scattering, and the annihilation into photon pairs $e^+e^- \rightarrow \gamma\gamma$. Both are electro-dynamical processes which are well understood, including the associated radiative corrections. In principle, this system can be used for an absolute determination of the luminosity. However, the data for the relative cross sections presented in this thesis only rely on the relative normalisation provided by the luminosity detector.

3.4.5 Trigger

The trigger system is designed to select events on the basis of signatures of potentially interesting events and reject background events. For a DIS event, hits in the three scintillator hodoscopes and a signal from the calorimeter corresponding to a deposition of at least 1.4 GeV in two adjacent calorimeter rows in coincidence with the HERA bunch signal are required. There are several other triggers available which are used to identify different possible hadronic final states as well as to determine trigger efficiencies. The maximum trigger rate which can be handled by the HERMES data-acquisition system with a dead time of less than 10% is at most 500 Hz. For a 3.5 GeV calorimeter threshold, used when taking data with unpolarised targets, about 2/3 of the triggers had tracks. Of the reconstructed tracks 95% came from the target, and about 1/3 of these events had a possible DIS lepton track.

3.4.6 Data acquisition

To minimise the dead time of the data-acquisition system (DAQ) double buffering is implemented. Event collection is done in parallel with the read out of the next event. Nevertheless, it is not always possible to accept all the events generated by the triggers. As this dead-time effect influences the number of selected events it has to be taken into account in the normalisation of the measured data. The dead-time fraction is defined for each trigger individually:

$$\delta_i = 1 - \frac{T^i_{acc}}{T^i_{gen}}, \tag{3.3}$$

where T^i_{acc} and T^i_{gen} represent the numbers of accepted and generated triggers of a certain scheme, respectively. Since the DAQ throughput depends on trigger rates, the trigger dead time fractions are calculated for short time periods of 10 seconds, called bursts. For several reasons these bursts can be shortened sometimes. As a consequence information stored on a burst-by-burst basis has to be corrected for burst-length differences.

3.4.7 Data taking

At HERMES there are three modes of data taking. The most common mode is normal polarised-target data taking where the luminosity is limited by the target densities which can be obtained with the atomic beam source. Data taking with unpolarised targets can be done in two ways. Normally, unpolarised target densities are limited by the beam lifetime and a luminosity of at most $10^{32}\,\mathcal{N}\mathrm{cm}^{-2}$ is obtained. Alternatively, data are collected in higher density running, which is done either in a dedicated run for HERMES only[2], or regularly at the end of each fill. Under these conditions the luminosity is limited by the trigger rates or the dead time. In this way luminosity values slightly in excess of $10^{33}\,\mathcal{N}\mathrm{cm}^{-2}$ have been obtained.

[2] The other HERA experiments do not collect data during such runs.

4. THE CROSS-SECTION RATIO OF DEUTERIUM TO HYDROGEN

4.1 Introduction

The measurement of the cross-section ratio for deep inelastic scattering on deuterium to hydrogen can provide interesting information on the quark-gluon structure of nucleons. More specifically, the following issues can be addressed:

- From the ratio of the measured cross sections, σ^d/σ^p, the ratio of the structure function F_2 of the neutron to that of the proton F_2^n/F_2^p can be extracted (eq. 2.33). In the quark-parton model (sect. 2.4) of the nucleon F_2^n/F_2^p represents the ratio of the parton distributions in the neutron and the proton. Deviations of this ratio from unity are related to differences between the up and the down quark distributions in the nucleon. The region at high x is particularly interesting as in that region the valence quarks dominate, implying that the measured ratio at $x \to 1$ provides information on the relative importance of the u and d valence quarks. In the limit $x \to 1$ different predictions for F_2^n/F_2^p exist. Currently the predictions [11, 12, 13, 14] range from $\frac{1}{4}$ to $\frac{2}{3}$. In section 2.7 the different models providing these predictions are discussed. Furthermore, precise knowledge of the u and d quark distributions at high x is very important at collider energies, as the extraction of new physics at high Q^2 relies on this information [32]. At low x, the sea quarks are dominant and their distribution is usually assumed to be nearly identical for the proton and the neutron.

- DIS data on proton and 'neutron' targets can be used to investigate possible differences between the value of the ratio $R = \sigma_L/\sigma_T$ for the proton and the neutron. The difference is expressed in terms of $\Delta R = R^d - R^p$. Both NMC and SLAC have published measurements on ΔR [1] [2], which can be compared to new HERMES results, thus extending such data to lower x and Q^2 values. The existing data on ΔR are presented in figure 4.1 showing that there is no deviation from zero observed in the presently covered (x, Q^2) domain. Possible deviations of ΔR from zero could be of interest as they might be related to differences of the gluon distribution for the proton and the neutron [33], or higher twist effects, which are discussed in the next item. It is noted that the quality and amount of the data available is limited below $x \simeq 0.1$.

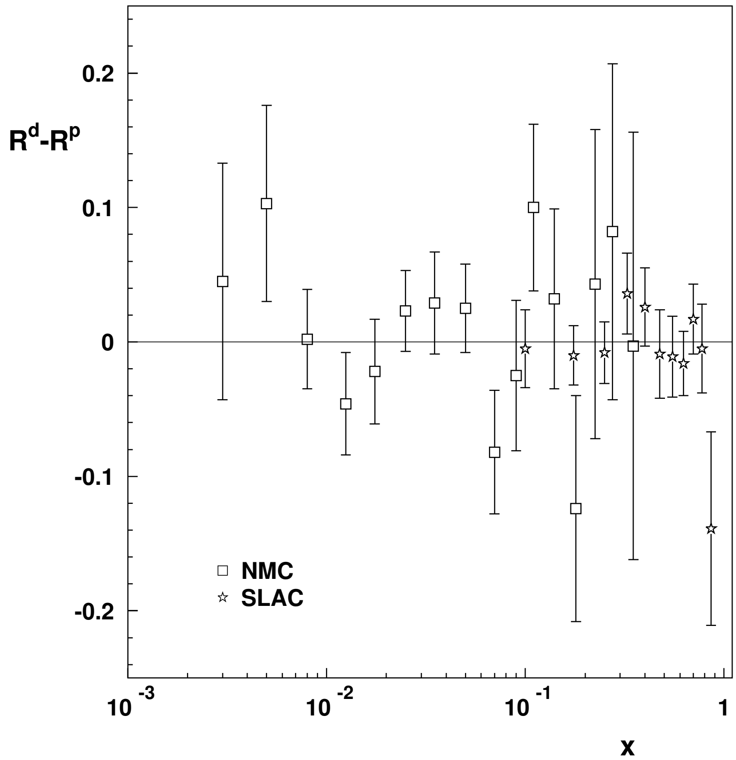

Fig. 4.1: World data on $R^d - R^p$ from NMC [1] and SLAC [2].

- Higher twist effects, which were introduced in section 2.5, can also be studied with F_2^n/F_2^p data. These effects represent quark-gluon correlations, which are possibly different for the proton and the neutron. As one does not know whether the effects are flavour dependent or possibly enhanced in the nuclear environment we study the difference between the proton and neutron (deuteron). There are two regions of interest to search for higher twist effects.

  At low x any deviation from the quark-parton-model prediction of $R = 0$ can be associated with higher twist effects. At low x also the average Q^2 is low thereby increasing the factor $1/Q^{2n}$, which governs higher twist effects, further clarifying the sensitivity for higher twist effects.

By comparing R^p and R^d in this domain it can be investigated whether in the vicinity of another nucleon these effects increase, as has been suggested [20].

At high x the differences between the quark distributions in the proton and neutron are most prominent as at high x the valence quarks dominate. Therefore, the high x region is the best domain to look for higher twist effects related to u-d quark differences. The non-perturbative phenomenological parameterisations of higher twist effects, such as the one used by Yang and Bodek [32] show this sensitivity as well: $F_2 = F_2^{pQCD}(1 + h(x)/Q^2)$ with $h(x) = a[x^b/(1-x) - c]$, i.e. the effect grows with x.

- In a recent paper [20], it has been shown how DIS data collected at HERMES can be analysed to obtain information [1] on R^A/R^d. Applying this technique to new σ^d/σ^p data, one can extract R^d/R^p, σ_L^d/σ_L^p, and σ_T^d/σ_T^p, where the subscripts, L and T, refer to the longitudinal and transverse cross section.

In this chapter the analysis of the σ^d/σ^p data is described in detail. These data are used to extract information on F_2^n/F_2^p and $R_{d/p} = R^d/R^p$ exploiting the large range of values of the virtual photon polarisation parameter, ϵ, covered by the HERMES experiment. The extraction of the ratio $R_{d/p}$ presented here[2] is not based on the Rosenbluth separation method which is explained in section 2.3. This method could not be used at HERA as all the data have been collected at a single beam energy of 27.5 GeV[3]. When combining the results of the present experiment with those obtained by NMC, effectively several beam energies are used.

This chapter is organised as follows. In section 4.2 the data selection is discussed, and the necessary corrections are described in section 4.3. The cross section ratio σ^d/σ^p is presented in section 4.4. A comparison with the existing data follows in section 4.5. The extraction of R and F_2 is the subject of section 4.6. In the subsequent section the data are used to search for higher twist effects at high x. The Gottfried sum-rule is evaluated in section 4.8. In the last section the conclusions are presented.

[1] Part of the effect reported [20] is due to an unexpected instrumental effect, i.e. photon showering in the beam pipe.

[2] This restriction only applies to those results that are based on HERMES data alone. When results are obtained from an analysis including NMC and HERMES data implicitly use is made of the Rosenbluth method.

[3] A Rosenbluth separation in the region of interest, low x and low Q^2, requires a second beam energy of a considerably higher value than the 27.5 GeV available at HERA.

4.2 Data selection

For the analysis presented in this chapter all the unpolarised hydrogen and deuterium data taken during HERMES run I (1995-2000) have been considered. In the following subsections the data selection criteria are presented as they are applied at the various levels. Also the kinematic requirements posed to identify DIS events are listed.

4.2.1 Burst selection

The runs which can be used for data analysis are selected using logs filed during data taking. In this manner unpolarised runs for hydrogen and deuterium can be identified. Every run consists of a number of bursts, for which the following data quality requirements were imposed.

- Live time : $\tau_{\text{live}} > 80\%$;
- Burst length : $9 < T_{\text{burst}} < 11$ s;
- Burst : first and last of each run are removed;
- Data-acquisition system: no error flags;
- Gain-Monitoring System : no error flags;
- Transition Radiation Detector: both top and bottom ok;
- Tracking detectors: no high voltage trips.

4.2.2 Event selection

The selection of DIS events is performed by putting requirements on several detector related quantities and by imposing certain kinematic restrictions. Concerning the kinematic requirements, two regions are distinguished: the DIS region characterised by $W^2 > 4$ GeV^2 and the baryon-resonance domain ($W^2 < 4$ GeV^2). Usually the latter domain is excluded in analyses of $F_2(x)$, but recently it has been shown [34] that for $Q^2 > 2$ GeV^2 the resonance region - on average - can be described by $F_2(x)$ derived from DIS data [35]. For that reason the data at $W^2 < 4$ GeV^2 are also considered and are referred to as “duality region” in reference to the concept of quark-hadron duality underlying this equivalence [35]. Below the requirements for valid DIS events are listed.

- Detector acceptance

- Horizontal acceptance $-170 < \theta_x < 170$ mrad
- Vertical acceptance $35 < |\theta_y| < 140$ mrad

- Target gas volume
  - Longitudinal size $-18 < z_{\text{vert}} < 18$ cm
  - Transverse size $t_{vertex} < 0.43$ cm
- Particle identification
  - Lepton identification PID3 + PID5 > 2
- DIS kinematics
  - Q^2 domain $0.1 < Q^2 < 15$ GeV^2
  - Above resonance region $W^2 > 4$ GeV^2
  - Limited size of radiative correction $y < 0.85$
- Duality kinematics
  - Resonance region $W^2 < 4$ GeV^2
  - Duality region $Q^2 > 2$ GeV^2

4.2.3 Lepton identification

The identification of leptons was done using the PID scheme presented in section 3.4.3. Leptons are identified by requiring PID3+PID5 > 2. For the data collected after 1997 PID3 reduces to PID2 as the threshold Čerenkov was replaced by a RICH, for which a separate PID scheme is used. The resulting lepton identification efficiency is 97% with a hadron contamination of only 0.01%. These numbers were obtained from a similar analysis [36].

4.2.4 Selected DIS events

After applying the selection requirements as listed above a total of about 25 million DIS events on hydrogen and deuterium were selected for analysis. The number of events per year and per gas are listed in table 4.1. As in 1999 no hydrogen data were taken, and hence no deuterium to hydrogen ratio could be determined, it was decided to add the deuterium data of 1999 to those of 2000 as there was no change in the detector system between these two periods of data taking.

Year	$H(\times 10^6)$	$D(\times 10^6)$
1996	1.71	2.83
1997	2.01	3.06
1998	0.82	1.59
1999	-	0.43
2000	10.11	2.37
total	14.66	10.30

Tab. 4.1: Number of unpolarised DIS events obtained per year during HERMES run I.

4.3 Corrections

Several corrections have to be applied to the raw data in order to be able to extract relative cross sections. The relevant corrections are described briefly below. In some cases it is argued that a given correction can be neglected for the unpolarised deuterium and hydrogen data presented in this thesis.

4.3.1 Flux factors

In order to correct the PID scheme for the non-uniformity of the flux of particles incident on the detector so-called flux factors have been introduced (see section 3.4.3). They depend on the scattering angle of the particle and its momentum. In principle, one can determine and subsequently apply these flux factors for each year and each target gas separately. However, it has been shown that for a given year the flux factors are identical if hydrogen or deuterium is used as target gas [37]. As a result the application of flux factors in the lepton identification will yield a similar change in the lepton identification efficiency and hadron contamination for both targets. Therefore, the influence of the flux factors cancels in the cross section ratio and could thus be omitted in the present analysis. To account for a possible systematic effect due to neglected flux-factor differences between hydrogen and deuterium, it has been estimated that an additional systematic uncertainty of only 0.5% needs to be introduced to the ratio of the cross sections.

4.3.2 Smearing

Partial energy losses and local inefficiencies in detector planes can cause a shift in the measured values of the kinematic variables as compared to the original values at the interaction point. To understand these shifts Monte Carlo simulations have been performed for both hydrogen and deuterium.

These simulations were carried out by M.Vincter to investigate the effect of the detector and the track reconstruction algorithm on the evaluation of the kinematic variables [38]. For the variable x a broadening of the distribution and a tail towards lower x is observed. This effect is negligible at low x, but significant at high x. In the simulation the shift of the mean to lower x and the misidentification of events at higher x have been combined, making use of a realistic cross-section parameterisation. However, since these effects are the same for hydrogen and deuterium within 0.25% these effects can be neglected as the ratio is taken. Hence, it has been decided to neglect the smearing contribution and introduce a separate contribution of 0.25% to the total systematic uncertainty on σ^d/σ^p to account for the fact that these effects were neglected.

4.3.3 Radiative corrections

The cross section ratios presented in this chapter are extracted from normalised yields of DIS events on deuterium and hydrogen. In the normalised yields events enter which do not correspond to deep inelastic scattering events. Apart from the Born cross section, which we wish to measure, there are also contributions from elastic or quasi-elastic scattering processes. These events are identified as DIS events because a photon was radiated by the scattering lepton before or after an elastic or quasi-elastic event. It may also happen that a photon is emitted by the lepton after a normal DIS event, causing a shift in the kinematics of the event. To extract the Born cross section from the data radiative corrections are applied, which correct for all these effects. The radiative corrections are calculated using the TERAD program [39]. The program takes into account the following higher order QED processes that result in the emission of additional photons: contributions from vacuum loops of all leptons and quarks, lepton pair production, electroweak interference and bremsstrahlung of one or two photons. The complete list of diagrams can be found in reference [40]. The size of the radiative corrections is different for deuterium and hydrogen, mainly due to the elastic contribution. Furthermore, there is an uncertainty associated with this correction as the phenomenological input parameters carry uncertainties. The size of the corrections and the associated uncertainties are explicitly listed in table 4.4 in section 4.4.4.

4.3.4 Photon shower effect

When collecting DIS data from nitrogen and deuterium a deviation of the cross section ratio from existing data at $x < 0.06$ and $Q^2 < 1.5$ GeV^2 was found [20]. As the new data were collected at a much lower beam energy than used for the existing data as obtained by NMC [41], and thus corresponding to a lower value of ϵ, a new effect was thought to be found. However, further measurements on heavier targets could not be analysed consistently until it was realised that an instrumental effect caused the discrepancy with respect to previous data. The hard Bremsstrahlung photons produced in nuclear elastic scattering have a large probability of hitting detector frames for the kinematic region where the deviation was found. These Bremsstrahlung photons are mostly emitted in three directions: along the beam, along the scattered lepton and in the direction of q. It is this last (Compton scattering) peak that caused the problem. When these events occur, extensive electro-magnetic showers are produced, creating very high multiplicities in part of the spectrometer. These events are impossible to track and are rejected for further analysis, thereby causing a significant tracking inefficiency. This effect is called the Photon Shower Effect (PSE).

The calculated radiative corrections are based on the assumption that all Bremsstrahlung events are observed and therefore the correction is overestimated. This causes the extracted Born cross section to be too low. Once this was realised Monte Carlo studies were performed, which were compared to special data productions to evaluate the size of the required PSE correction. In table 4.4 the size of both the radiative corrections (column 5 and 6) and the PSE correction are presented (column 3) As expected, the PSE correction factor is largest at low x and Q^2, where the radiative corrections are also largest. It can be seen that the PSE correction on the ratio σ^d/σ^p ranges from 4.2% at low x to less then 1% for $x > 0.035$, while beyond $x \sim 0.1$ the PSE is negligible. As the correction is based on a Monte Carlo simulation that involves the rather complicated (detector frame) geometries, we have to assign a systematic uncertainty to the PSE correction, which is presented in column 4 of table 4.4 and is highest at the lowest x, 1.4%, and drops off towards $x = 0.1$.

4.3.5 Charge symmetric background

In the HERMES experiment there are various sources of e^+e^- pairs, e.g. a π^0 decaying into a $\gamma\gamma$-pair of which one photon could produce an e^+e^- pair. The e^+ or e^- lepton, depending on the beam charge, can be misidentified as the scattered lepton from a DIS event. These events are known as Charge Symmetric Background (CSB) events. The correction for these events can be taken from an analysis of events containing a lepton of opposite charge (with respect to the beam charge). The total number of events selected this way amounts to $\sim 2\%$ of the events found in the regular DIS analysis. However, the CSB data have a significantly different x-distribution; peaking at low x. In certain low x bins the CSB can be as large as 6%. If it is assumed that the acceptance is identical for CSB and DIS events, one can subtract the CSB events per (x, Q^2) bin, where after the radiative corrections are applied.

The number of DIS events, $N_{\rm DIS}$, has been evaluated as follows from the observed number of events, $N_{\rm total}$, in a given bin and the number of CSB events, $N_{\rm CSB}$:

$$N_{\rm DIS}(x, Q^2) = N_{\rm total}(x, Q^2) - N_{\rm CSB}(x, Q^2). \tag{4.1}$$

These numbers of events are not yet corrected for the radiative corrections, which need to be applied. This is discussed in the following section.

4.4 Experimental data on σ^d/σ^p

In this section the determination of the actual cross section ratio σ^d/σ^p is presented. This involves a number of steps, which are discussed in separate subsections on normalisation (4.4.1), error calculation (4.4.2 and 4.4.4) and reproducibility (4.4.3).

4.4.1 Normalisation

The normalisation of the selected DIS events, corrected for the CSB as described in the previous section, is done in the following manner. The overall normalisation is performed by dividing the number of events in a given bin by the total integrated luminosity ($\mathcal{L}$) for the selected bursts, corrected for the length of these bursts ($T_{\rm burst}$) and the live-time of the data acquisition system ($\tau_{\rm live}$) for that burst. At the same time the radiative corrections (η) are applied, which reduce (or, at high x, increment) the selected number of events $N_{\rm DIS}$. The radiative correction factors take into account the fact that the radiative corrections for DIS events are different from the radiative correction for CSB events. This leads to the following yield definition:

$$Y = \frac{N_{\rm DIS} \cdot \eta}{\mathcal{L} \cdot T_{\rm burst} \cdot \tau_{\rm live}} \tag{4.2}$$

The cross section ratio σ^d/σ^p per nucleon can be obtained by also taking into consideration the double number of nucleons in deuterium with respect to hydrogen.

$$\frac{\sigma^d}{\sigma^p} = \frac{Y^d/2}{Y^p} \cdot C_{pse} \tag{4.3}$$

The correction for the photon shower effect C_{pse} is taken into account as a correction on the cross section ratio for the applicable kinematics domain. It is emphasised that Eq. 4.2 is evaluated at the burst level. The bursts have a duration of 10 s (see section 3.4.6). In the results presented hereafter, Y^d and Y^p have been integrated over a year for each bin, where after the ratio of Eq. 4.3 is evaluated.

4.4.2 Statistical uncertainties

The statistical uncertainties on the cross section ratio have been calculated taking into account the reduction of the number of events due to radiative corrections (η). This reduction can be as large as 60% in the lowest x bin, as illustrated in table 4.4. The reduction due to the CSB events (at most 6%) is also included. As a result, for the radiative corrections a factor $1/\eta^p$, representing the radiative corrections calculated for the proton target, enters, which is deduced in [42], while for the CSB correction a subtraction of the CSB is performed. The resulting absolute uncertainty on the measured cross-section ratio is obtained as follows:

$$\delta\left(\frac{\sigma^d}{\sigma^p}\right) = \frac{\sigma^d}{\sigma^p}\sqrt{\left.\frac{N_{DIS}+N_{CSB}}{(N_{DIS}-N_{CSB})^2}\right]_d + \left.\frac{N_{DIS}+N_{CSB}}{(N_{DIS}-N_{CSB})^2}\right]_p} \cdot \frac{1}{\eta^p} \tag{4.4}$$

It is noted that for historical reasons radiative corrections are usually treated as a multiplicative factor (η^p in eq. 4.2), which is reasonable as long as as the corrections are small. In our data the corrections are large at low x and hence it would have been more appropriate to treat them in a subtractive manner. As a result the uncertainties would have increased. The factor η^p in eq. 4.4 accounts for this enlargement of the uncertainties, while keeping to the multiplicative approach.

4.4.3 Reproducibility

In order to investigate the reproducibility of the measurements, the data taken in the years '96, '97, '98, and '99 together with 2000 have been analysed separately. As a first step we compared the present analysis of the 1996 data with an early analysis performed by Vincter[43]. In figure 4.2 the comparison is shown between the σ^d/σ^p ratio produced by both analyses. It is noted that the analyses are based on two different versions of the basic event reconstruction and have employed different data quality criteria and different kinematic requirements. In particular the W^2 and Q^2 requirements were different. In the so-called 96b3 μDSTs used by Vincter the reconstruction included the tracks recorded by the vertex chambers, while those were not used (in order to be consistent with later years) in the 96c1 μDSTs used in the present analysis. The agreement between the two analyses is reasonable, especially if it is realised that the correction for the PSE nor the error enlargement factor ($1/\eta^p$) were considered by Vincter. Since a different binning is used in the two analyses, no point to point comparison can be made. However, by comparing the data set from the analysis performed by M. Vincter with a fit to the data set of this analysis, similar to the fit shown in figure 4.9, an agreement was found with a confidence level of 95% in the kinematic overlap region between the two analyses. It can be seen in figure 4.2 that in the present analysis a larger kinematic range is covered. This is a consequence of the reduced restrictions on x (Vincter: $x > 0.012$) and W^2 (Vincter: $W^2 > 4$), which is related to the proof of duality.

To verify the year-to-year reproducibility, the cross section ratios are shown in figure 4.3 for each year separately. For each year the data are also divided by a fit of the sum of the data over all years in order to establish the relation of each year with respect to the five-year average. It is seen that the shapes of the cross-section ratio for the different years agree very

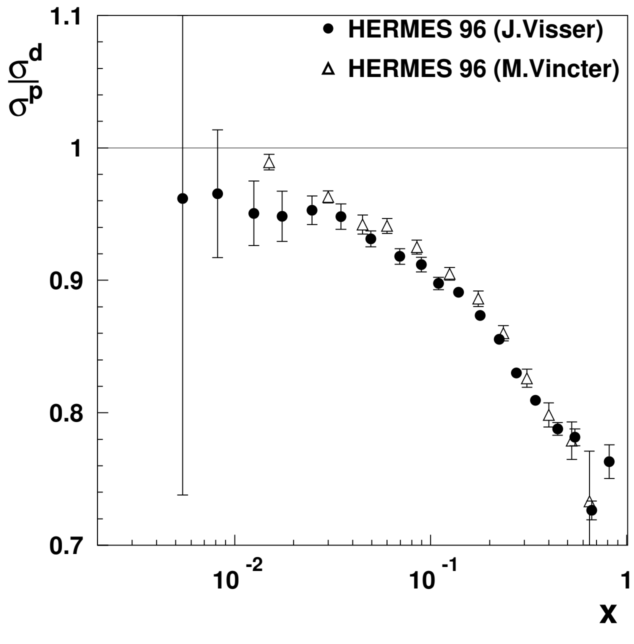

Fig. 4.2: Ratio of the cross section per nucleon for deuterium and hydrogen as a function of x. Two analyses are compared, both performed on the HERMES 1996 data sample. The open triangles represent the analysis done by M. Vincter using the 96b3 μDSTs, involving different kinematic requirements, while the solid circles show the results of the present analysis performed on the 96c1 μDSTs.

well, while the relative normalisation factors are compared in table 4.2. It is noticed that the '97 cross section ratio is $1.2 \pm 0.1\%$ low with respect to the average. This is significantly more than the deviation of the other years with respect to the average and cannot be explained as a statistical fluctuation. While searching for a cause to explain the reduced cross-section ratio of the

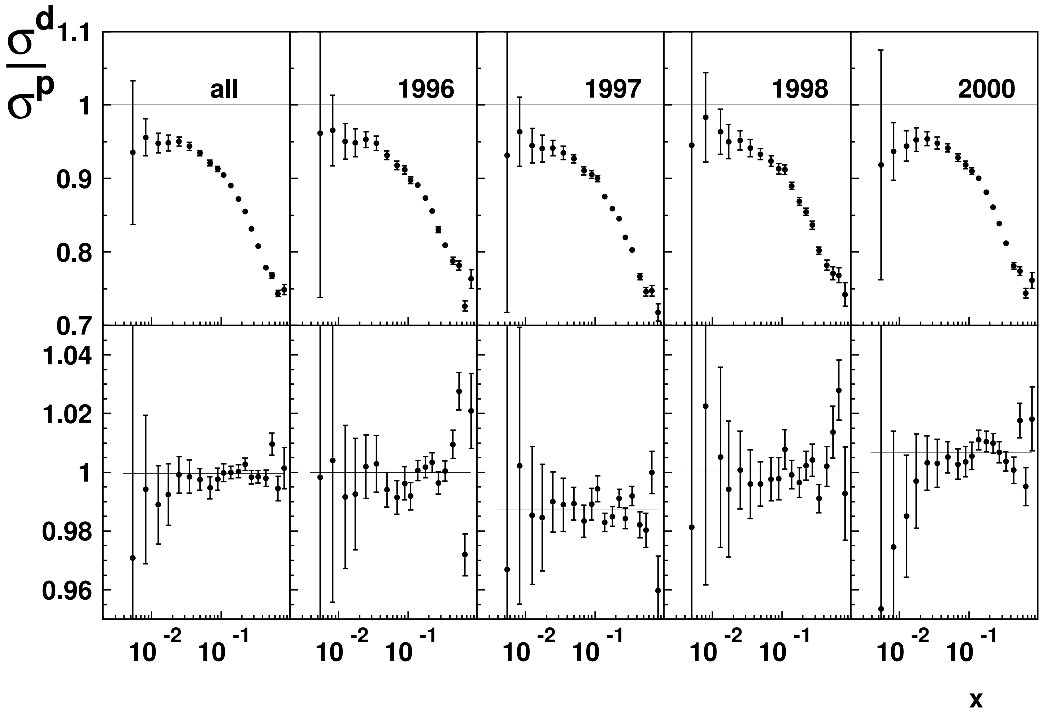

Fig. 4.3: The deuterium to proton cross-section ratio as measured in four different periods, i.e. '96, '97, '98, and '99 and 2000 combined. In the lower panel the ratio of the measured data, as presented in the upper panel, to the fit of all data combined, like the fit in figure 4.9, is shown.

'97 data a non-linear behaviour of the deuterium yield with respect to the luminosity rate was found. In order to further investigate this, all fills in which both deuterium and hydrogen data were collected, were analysed separately. Several fills showed a large (up to 10%) drop in the cross-section ratio, while in the data quality information nothing could be found to explain this drop. It is concluded that the '97 data set suffers from a non-linear behaviour of the rate as measured by the luminosity monitor, which does not show up in later years due to subsequent changes to the device. Therefore the '96, '98, and the combined '99 and 2000 data sets were added to verify the normalisation of all years with respect to the weighted average. This produced a deviation

	1996	1997	1998	1999+2000
I	0.1 ± 0.1	-1.2 ± 0.1	0.1 ± 0.2	0.7 ± 0.1
II	-0.4 ± 0.1	-1.7 ± 0.1	-0.3 ± 0.2	0.3 ± 0.1

Tab. 4.2: Relative deviation (in %) of the different years with respect to the grand total. Total I includes all years and total II excludes 1997.

of at most 0.4 ± 0.1% (for the '96 data set), while for the '97 cross section ratio a 1.7 ± 0.1% deviation was found. It was concluded that the '96, '98 and '99 and '00 data sets are in mutual agreement. As the '97 cross-section ratio is systematically low, presumably due to the non-linear luminosity monitor behaviour, it was decided to renormalise the '97 cross-section ratio by 1.7%. After the normalisation the '97 data were added to the other data sets for further analysis. The systematic uncertainty due to the spread in the measured cross-section ratios for different years can be roughly estimated by taking the statistically weighted sum of the reproducibility factors. Adding the deviations weighted by their uncertainties corresponds to a systematic uncertainty due to the limited reproducibility of the data of 0.7%.

4.4.4 Systematic uncertainties

The total systematic uncertainty on the measured cross-section ratio is given by the uncorrelated contributions, associated with particle identification, smearing corrections, the uncertainty in reproducing the cross-section ratio for different years, the uncertainty in the estimation of the photon shower effect (PSE), and the systematic uncertainty on the radiative corrections. The x and Q^2 independent contributions to the total systematic uncertainty are listed in table 4.3. They are added in quadrature to yield an uncertainty of 0.9%. The uncertainties on the photon shower effect and the radiative cor-

Contribution	Uncertainty
Flux factors	$< 0.5\%$
Smearing	$< 0.25\%$
Reproducibility	$\simeq 0.7\%$
Total	$\simeq 0.9\%$

Tab. 4.3: Overview of the x and Q^2 independent contributions to the total systematic uncertainty on the cross section ratio.

rections are clearly depending on x and Q^2 and therefore they are presented in table 4.4, where their x dependence is shown. The size of the photon shower effect correction and the radiative corrections are listed in column 3, 5 and 6, while the contribution to the systematic uncertainties are presented in columns 4 and 7, respectively. The radiative corrections are calculated for hydrogen and deuterium separately, while the systematic uncertainties on the radiative corrections are given for the cross-section ratio. The systematic uncertainty on the PSE is presented in figure 4.4. In the upper panel the

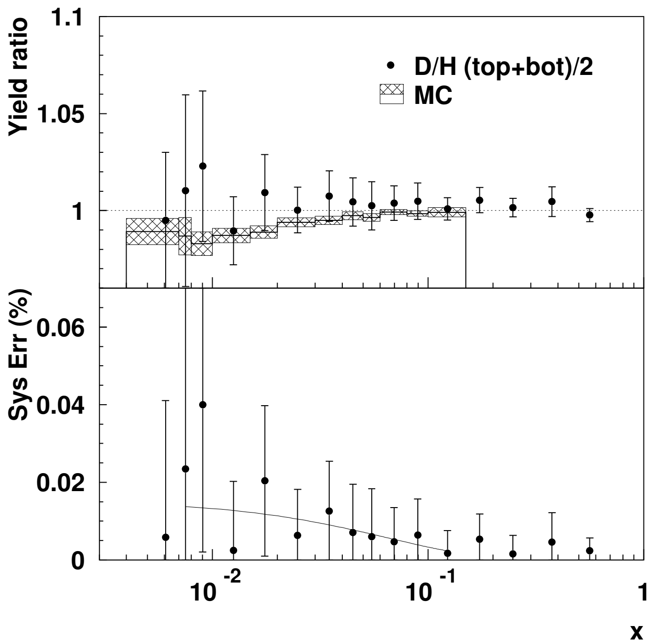

Fig. 4.4: Photon-shower-effect systematic uncertainty (lower panel), deduced from the comparison of the special data analysis and the Monte Carlo studies (upper panel).

comparison between data and Monte Carlo is shown. The data have been produced with a special tracking analysis to establish the size of the PSE. Presented is the average of the σ^d/σ^p analysis performed using only the top detector half and only the bottom part of the spectrometer. The difference between the result obtained from the data as compared to the Monte Carlo results is shown in the lower panel. The difference becomes larger at low x and somewhat unstable due to the limited data available for this study. To work with a smooth systematic uncertainty, the shown difference was fitted by a smooth 2^{nd} order polynomial. The result is plotted in the lower panel and used to evaluate the PSE systematic uncertainty listed in table 4.4. The total uncertainty, when taking into account the other contributions, is listed in the last column of table 4.4. In this table the relative error is presented, while in the figures the systematic error band shown represents the absolute systematic uncertainty for ease of interpretation.

x	Q^2	PSE(corr)	PSE(sys)	RC(p)	RC(d)	RC(sys)	total(sys)
0.0038	0.17	0.959	0.0145	0.28	0.41	0.039	0.046
0.0053	0.23	0.958	0.0142	0.32	0.43	0.033	0.040
0.0081	0.34	0.963	0.0136	0.39	0.49	0.033	0.040
0.0125	0.49	0.963	0.0127	0.48	0.56	0.030	0.037
0.0174	0.65	0.971	0.0117	0.55	0.61	0.027	0.034
0.0248	0.86	0.985	0.0105	0.62	0.66	0.025	0.032
0.0348	1.11	0.992	0.0090	0.68	0.71	0.024	0.031
0.0495	1.40	0.995	0.0072	0.74	0.77	0.018	0.026
0.0695	1.73	0.996	0.0052	0.80	0.82	0.013	0.022
0.0896	1.98	0.997	0.0038	0.84	0.86	0.010	0.020
0.1096	2.18	1.0	0.0000	0.87	0.89	0.008	0.019
0.1388	2.42	1.0	0.0000	0.91	0.92	0.008	0.019
0.1789	2.68	1.0	0.0000	0.95	0.96	0.008	0.019
0.2234	2.92	1.0	0.0000	0.99	1.00	0.008	0.019
0.2732	3.16	1.0	0.0000	1.02	1.03	0.008	0.019
0.3418	3.75	1.0	0.0000	1.06	1.07	0.007	0.019
0.4444	4.36	1.0	0.0000	1.11	1.11	0.006	0.018
0.5441	4.45	1.0	0.0000	1.16	1.17	0.005	0.018
0.6629	4.31	1.0	0.0000	1.22	1.23	0.005	0.018
0.8163	4.05	1.0	0.0000	1.19	1.21	0.014	0.022

Tab. 4.4: Size of PSE and the radiative corrections (columns 3, 5 and 6) and their contribution to the systematic uncertainty and the total systematic uncertainty, including the contribution given in table 4.3, for the cross-section ratio for each x and Q^2 bin.

4.5 Comparison with previous measurements

In this section the HERMES data on σ^d/σ^p are compared to the data, previously collected by NMC [1] and SLAC [44]. First, the comparison will be made in the x-domain and then for each x-bin the Q^2-dependence of the data is presented.

4.5.1 Cross section ratio dependence on x

The cross-section ratio as measured at HERMES is presented in figure 4.5. In the left panel the data are compared to similar data obtained by NMC [1]. The NMC data were recorded using four different beam energies: 90, 120, 200 and 280 GeV. The kinematic range covered by the NMC data begins at $x = 0.0015$ and $Q^2 = 0.16$ GeV^2 and goes up to $x = 0.675$ and $Q^2 = 26.9$ GeV^2 corresponding to an average Q^2 of ~ 10 GeV^2 [45].

The shape of the two distributions is somewhat different. In order to investigate whether the difference in shape can be explained by the difference in average Q^2, at which the two data sets have been taken, we compare the HERMES data to a parameterisation [45] of the existing data, which is based on measurements from NMC, BCDMS, and SLAC. In this parameterisation the average Q^2 for each x bin can be inserted to evaluate σ^d/σ^p in each x bin, i.e. the parameterisation effectively includes the DGLAP evolution as described in section 2.5

This procedure leads to a better description of the data as can be seen in the upper plot in the right panel of figure 4.5, although there is a hint of possible small deviations at the extremes of the x distribution. To enhance possible differences at low and high x the HERMES data have been divided by the world data parameterisation. In the lower plot in the right panel of figure 4.5 small deviations from a flat behaviour can be observed at low and high x. Such deviations might be due to higher twist effects.

To study these differences the two kinematic regions will be considered separately in sections 4.6 and 4.7, respectively. At the highest x such an effect will correspond to a Q^2 dependence of F_2^d/F_2^p. At low x, where the Q^2 dependence is already known to be small [46], higher twist effects may show up in R, i.e. as a Q^2-dependent difference between R^d and R^p. These possible higher twist effects on R can be investigated by studying the ϵ-dependence of σ^d/σ^p. In the remainder of this chapter these deviations are studied in more detail by evaluating the Q^2-dependence of F_2^d/F_2^p at high x and the ϵ-dependence of σ^d/σ^p at low x.

4.5.2 Q^2-dependence

Comparing the HERMES data as a function of x with a Q^2-evolved parameterisation cannot reveal the details contained in the measurements. Therefore, the data are presented as a function of Q^2 in figures 4.6 and 4.7 for every x-point shown in figure 4.5. A comparison is made with both the NMC and SLAC data. The data sets agree well over most of the x and Q^2 region. However, possible small differences are hard to distinguish. To compare the

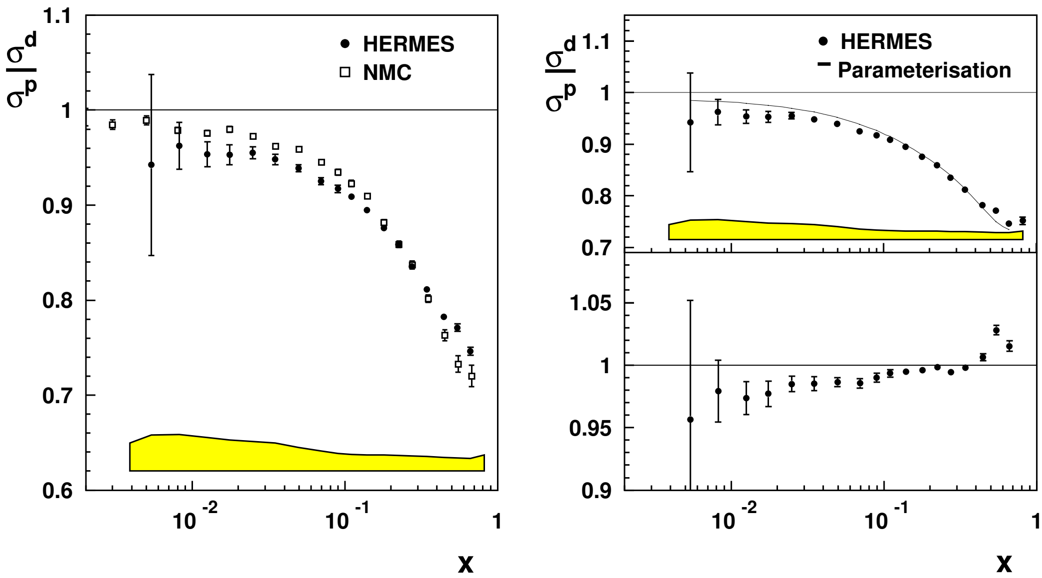

Fig. 4.5: In the left panel the comparison of σ^d/σ^p between the HERMES and NMC results is shown. The HERMES data are represented by the solid circles, the NMC data by the open squares. The error band indicates the systematic uncertainty.
The right-hand panel presents the comparison of the HERMES data with the world data parameterisation [45]. The parameterisation is calculated for the $\langle x \rangle$ and $\langle Q^2 \rangle$ values of the HERMES experiment. The lower part shows the deviation of the HERMES data from the parameterisation.

Q^2-dependence for the HERMES and NMC data sets, the following function was used to fit the data:

$$\frac{\sigma^d}{\sigma^p}(\langle x \rangle, Q^2) = a(x) + b(x) \ln Q^2 \tag{4.5}$$

The fit of the NMC data yielded the same values for a and b as were published [46]. Subsequently the same fit was used to extract a and b for the present data. A comparison for a and b obtained in this way is presented in figure 4.8. The offset a, which corresponds to σ^d/σ^p at $Q^2 = 1$, is in fair agreement for the two data sets. Remaining differences (of a few %) in the mid x-range possibly reflect a normalisation difference between the HERMES and NMC data, which is further discussed in section 4.6.2. For the slope, b, the HERMES data show a weak trend from slightly positive b-values at $x \sim 0.04$ to slightly negative b-values at high x, while the Q^2-dependence found for NMC is very small over the whole kinematic range. Assuming that the intrinsic Q^2-dependence of the data must be the same, the possible difference between $b(x)$ for both data sets can be due to an ϵ-dependence of the cross-section ratios. This is discussed in detail in the subsequent sections. However, in view of the large uncertainties involved the differences between the HERMES and NMC data displayed in figure 4.8, need not be significant.

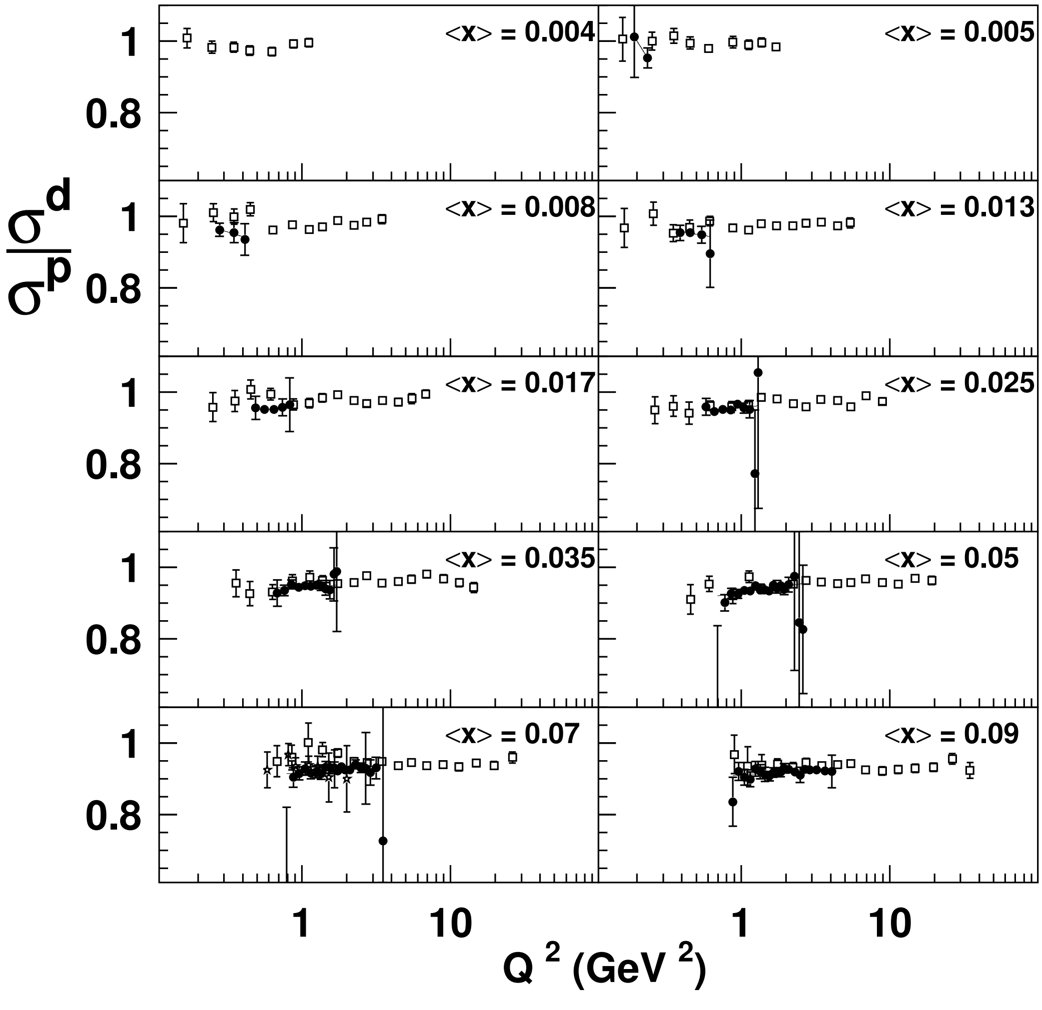

Fig. 4.6: The cross-section ratio per nucleon as a function of Q^2 in the different x regions for the HERMES (full circles), NMC (open squares), and SLAC (open stars) data. Also shown is the result of a fit as described by equation 4.5.

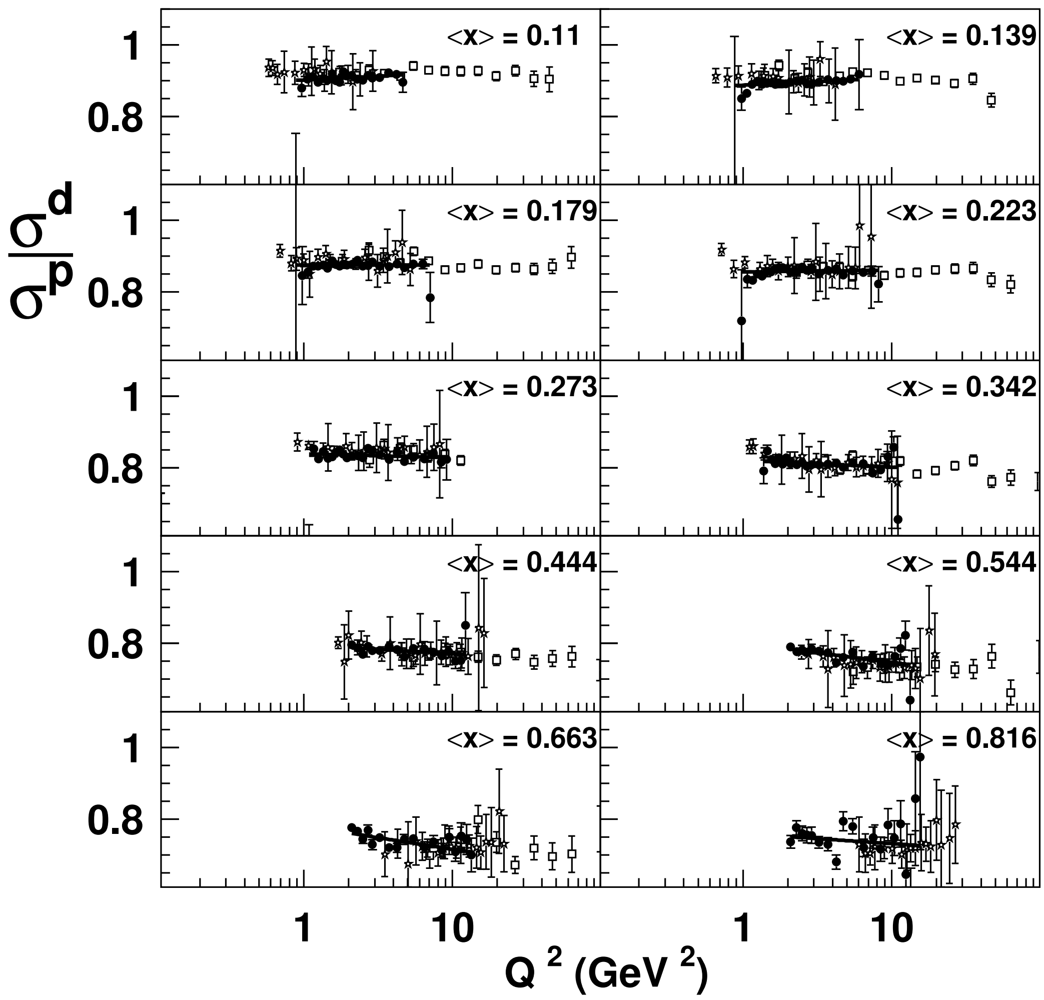

Fig. 4.7: The cross-section ratio per nucleon as a function of Q^2 in the different x regions for the HERMES (full circles), NMC (open squares), and SLAC (open stars) data. Also shown is the result of a fit as described by equation 4.5.

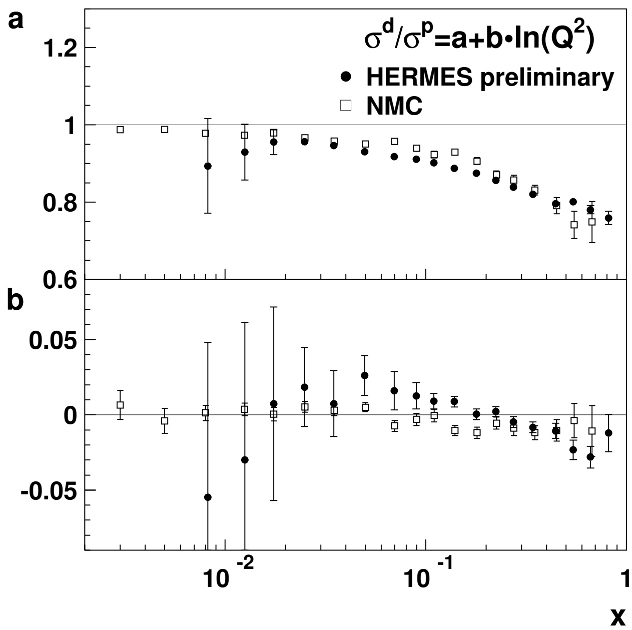

Fig. 4.8: The result of a $\ln(Q^2)$*-dependent fit. The offset* $a(x)$ *(upper panel) and the slope* $b(x)$ *(lower panel) are shown for both the HERMES data (solid circles) and the NMC data (open squares). Note that the systematic uncertainties (typically a few % in each data set) are not displayed.*

4.6 Extraction of R and F_2 related quantities

In order to extract R and other related quantities from the data a fitting procedure is adopted. The cross-section ratios are plotted versus ϵ for each x-bin. By fitting these data with two free parameters several quantities can be extracted, as will be explained in this section. However, before these fits can be performed several corrections have to be applied to the data, which will be dealt with first.

4.6.1 Bin-centring correction

The fitting of the ϵ-dependence at fixed x is not straightforward as the data contained in a certain x-bin are collected at slightly different x-values. Therefore, a bin-centring correction is needed such that all data are made to correspond with the weighted average $\langle x \rangle$ of that bin. For this bin-centring correction the cross-section ratio versus x was fitted with the following functional form:

$$f_{d/p}(x) = a + bx + cx^2 + dx^3 + e \ln x \tag{4.6}$$

The resulting curve[4] is shown in figure 4.9 together with the data, which are well described. Subsequently, the fit was used to correct the measured cross-

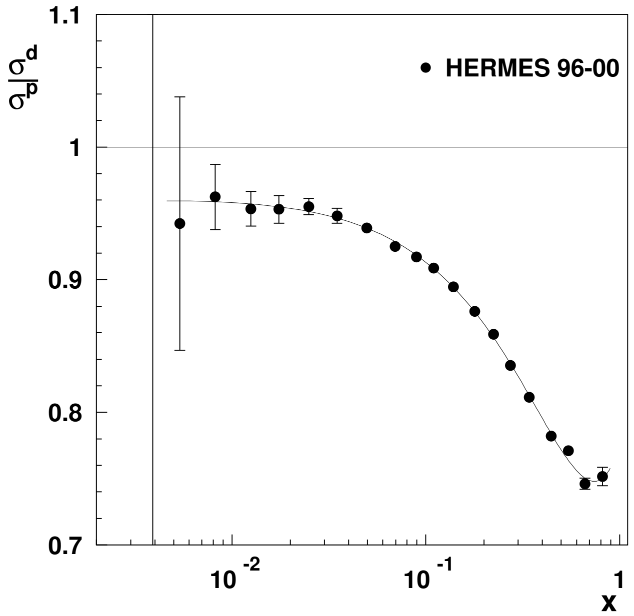

Fig. 4.9: Fit to the deuterium to proton cross-section ratio using the functional form given by equation 4.6.

section ratio within each x-bin applying the following procedure to each data point contained in that x-bin:

$$\frac{\sigma^d}{\sigma^p}(\langle x\rangle, Q^2, \epsilon) = \frac{\sigma^d}{\sigma^p}(x, Q^2, \epsilon) \cdot \frac{f_{d/p}(\langle x\rangle)}{f_{d/p}(x)}, \qquad (4.7)$$

where x corresponds to the measured value and $\langle x\rangle$ to the weighted average of x in the selected x-bin. The size of the correction is less than 0.1%.

4.6.2 Relative normalisation of the NMC and HERMES data

In order to verify the relative normalisation of the NMC and HERMES data, the measured values of σ^d/σ^p have been compared for each x-bin, using the combined representation of the data as shown in figures 4.6 and 4.7, with the requirement that the measured Q^2 values from NMC do not deviate from the HERMES Q^2 values by more than 10%. The comparison has only been made

[4] The fitting parameters obtained have the following values; $a = 0.96$, $b = -0.54$, $c = 0.30$, $d = 0.07$, $e = -0.004$

if for both data sets ϵ is larger than 0.8, otherwise the relative normalisation could be biased by a possible ϵ-dependence of the data.

For all data satisfying the aforementioned requirements the weighted average of σ^d/σ^p in the overlap region was calculated for both HERMES and NMC. These numbers were divided and fitted by a constant, the result is shown in figure 4.10. The data at lowest $x(< 0.02)$ and highest $x(> 0.4)$

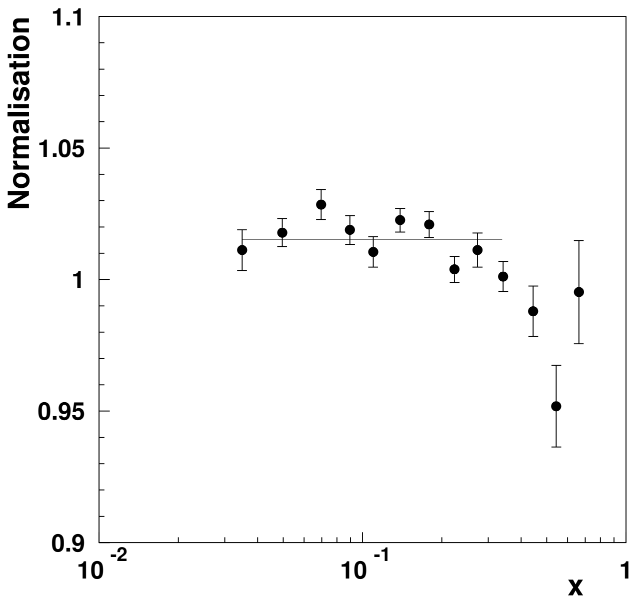

Fig. 4.10: Normalisation with respect to NMC data versus x in the overlap region in Q^2 and for $\epsilon > 0.8$.

were excluded from the fit due to a lack of overlap in ϵ (at low x) and to exclude the region where higher twist effects could occur (at large x). The obtained value for this constant is 1.017 ± 0.001. As can be seen from figure 4.10, the data at high x are systematically below the average, giving a first hint for possible higher twist effects.

Considering the small systematic uncertainty of the NMC data (0.5%) as compared to the HERMES systematic uncertainty of, on average, 2.0%, it was chosen to re-normalise the HERMES data by 1.7%. In this way both data sets are now combined in order to study the ϵ-dependence of the data. The main advantage of using both data sets in this investigation is the increased coverage in ϵ, especially at low x. Effectively, the analysis resembles a Rosenbluth separation because we make use of basically five data sets, as the NMC data have been collected at four different beam energies. The five data sets together cover beam energies from 27.5 GeV to 280 GeV.

4.6.3 Extraction of R^d/R^p and F_2^d/F_2^p

The ϵ-dependence can be used to extract information on R^d/R^p and F_2^d/F_2^p, using the following relation to fit the data.

$$\frac{\sigma^d}{\sigma^p}(\epsilon) = \frac{F_2^d}{F_2^p} \cdot \frac{(1+\epsilon k(x,Q^2)R^p)(1+R^p)}{(1+k(x,Q^2)R^p)(1+\epsilon R^p)} \quad , \tag{4.8}$$

From this equation it can be seen that the intersection of the fit at $\epsilon = 1$ yields a value for F_2^d/F_2^p, while the slope is a measure for $k(x,Q^2) = R^d/R^p$. In the fit two free parameters are used: F_2^d/F_2^p and $k(x,Q^2)$. For R^p the R1990 [47] parameterisation was used. This parameterisation is shown in figure 4.11. The ϵ-dependence of the bin-centred and renormalised HERMES data are

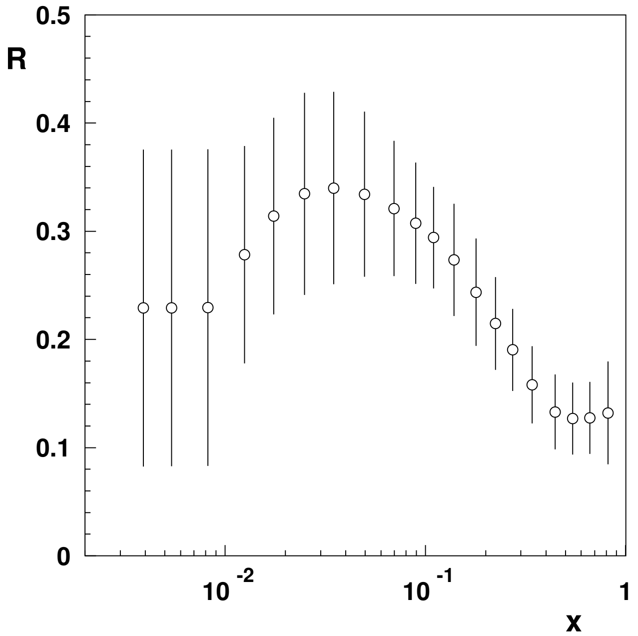

Fig. 4.11: The values of R from the R1990 parameterisation [47] evaluated at x and Q^2 values corresponding to those of the present experiment. The error bars represent the uncertainty of the parameterisation.

presented in figures 4.12 and 4.13 together with the NMC data obtained in the same (x,Q^2) range. The resulting fits obtained based on the fit to the data using equation 4.8 are shown as well. All these data were already shown in figure 4.6 and 4.7, but in this case fewer NMC data are displayed due to the required similarity in Q^2.

In the left panel of figure 4.14 the resulting F_2^d/F_2^p values are plotted versus x together with the σ^d/σ^p values, as measured directly. It is noted

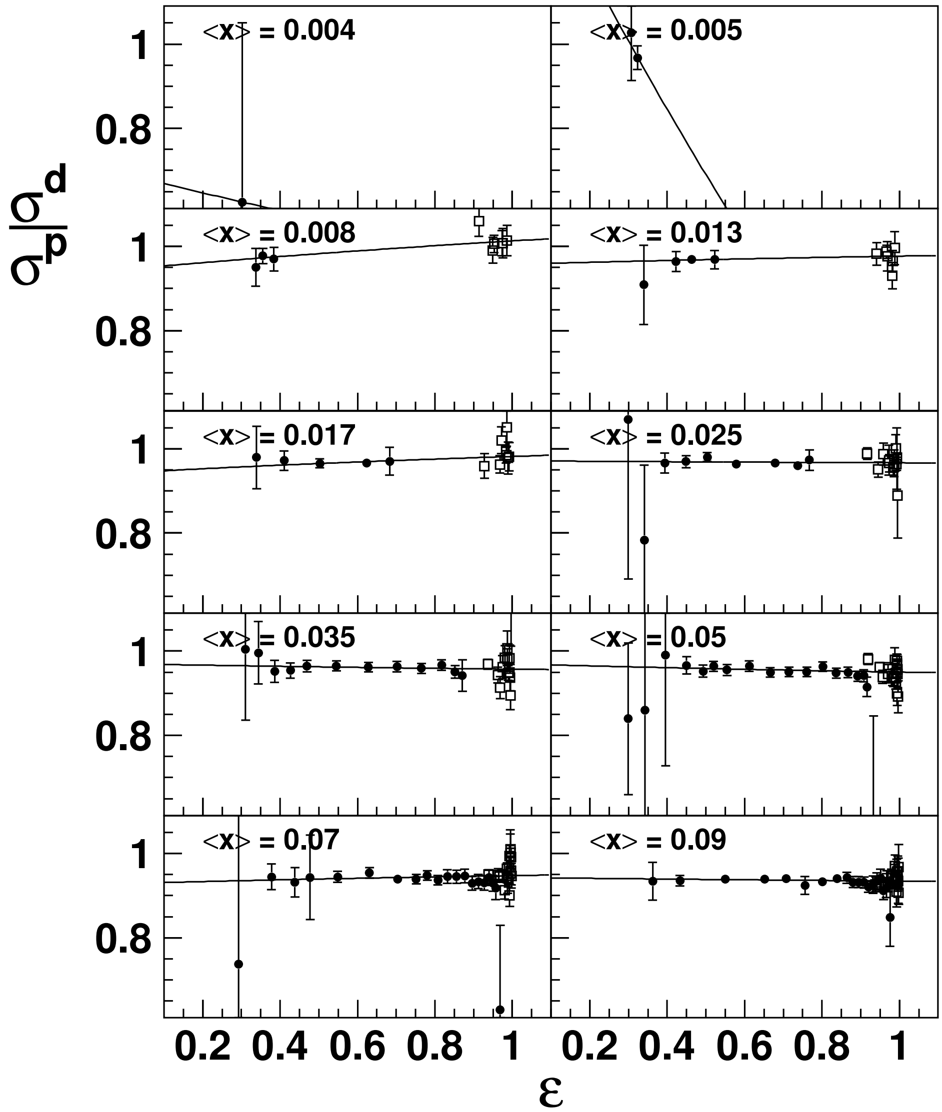

Fig. 4.12: DIS cross-section ratio per nucleon for deuterium to proton as a function of ϵ. Presented are the HERMES data (full circles) and the NMC data (open squares), which were collected at similar Q^2 values. Also shown is the fit as obtained using eq. 4.8.

that the uncertainty in the fit is very large for the first three x-bins due to the statistical uncertainty of the data. For that reason they are not shown in figure 4.14. For similar reasons no results are shown for $x > 0.4$ in the right panel of figure 4.14. In this case the short lever arm in ϵ induces large uncertainties in the fit. The upper systematic error band indicates the absolute systematic uncertainty on the direct measurement, while the lower error band represents the uncertainty on the result from the fit. The determination of the systematic errors is discussed in detail in the next section. The fact that the systematic uncertainty of the direct measurement is larger than the one of the result from the fitting procedure can be understood as follows. The direct measurement is based on HERMES data only, while the result from the fit is in addition based on the NMC data. For the extraction of F_2^d/F_2^p the NMC data dominate the result of the fit, as the NMC data are taken at high ϵ and the values of the fit at $\epsilon = 1$ determine the values of F_2^d/F_2^p. This is clear from equation 4.8. The size of the systematic uncertainty for these NMC data is very small and therefore the resulting systematic uncertainty is small. The values of F_2^d/F_2^p as determined by the two different methods are very close. Only at low x deviations can be observed due to the limitations of the fitting procedure. The similarity of the two determinations of F_2^d/F_2^p implies that $R^d \sim R^p$, which is confirmed by the results of the fit for R^d/R^p. In the right-hand panel of figure 4.14 the fitted values of R^d/R^p are presented versus x. The fact that no deviation from 1 is observed for R^d/R^p, which implies that the value for R^d does not differ from R^p, is consistent with earlier measurements. However, the present measurements extend this observation to lower values of x and Q^2 (see section 4.6.5).

4.6.4 Systematic uncertainties

The systematic uncertainties on the measured cross-section ratio have already been discussed in section 4.4.4. Here, we focus on the systematic uncertainties of the results obtained by the fitting procedure. Two independent sources can be recognised: the systematic uncertainty on the measured cross-section ratio; or more specifically to what degree the results from the fit can vary when the data points are shifted up or down with this uncertainty. Secondly, the uncertainty on the chosen parameterisation of R^p, which is presented in figure 4.11.

As the NMC data are used in the fitting procedure the question arises in what manner the systematic uncertainty on these data have to be taken into account. The main contribution to the NMC systematic uncertainty is the uncertainty in the radiative corrections, which have been calculated with the same program as used at HERMES. Therefore, when moving the HERMES data points up and down with their systematic uncertainty, the NMC data are moved in the same direction with their systematic uncertainty. By comparing the two values, obtained in this way, with the central values from the fits the final systematic uncertainty is evaluated by averaging the two differences.

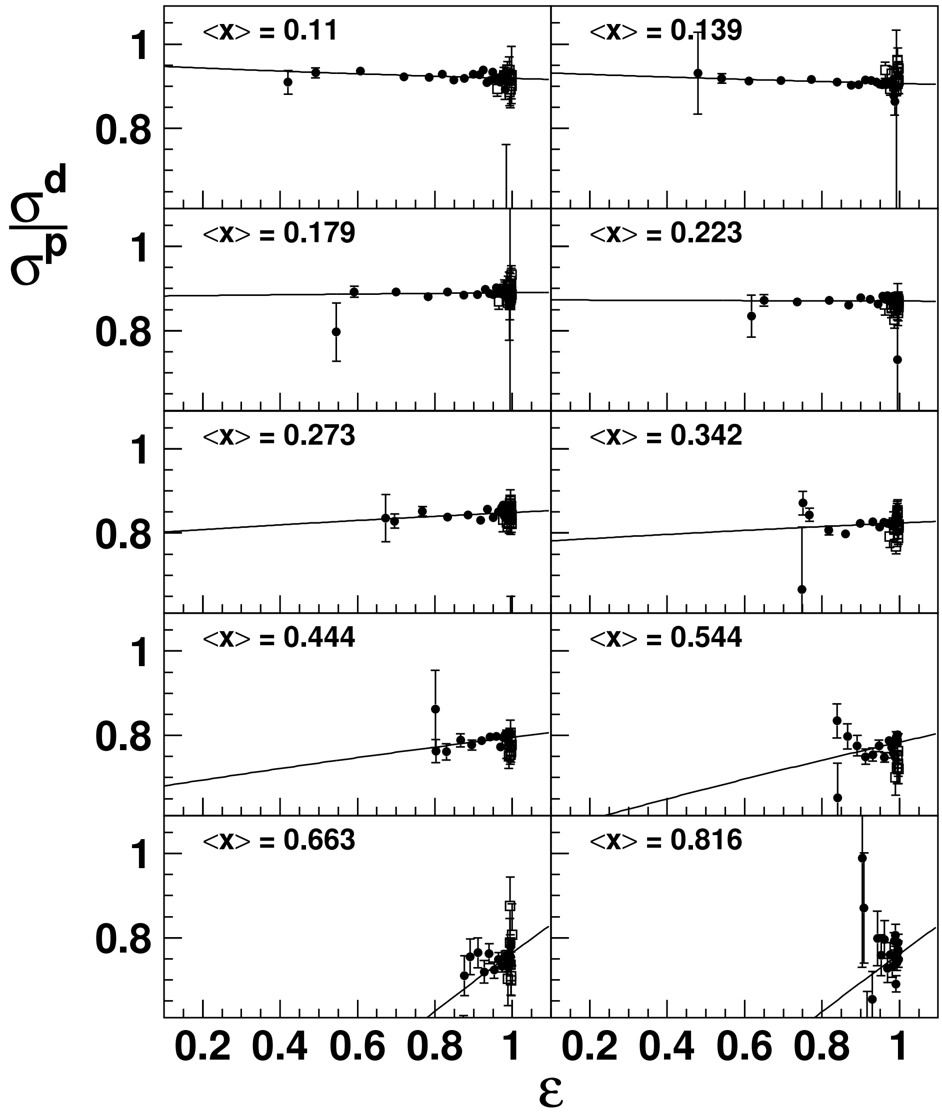

Fig. 4.13: DIS cross-section ratio per nucleon for deuterium to proton as a function of ϵ. Presented are the HERMES data (full circles) and the NMC data (open squares), which were collected at similar Q^2 values. Also shown is the fit as obtained using eq. 4.8.

The second source is the uncertainty on the parameterisation of R. The chosen value of R^p (R1990)[47] directly affects the fit results as can be seen from equation 4.8. To establish the effect of the uncertainty of R^p the fitting procedure was repeated with the value of R plus its uncertainty and R minus its uncertainty. For the region below $Q^2 = 0.35$ GeV^2, where the applicability

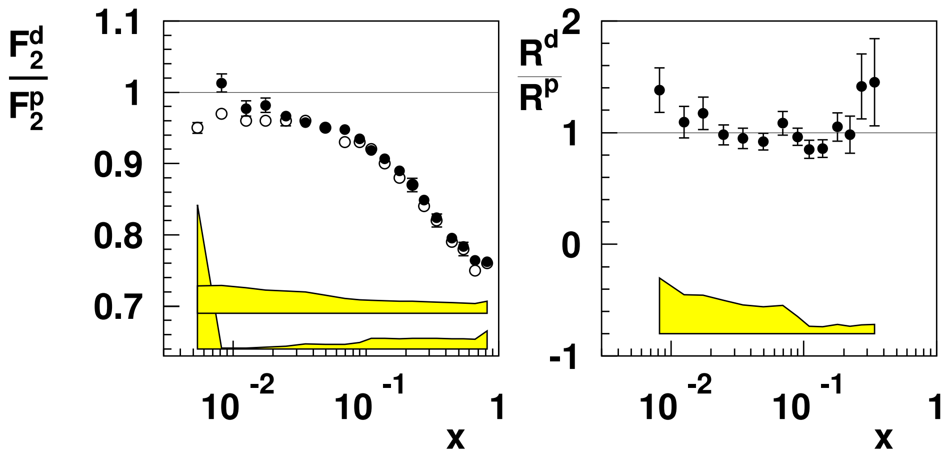

Fig. 4.14: *The results from the fit in the ϵ-domain using eq. 4.8. In the left panel the cross-section ratio σ^d/σ^p, as measured directly (open circles), is compared to the extracted structure function ratio F_2^d/F_2^p from the fit in the ϵ domain (solid circles) of the combined HERMES and NMC data. The upper error band indicates the systematic uncertainty on the direct measurement, while the lower band is the result of the uncertainties in the fitting procedure.*
In the right panel the extracted ratio R^d/R^p, as obtained from the same fitting procedure, is shown with the error band giving the uncertainties due to the fitting procedure.

of the parameterisations ceases we have used the values as given by the parameterisation anyway, as the errors are large and the effect of changing R^p is found to be minimal. The average of the difference compared to the centre value was taken to be the systematic uncertainty due to the parameterisation of R^p. Both effects were studied separately and added in quadrature as they are independent.

4.6.5 Extraction of $R^d - R^p$ and F_2^d/F_2^p

Existing data on the combination of R^d and R^p are generally presented as the difference $\Delta R = R^d - R^p$. In order to have a direct comparison between the HERMES results and the existing data, ΔR was extracted from the ϵ-dependence of the combined HERMES and NMC data. The fit was carried out using equation 4.9 with ΔR and F_2^d/F_2^p as free parameters. Equation 4.9 can be obtained from 4.8 as an approximation if only the first term in the Taylor expansion is used:

$$\frac{\sigma^d}{\sigma^p} \simeq \frac{F_2^d}{F_2^p}\left(1 - \frac{1-\epsilon}{(1+R)(1+\epsilon R)}\Delta R\right). \tag{4.9}$$

The extracted values for $\mathrm{F}_2^d/\mathrm{F}_2^p$ from equations 4.8 and 4.9 can be used to check the uncertainty introduced by using only the first term in the Taylor expansion to obtain ΔR. As the extracted values for $\mathrm{F}_2^d/\mathrm{F}_2^p$ are within 0.01% the same as those obtained from the fit using equation 4.8 it can be concluded that the methods are indeed identical and the result of ΔR carries no additional uncertainty. In figure 4.15 the results for ΔR are plotted as a function of Q^2 for different x regions. For comparison the results obtained by NMC and SLAC [1, 2] are shown as well. The systematic uncertainty, as presented by the shaded band, was obtained in the same manner as described in section 4.6.4. It is concluded that in the region of overlap very good agreement is reached with the SLAC and NMC analyses. Moreover, the present analysis provides new data at low x and low Q^2, which also show that $R \simeq 0$.

4.6.6 Extraction of σ_T^d/σ_T^p and σ_L^d/σ_L^p

Apart from showing the result of the present analysis in terms of F_2^d/F_2^p and R^d/R^p (or ΔR), it is also possible to express the results in terms of ratios of longitudinal and transverse photo-absorption cross sections. Therefore, we have rewritten equation 4.8 into the following form:

$$\frac{\sigma^d}{\sigma^p}(\epsilon) = \frac{\sigma_T^d/\sigma_T^p + \epsilon R^p \sigma_L^d/\sigma_L^p}{1+\epsilon R^p} \tag{4.10}$$

The two free parameters in the fit are σ_L^d/σ_L^p and σ_T^d/σ_T^p. This relation allows us to separate the transverse and longitudinal effects on the cross-section ratio. The results from the fit to the combined HERMES and NMC data are shown in figure 4.16. For $\sigma_\mathrm{L}^d/\sigma_\mathrm{L}^p$ the result is presented in the left panel. The ratio is constant, and close to unity, over the whole x range within the statistical and systematic uncertainties. In the right-hand panel the extracted values of $\sigma_\mathrm{T}^d/\sigma_\mathrm{T}^p$ are shown. This ratio resembles the behaviour of σ^d/σ^p.

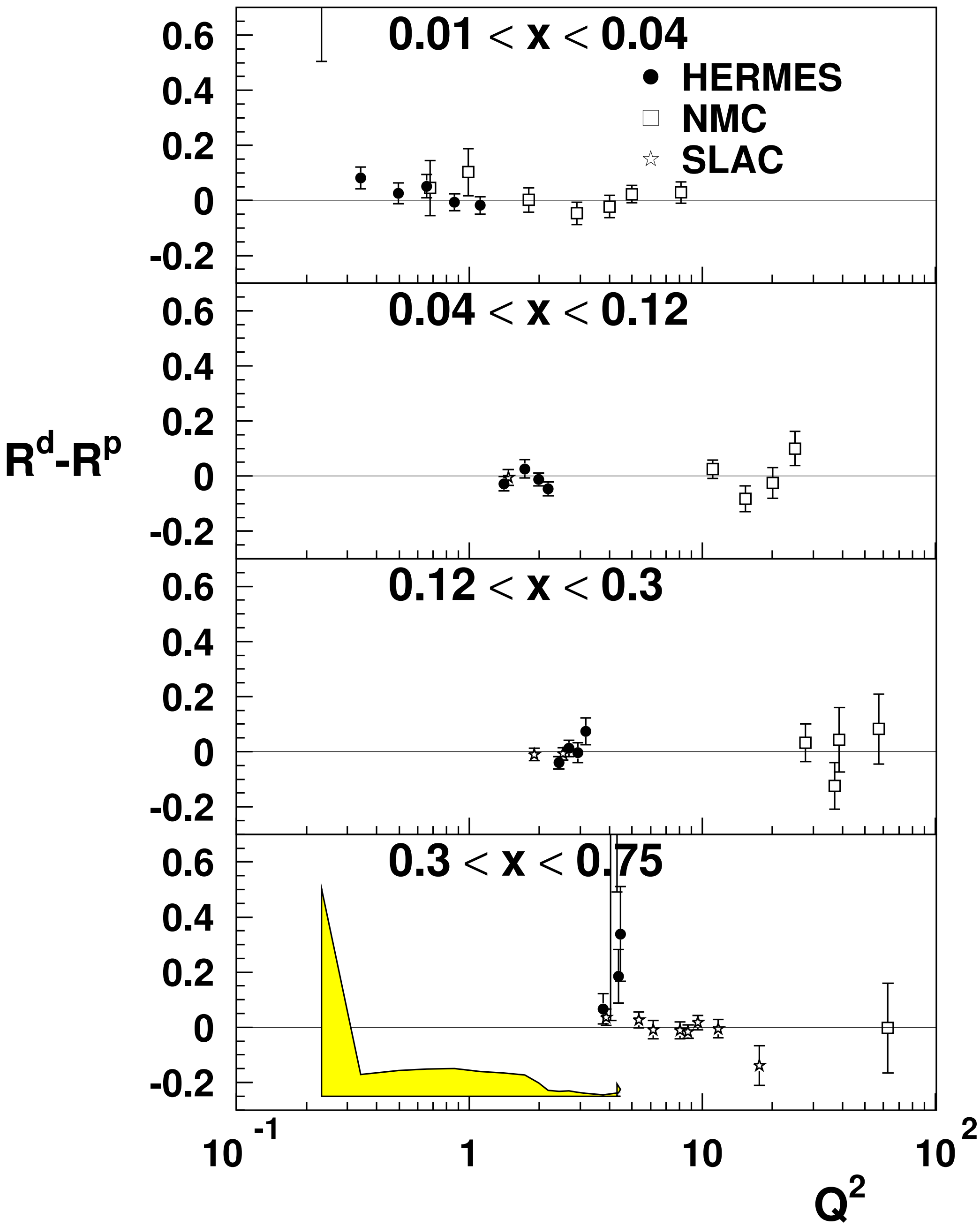

Fig. 4.15: The values of $\Delta R = R^d - R^p$ as a function of Q^2 as obtained by the present analysis of the combined HERMES and NMC data (solid circles) for different x regions compared to the values as obtained by the NMC (open squares) analysis and the SLAC global re-analysis (open stars). The error band indicates the uncertainty due to the fitting procedure.

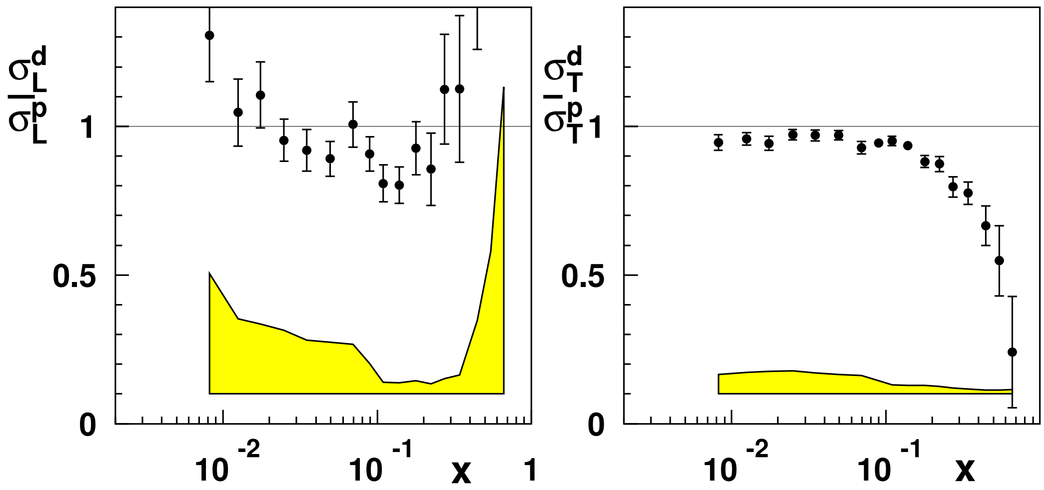

Fig. 4.16: The results of the fits using eq. 4.10. In the left-panel the results for σ_L^d/σ_L^p as a function x are presented, while in the right-hand panel the results for σ_T^d/σ_T^p are shown. The error bands indicate the uncertainties due to the fitting procedure.

4.7 Higher twist effects at high x

The possible flavour dependence of higher twist effects has been investigated at high x, where the valence quarks dominate and the difference between the proton and neutron valence quark content becomes apparent. The latter effect is clearly observed by the large deviation from unity of the cross-section ratio σ^d/σ^p or F_2^n/F_2^p presented in this chapter. At high x nuclear effects and target mass effects play a role as was mentioned in section 2.7. However, since these effects cannot be determined unambiguously, the data analyses do not include a correction for these effects to obtain a model-independent result.

To investigate whether there are higher twist effects one has to compare the experimental data with pQCD calculations performed in Next to Leading Order (NLO). These pQCD calculations are based on Parton Distribution Functions (PDF's) obtained from the fits of the currently available high energy scattering data. There is a continuing effort [48] to fit the currently available data in a QCD framework in order to obtain the most accurate description of the PDF's. These efforts result in precise F_2^d/F_2^p descriptions in leading twist (LT). As an example of this effort we mention the PDF parameterisations obtained by Botje [48]. Since most of the data, on which these parameterisations are based, have been obtained at relatively high Q^2 values, it is of interest to compare them to the present data which have been collected at relatively low Q^2 values of ~ 2 GeV^2. Such a comparison enables us to investigate whether the leading twist calculations describe the data satisfactorily, or whether possible higher twist effects contribute in certain kinematic regions. For this purpose the ratio F_2^d/F_2^p has been evaluated for both the HERMES and NMC kinematics using the PDF parameterisation of Botje [48]

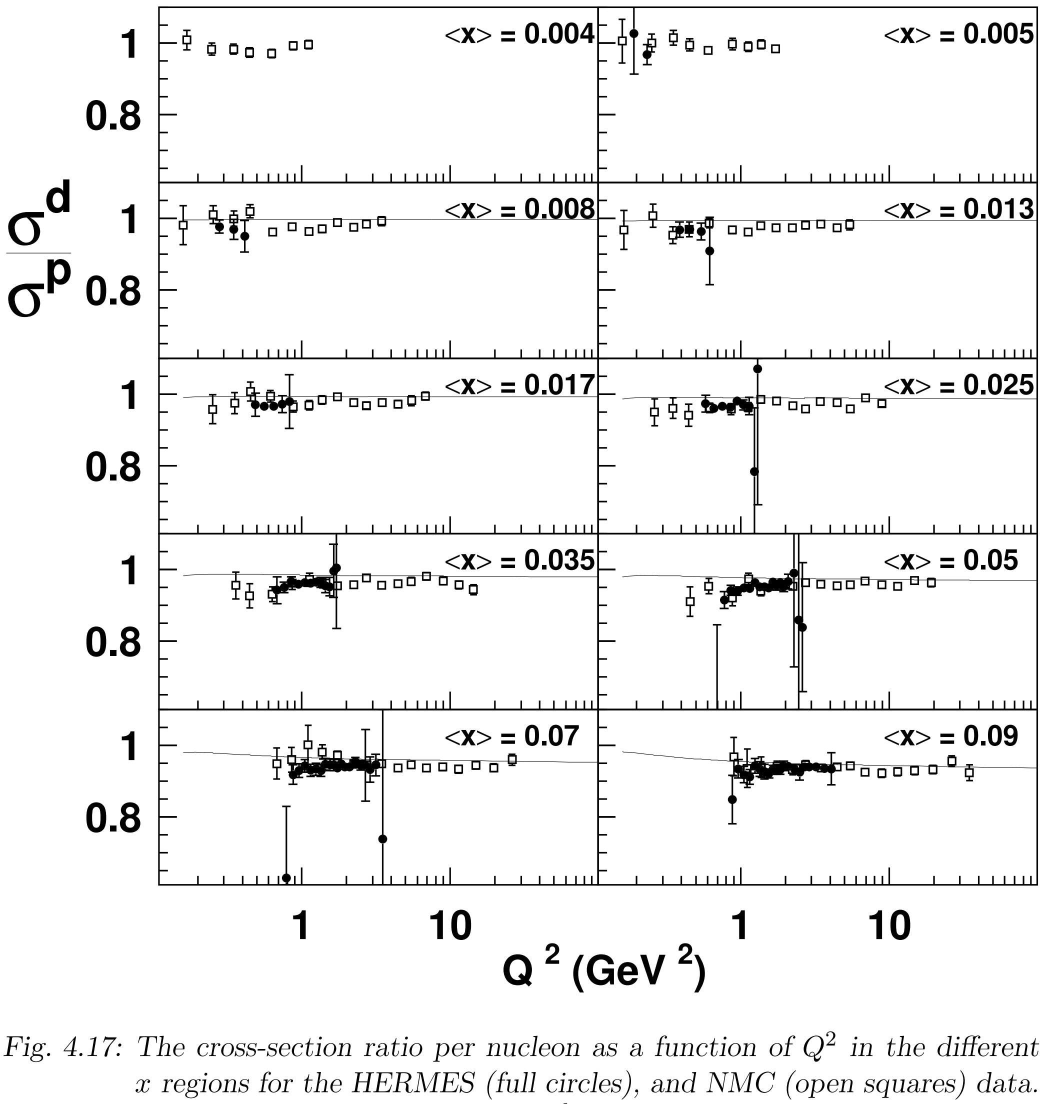

Fig. 4.17: The cross-section ratio per nucleon as a function of Q^2 in the different x regions for the HERMES (full circles), and NMC (open squares) data. Also shown is the prediction for σ^d/σ^p using the latest PDF's in a QCD framework.

In figures 4.17 and 4.18 the calculations are presented together with the

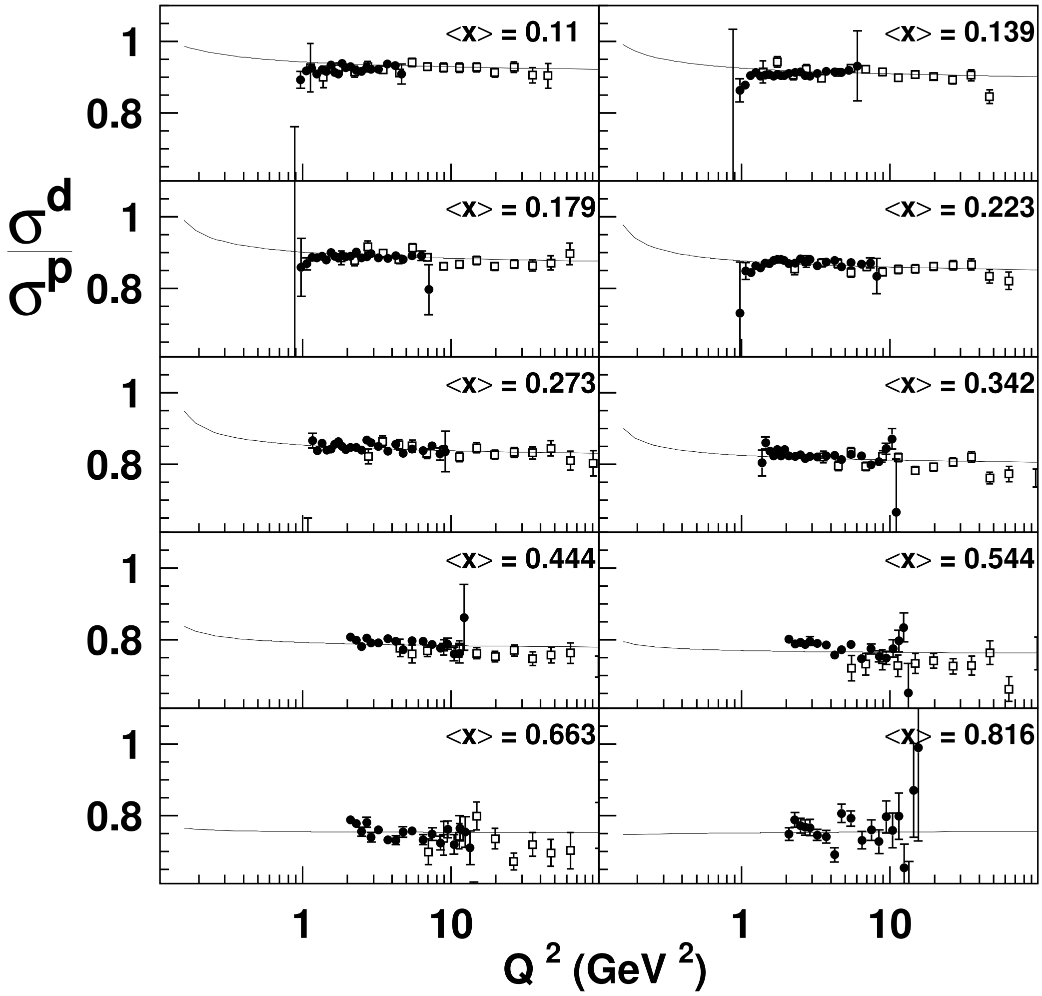

Fig. 4.18: The cross-section ratio per nucleon as a function of Q^2 in the different x regions for the HERMES (full circles), and NMC (open squares) data. Also shown is the prediction for σ^d/σ^p using the latest PDF's in a QCD framework.

HERMES and NMC data versus Q^2 for fixed x-bins. In general, there is a fairly good agreement in all x-bins. In order to search for higher twist effects the following expression is used for $F_2(x, Q^2)$:

$$F_2(x,Q^2) = F_2^{LT}(x,Q^2) \cdot \left(1 + \frac{C(x)}{Q^2}\right), \tag{4.11}$$

with $F_2^{LT}(x, Q^2)$ the leading-twist calculation based on the PDF parameterisation and $C(x)$ the contribution of higher twist terms. As we measure σ^d/σ^p, the following ratio needs to be evaluated:

$$\frac{F_2^n}{F_2^p} = \left(\frac{F_2^n}{F_2^p}\right)^{LT} \cdot \left(1 - \frac{C^p - C^n}{Q^2}\right), \tag{4.12}$$

where F_2^n/F_2^p is calculated directly from σ^d/σ^p because we have found $R^d \simeq R^p$. In this procedure we can only extract higher twist effects which are different for the neutron and the proton. The extracted value of $C^p - C^n$ has been obtained by a minimisation procedure comparing the data to the calculated values. The results are presented in figure 4.19. In the left panel results are presented which are obtained using one of the most recent parameterisations for the PDF's [48], while the result shown in the right panel was obtained with the MRSA [49] PDF's as input. A similar result was

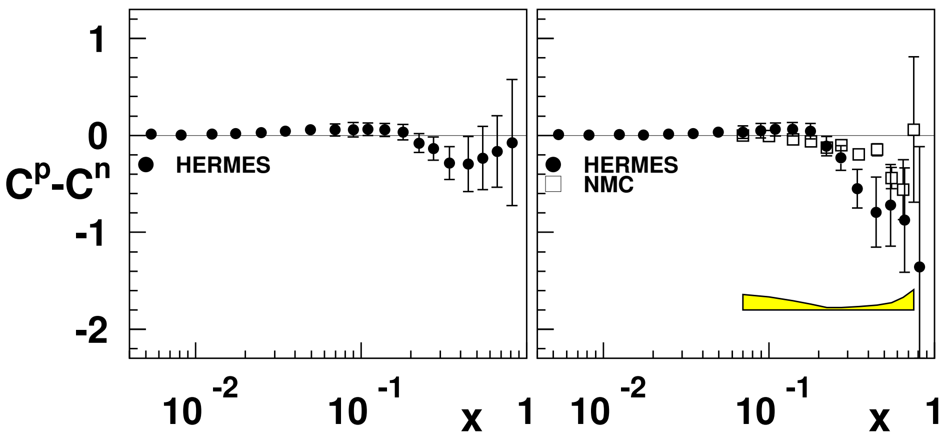

Fig. 4.19: Possible higher twist effects extracted from a comparison between data and QCD predictions. The results shown in the left-hand panel were obtained using the latest PDF's [48]. The results in the right-hand panel were obtained with the older MRSA PDF's as input. Also, the NMC results on $C^p - C^n$ are shown.

obtained by NMC (also using the MRSA PDF's) combining NMC, BCDSM, and SLAC data. The NMC results are plotted in the right panel as well.

For the HERMES data the error bars shown represent both the statistical and sytematical uncertainties as in the fitting procedure these two components cannot be properly separated. The error band shown in the right-hand plot applies to the NMC data. Taking the uncertainties into account the two results shown in the right panel are in qualitative agreement. If the more recent PDF's of Botje are used, a small deviation of $C^p - C^n$ from zero remains, which is, however, barely significant. It is concluded that no unambiguous evidence for flavour-dependent higher twist effects can be found from these data.

4.8 The Gottfried sum rule

In section 2.6 the Gottfried Sum Rule (GSR) was introduced, which relates the difference between the proton and neutron structure functions $F_2^p(x)$ and $F_2^n(x)$ to a possible isospin asymmetry of the sea quarks. The NMC experiment [50] found a significant deviation from 1/3, the value of the GSR expected if $\overline{u}(x) = \overline{d}(x)$. It was concluded that the $\overline{u}$ and $\overline{d}$ contents of the sea are not equal. Here, the first determination of the GSR by the HERMES experiment is presented, based on the measured values of F_2^d/F_2^p and the parameterisation of the world data for F_2^d. As compared to NMC, the GSR value obtained by HERMES is evaluated at a lower Q^2 value, thus enabling the investigation of a possible Q^2 dependence of the GSR. The GSR is defined

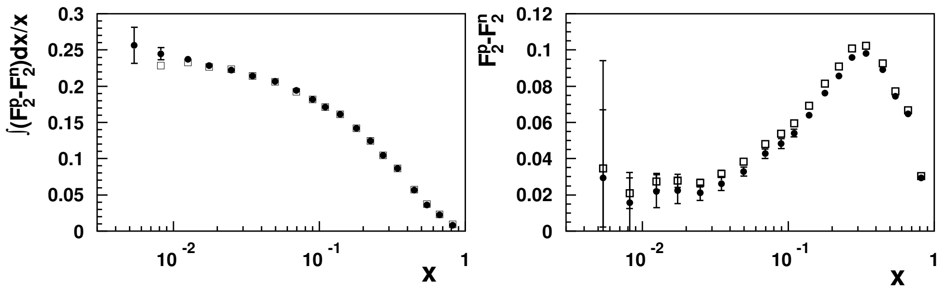

Fig. 4.20: Value of the GSR integral with a running lower limit x_{min} set equal to the x-value of that bin (left panel). The value of $F_2^n - F_2^p$ is shown in the right panel. The NMC data are shown for comparison (open squares).

as:

$$S_{GSR} = \int_0^1 \frac{1}{x}(F_2^p(x) - F_2^n(x))\mathrm{d}x \qquad (4.13)$$

and was calculated using the following expression:

$$S_{GSR} \quad = \quad \int_{0.005}^{0.75} 2F_2^d(x)\left(\frac{1 - F_2^d(x)/F_2^p(x)}{F_2^d(x)/F_2^p(x)}\right)\frac{\mathrm{d}x}{x} \qquad (4.14)$$

at an average value of Q^2 of 2 GeV^2. The obtained value of the GSR integral is

$$S_{GSR} \quad = \quad 0.256 \pm 0.025 \text{ (stat)} \pm 0.023 \text{ (sys)}.$$

The result is in agreement with the NMC result:

$$S_{GSR}^{NMC} \quad = \quad 0.2281 \pm 0.0065 \text{ (stat)}.$$

To illustrate the evolution of the integral of $F_2^n - F_2^p$ the value of the running integral is shown in the left panel of figure 4.20. At low x the behaviour is rather flat, which indicates that with the extension over the whole x-range towards lower x no significant contribution to the integrand can be expected. At high x the decrease of the difference, $F_2^n - F_2^p$, also reduces the significance of the inclusion of the region up to $x = 1$. Therefore, if the whole x domain would be considered still a deviation from the originally expected value of 1/3 would be obtained. In the right panel of the same figure the difference $F_2^n - F_2^p$ is presented as evaluated in the same way as for the integrand in equation 4.14. A comparison between the results of the present analysis and the NMC data is shown, which shows a good agreement. It is noted that the NMC value was obtained by integrating over x from 0.004 to 0.8. It can be concluded that over a similar range in x, but at an average Q^2 which is a factor of two lower, the deviation from the GSR is essentially the same. Therefore, the difference between the $\overline{u}$ and $\overline{d}$ distributions seems to be the same in the two different Q^2 regions probed by the NMC and HERMES experiments.

4.9 Concluding remarks

The presented analysis has resulted in several results, which have increased the knowledge of the ratio of the structures functions F_2^d and F_2^p. A large number of events was analysed, resulting in a small statistical uncertainty. The systematic uncertainty is of the order of 2%, but somewhat larger at low x mainly due to the uncertainty in the determination of the radiative corrections. Since the HERMES experiment was not designed for studies as discussed in this chapter, the results are surprisingly precise. This enabled a detailed comparison with the precise NMC data obtained at larger average

Q^2 values. The combination with the NMC data made it possible to determine the difference, ΔR, between the ratio of the longitudinal to transverse photo-absorption cross section ratios on the deuteron (R^d) and the proton (R^p). The new data are consistent with zero, which is in agreement with previous results obtained for $\Delta R(= R^d - R^p)$. By studying the Q^2-dependence of F_2^d/F_2^p in comparison with QCD predictions based on recent particle distribution functions an investigation of higher twist effects was performed. A hint for higher twist effects, that are different in the deuteron relative to the proton, was found, but the small size of the effect and the associated margins of uncertainty make it impossible to draw unambiguous conclusions.

The Gottfried Sum Rule was determined over the measured x-domain. A value was obtained similar to the one extracted by NMC, but at an, on average, lower Q^2 value. From the results on F_2^d/F_2^p, as obtained through

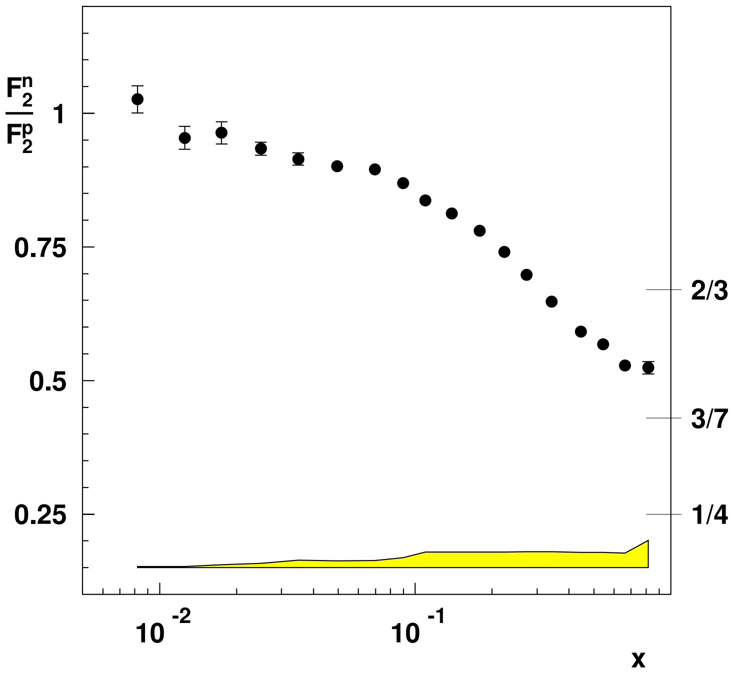

Fig. 4.21: The F_2^n/F_2^p result from the fits in the ϵ-domain compared to the predictions for $x \to 1$ discussed in section 2.7.

fitting the combined HERMES and NMC data, we can directly calculate F_2^n/F_2^p and compare the result to the theoretical predictions presented for high x in section 2.7. In figure 4.21 the results for F_2^n/F_2^p are presented. It can be seen that the current data yield results for $x \to 1$ that are close to the QCD predictions for F_2^n/F_2^p at $x = 1$, i.e. 3/7 especially if it is realised that the data possibly need to be corrected for higher-twist effects that would reduce F_2^n/F_2^p. However, as long as no corrections are applied for possible higher twist effects, off-shell effects (of the neutron in deuterium) and other nuclear effects, it is hard to draw definite conclusions. In order to avoid such uncertainties it is desirable to measure the same quantity using the tagging method to extract $F_2^n\rfloor_{tag}/F_2^p$. This subject is discussed in the next chapter.

5. THE SILICON TEST COUNTER

5.1 Introduction

The HERMES Silicon Test Counter (STC) was developed in 1997 and 1998 and was part of the HERMES experimental setup during the fall of 1998. It consisted of two layers of double-sided silicon and was positioned beneath the centre of the internal target-cell inside the vacuum chamber. This prototype detector was made to verify the feasibility of operating silicon detectors in the harsh environment of the HERMES lepton-scattering interaction area. In view of the plans (that were later realised) to install two large arrays of silicon detectors surrounding the HERMES target, it was crucial to demonstrate that neither the ultra high vacuum requirements nor the RF of the beam or the high radiation levels prevented the operation of such systems. The STC was positioned at such a position that it could be used to observe recoil protons produced in Deep Inelastic Scattering (DIS). As a result the STC might also provide a 'proof of principle' of recoil detection in DIS, a subject long debated in literature [51, 52, 53].

More specifically with a recoil detector several new physics topics can be studied:

- The measurement of the momentum distribution of nucleons in deuterium in DIS by detecting spectator protons of DIS events on the neutron in deuterium and determining their momentum. A comparison can be made with similar data obtained in quasi-elastic electron scattering (QES) at a considerably lower incident energy. In case it can be shown that the momentum distribution derived from DIS and QES are similar, it proves the feasibility of recoil detection in DIS, thus enabling the use of recoil detection as a tool to observe tagged structure functions in DIS. Furthermore, possible differences between the momentum distributions from DIS and QES may shed light on the relative importance of contaminating processes (such as final-state interactions and exchange currents) in the reactions.

- The extraction of the tagged neutron structure function $F_2^n\rfloor_{tag}$ from DIS and recoil detection data on deuterium. In practice the ratio

$F_2^n\rfloor_{tag}/F_2^p$ is obtained, which can be compared to F_2^n/F_2^p data, derived from inclusive DIS on deuteron and hydrogen targets (see Chapter 4). As was discussed in section 4.9 the ratio F_2^n/F_2^p derived from inclusive DIS data is difficult to interpret in the limit $x \to 1$, where explicit predictions exist (see section 2.7), because of uncertainties related to nuclear (binding) effects in deuterium. However, the use of a recoil detector allows the tagging of DIS events on the neutron in the deuteron, by identifying the spectator proton, thus offering nucleon momentum information, which can be used to reduce the uncertainties due to the nuclear binding effects. Furthermore, the determination of a tagged structure function makes it possible to study the nuclear momentum dependence of $F_2^n\rfloor_{tag}$ by determining $F_2^n\rfloor_{tag}/F_2^p$ for different recoil momentum bins. This is of interest as a momentum dependence of F_2 could be at the origin of the EMC-effect. In this chapter a first attempt is made to extract $F_2^n\rfloor_{tag}/F_2^p$ and its momentum dependence.

Other physics issues that can be addressed with a recoil detector are the study of target fragmentation products, deep virtual Compton scattering, and other exclusive processes and colour transparency. All these topics are described in more detail in [51, 54]

In this chapter the design considerations of the STC and their implementation are presented in sections 5.2, 5.3, 5.4, 5.5, and 5.6. Following this technical overview of the system the signal extraction and energy calibration of the silicon counters is explained in section 5.7. As the data showed that it was possible to operate the STC at HERMES, in the concluding section an attempt is presented to extract data on the nucleon momentum distribution and the structure function ratio $F_2^n\rfloor_{tag}/F_2^p$.

5.2 Design considerations

As mentioned in the previous section, the STC was positioned underneath the target cell, through which the electron beam passes. The closeness of the open-ended internal cryogenic target-cell and the electron beam and also the ultra-high vacuum of the HERA beam-line posed several restrictions on the design of the detector and the materials which could be used.

- The materials used had to satisfy the out-gassing requirements, set by the HERA vacuum group. The allowed contribution to the pressure at the location of the HERMES target corresponds to a background pressure of 10^{-7} mbar. This is to ensure that the passing of the beam through the HERMES area would not be hindered by an additional gas load, leading to a reduced beam life time. In particular the outgassing of gases, which can not be pumped away easily, or those which might have detrimental effects on the pumping system used, should be avoided. In addition, it is necessary to keep the amount of gas in the target chamber as low as possible since this could negatively influence the purity and the high polarisation of the HERMES target. Moreover, the electronic components had to be able to withstand a high level of radiation to avoid a breakdown of the front-end part of the readout chain. For all these reasons normal printed circuit boards (PCBs) could not be used. Instead, kapton was chosen as base material for the PCBs. The kapton was glued to a copper plate for stability as well as cooling. The glues and insulating materials used were carefully selected and tested. Details are given in [55]. For the cabling, kapton-coated wire was taken.

- The passing of the electron beam in bursts of 26 ps produces a wide-band radio-frequency (RF) spectrum. In principle, the target and the wake-field suppressor are designed to keep the RF inside the beam pipe. However, the pumping holes in the target-cell and the openings in the wake-field suppressor allow certain frequencies to enter the target chamber. To prevent the RF in the target chamber from influencing the silicon detector and front-end electronics placed there, the detector and front-end electronics should be surrounded by an enclosure (Faraday cage), which is reduced to an open grid in the line of sight to the target (see figure 5.1).

- Since there is very little heat dissipation in the vacuum the heat produced by the readout electronics will cause an increase in temperature of the entire system. In order to prevent a breakdown at high temperatures the electronic components have to be cooled by direct contact. In this case the use of a cold bar was chosen. Also, a cooled environment is preferable for the operation of silicon detectors as the effect of radiation damage to silicon is less pronounced at low ($< 0\ ^{\circ}C$) temperatures .

- The limited space available in the target chamber complicated the design as the method of installation had to be considered as well as the routing of the signal cables and the cold bar. In this respect, it has to be realised that the HERMES internal target and the STC had to be installed simultaneously, while they both have separate cooling and electronic systems.

5.3 Detector mechanics

The outcome of the design effort was a detector system as presented in figure 5.1. A small ($421 \times 142 \times 63$ mm^3) box with the open top side covered by a woven mesh of perpendicular wires with a spacing of 5 mm between the wires. These wires are made of beryllium copper (CuBe) and have a thickness of 125 μm. The cooling bar was part of the support structure of the silicon detector. The actual cooling was done by conduction. A cold bar,

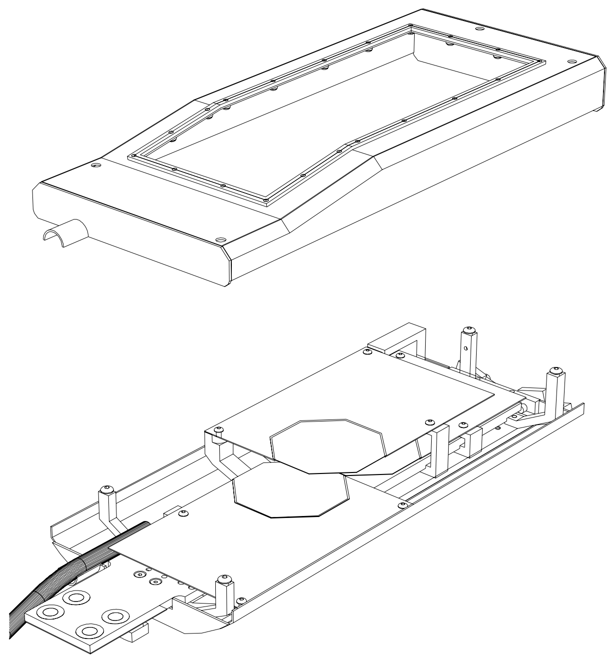

Fig. 5.1: Three-dimensional view of the HERMES Silicon Test Counter (STC). The top part of the graph shows the cover plate including the open grid with a spacing of 5×5 mm^2. In the bottom part the following parts can be identified: octagonal silicon detectors supported by rectangular carrier boards, cabling (black) and the cold bar extending from below the counters. The overall scale of the STC is $421 \times 142 \times 63$ mm^3.

situated outside the vacuum chamber in a secondary vacuum, was connected by a copper (OFHC) bar, via an electrically insulating piece of aluminium nitride to the aforementioned copper support structure of the carrier boards. The cold bar was cooled by a system using Peltier elements. The cooling power available was $\sim$ 150W at 0 $°C$. The whole structure was positioned on three pins, which were welded to the vacuum chamber. The obtained positioning precision was of the order of 3 mm. The top silicon detector was 6 cm below the centre of the target-cell. The second layer of silicon detectors was positioned 1.5 cm below the top one. The detectors used for tracking and particle identification were double-sided silicon strip detectors. A recoil proton passing through two detectors with double-sided readout provides the four coordinates necessary to reconstruct the track of the particle. Energy information is obtained by using the two silicon detectors as $\Delta E - \Delta E$ counters using the analog signal produced by both counters.

5.4 Silicon

The choice of silicon detectors, as we are considering a prototype, was limited to silicon detectors readily available at one of the manufacturers. The main consideration was to have two layers of double sided silicon, where the top layer had to be relatively thin to allow for particles with low momentum to pass this first layer and reach the second layer. Eventually one thin (135 μm) detector was chosen for the top layer, while for the bottom layer two different detectors were selected. In the backward region relative to the centre of the target and the beam direction an equally thin detector was positioned, while for the forward region we opted for a thick (306 μm) detector. The specifications of the silicon detectors are given in table 5.1.

Silicon detector properties	
shape	octagonal
thickness	135, 136, 306 μm
silicon type	double sided
strip pitch	1 mm
strip pattern	orthogonal
size	64 x 64 mm^2
strip coupling	DC
depletion Voltage	28, 27, 54 V
$I_{leakage}$ @ -15 $°C$	0.4, 0.4, 1.0 μA

Tab. 5.1: Properties of the silicon detectors used in the STC.

5.5 Electronics

For the collection of the signals from the silicon detector the Analog Pipeline Chip (APC) was chosen. The main advantage of this 64-channel chip is its large dynamic range, which enables the observation of both the slow recoils (with momenta down to 100 MeV/c) and fast particles ($300 < p < 1400$ MeV/c). The APC was well known from its use in the vertex chambers, which were part of the HERMES setup and also built at NIKHEF [28]. In addition, the APC's needed were readily available at NIKHEF.

The APC's were operated at the HERA bunch crossing frequency of 10.4 MHz. They have 64 channels, which integrate the charge from the silicon strips. This integrated charge is sampled at the bunch crossing frequency and stored in a circular buffer with a depth of 32 cells (pipeline), allowing a trigger latency of several microseconds. Upon receipt of a trigger, two samples are retrieved form the circular buffer: one from just before the passing of a particle and the other from right after the passage. The difference of these two samples is a measure of the charge deposited in the detector by the passing particle. By choosing the two sampling points carefully a good signal can be obtained. The APC's and the electronic components needed to process the signal were placed on the kapton printed circuit boards, supported by copper plates as mentioned before. In total there were three carrier boards with on each side an APC with 64 channels, adding up to 384 channels. Each APC was read out by its own ADC. To ensure optimal performance the electronics were grounded from outside the vacuum and no electrically conducting connections were made with the immediate surroundings. The electronics were housed inside the metal cage and the cables were shielded by a fine mesh, thus forming a Faraday cage around the active electronics up to the flange to protect the small (100 mV) signals from noise influences. A balanced signal output was chosen to further enhance the noise immunity. The ADCs used were the CAEN V676, a 10 bit ADC, working at 10 MHz, which was positioned 30 metres away in the electronics trailer.

5.6 Operation of the STC

During the operation and the installation of the STC several accidents occurred, which decreased the potential of the detector and in the end rendered it inoperable. Three APC's of the six initially in operation broke down due to discharges of static electricity. This was caused by the extremely dry environment in which the detector was installed and facilitated by (in hindsight) insufficient electronic protection of the APC's. The other three chips were operated successfully for several months, until the radiation resulting from the loss of an erratic HERA electron beam in the vicinity of the HERMES interaction point, caused significant damage. The chips became inoperable, along with the APC's used in the vertex chambers at HERMES and the silicon vertex detector [56] at the H1 experiment. A glass dosimeter had been installed near the detector and it was analysed afterwards. It had collected about 65 kGy of radiation, while the APC's are believed to be operable up to only 0.8 kGy [57].

5.7 Results

The results obtained from the present analysis of the STC data is described in this section. A first analysis of the data, which was limited to a proof of principle and did not include the extraction of the physics quantities introduced in section 5.1, was performed by K. Fiedler [58]. The present results supersede those of Fiedler. First the event selection and the synchronisation with the HERMES spectrometer data is covered. Thereafter, the signal processing and the energy calibration is discussed. The extraction of the nucleon momentum distribution in the deuteron is presented in section 5.8, while the structure-function ratio $F_2^n\rfloor_{tag}/F_2^p$ is presented in the last section of this chapter.

5.7.1 Event selection

To select events in the STC data that correspond with a DIS event, first an inclusive analysis of the HERMES data was carried out, similar to the one presented in chapter 4. The data quality requirements were less stringent as compared to the inclusive analysis presented in chapter 4, since only little STC data are available. The selected events were used as an input list for possible interesting STC events. A total of 0.34 million events on hydrogen were selected, while on deuterium, polarised and unpolarised combined, nearly 1.3 million events were available.

Before analysing the events, a baseline of the APC had to be established for each strip, as the APC has a different baseline for each channel. This had to be done for each run as the conditions vary form run to run, possibly resulting in a different baseline. To obtain the baseline for each run and for each strip 1000 events were selected, in which the strip was not hit. The distribution formed by these 1000 events was fitted with a gaussian to get the mean and the width. The obtained mean was taken to be the baseline for the run analysed, while the width was used as a base measure of the threshold. In practice, the threshold was set at five times the width (expressed in terms of the sigma of the Gaussian) above the mean for the present analysis. In this way most noise and minimum-ionising events were removed from our sample. The five-sigma threshold corresponds to $\simeq$ 200 keV or $\simeq$ 250 keV depending on the detector hit, which is significantly more than the energy deposited by a minimum-ionising particle of about 100 keV. The event selection of possible spectator proton events was performed by requiring, for every event in the DIS event list, at least one strip for one of the three detector planes to be higher than the applied threshold.

5.7.2 Signal processing

After the selection of events the hit strips were 'clustered', where possible, to obtain the most accurate position of the passing particle and to take all the deposited energy into account. In this procedure no gaps were allowed in a cluster. The total deposited charge is given by:

$$q_{tot} = \sum_{i=n-1}^{i=n+1} q_i \tag{5.1}$$

The centre of gravity of the cluster was determined and stored as the hit position, while the integrated cluster charge was stored as the deposited energy. For the bottom detector the signals were doubled as only half the balanced signal was read out. The clusters were in more than 90% of the clusters determined by just one strip.

5.7.3 Data quality and acceptance cuts

Several plots are shown in order to check the data quality and the acceptance of the STC. Furthermore, the synchronisation between the HERMES and STC data stream was verified. First, the hit position determined by the strips of the top and bottom sides of the top detector should give the orthogonal detector shape as illustrated in the right-hand panel of figure 5.2. The charge collected by the top side should be nearly the same as that obtained by the bottom side of the top detector, giving a linear relation between the two quantities, which is made clear in the lower right hand panel of figure 5.2.

When involving the HERMES spectrometer data in the analysis the proper synchronisation of the STC and HERMES data can be verified. In the top left panel of figure 5.2 the z-vertex position, as determined by the scattered electron in the HERMES spectrometer, is plotted versus the z-position of the hit in the top detector of the STC, requiring also that charge has been deposited in the second layer. The area in which possible hits can occur is enclosed by the drawn lines. The fact that there are only a limited number

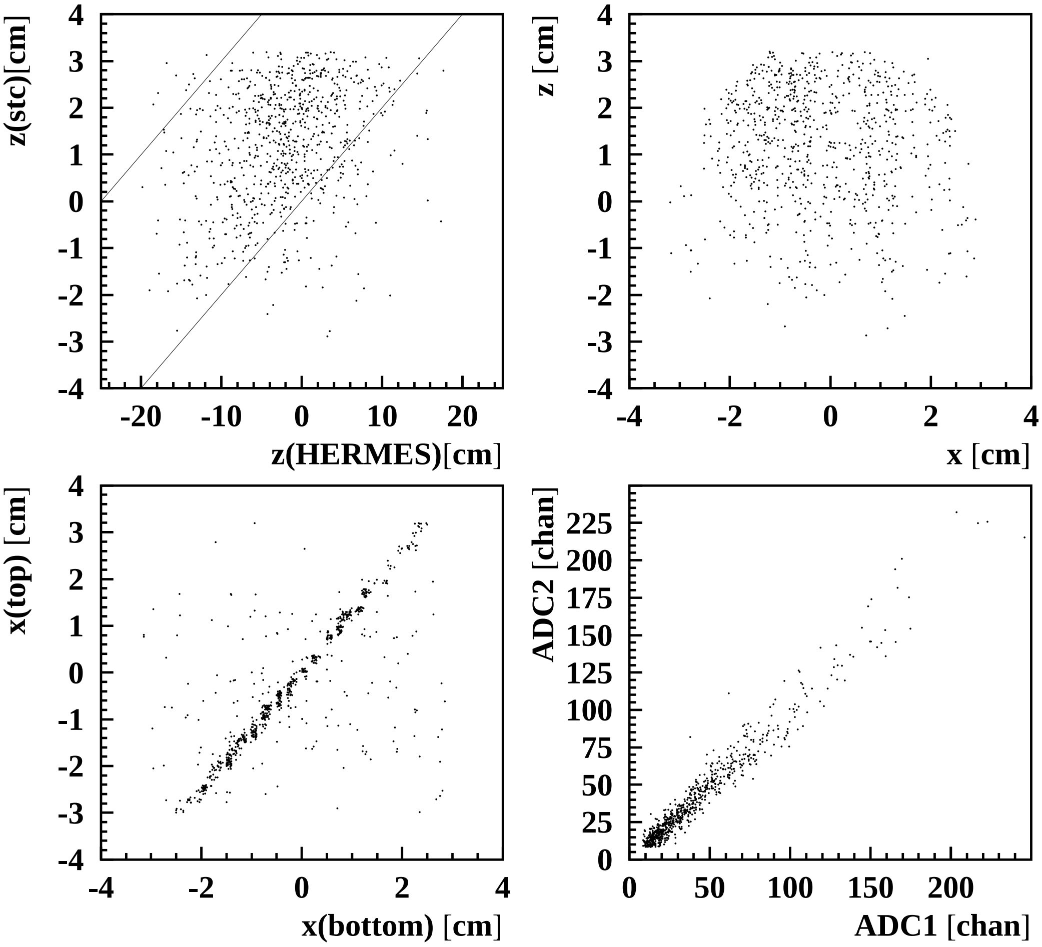

Fig. 5.2: Correlation plots between the z and x strips of the two detector planes, labelled as 'top' and 'bottom'. In the top left plot the z-vertex as provided by scattered electron observed by the HERMES detector is used in the absence of z-information from the bottom detector. In the bottom right plot the charge correlation of the top plane is shown.

of hits (noise) outside this area proves that the synchronisation of the two data-streams is correct.

5.7.4 The reconstruction of the x-vertex

From the x-hit position in both the top and the bottom layers of the STC the x-vertex position can be reconstructed.

$$x_{vertex} = x_{top} - (x_{bottom} - x_{top})\frac{\Delta Y_1}{\Delta Y_2} \tag{5.2}$$

with $\Delta Y_1 = 6.0$ cm, the distance from the centre of the target to the first plane and $\Delta Y_2 = 1.5$ cm, the distance between the two silicon planes. In figure 5.3 the resulting distribution is seen. This distribution presents a proper vertex reconstruction, which indicates that the STC worked well. Unfortunately a similar result could not be obtained for the z-vertex, due to the broken APC's. If operational a z-vertex distribution obtained with a nearby silicon detector could be a significant improvement with respect to the current accuracy of z-vertex position, as determined by the HERMES spectrometer, of about 2 cm.

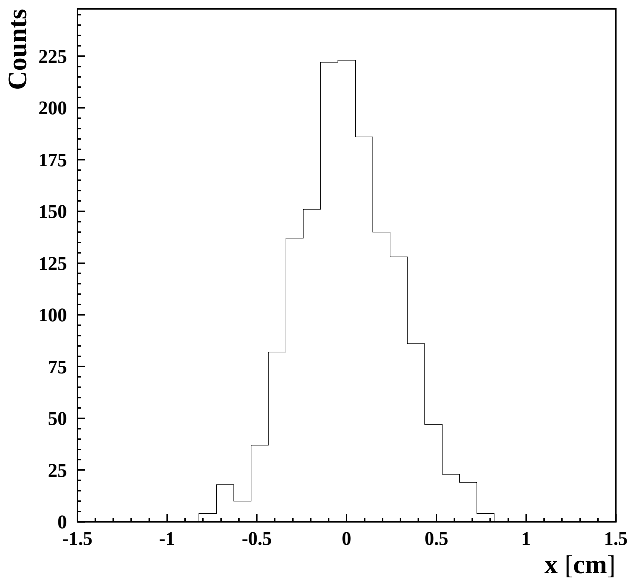

Fig. 5.3: Reconstructed x-vertex from the STC data.

5.7.5 Angular distributions

To perform the energy calibration we need to know the incidence angle of the incoming particle. To obtain this, the polar angle θ and the azimuthal angle ϕ of the recoil particle are calculated in the HERMES coordinate system using the following expressions:

$$\theta = \frac{\pi}{2} - \text{atan}([z_{top} - z_{vertex}]/\Delta Y_1) \tag{5.3}$$

$$\phi = \frac{3\pi}{2} + \text{atan}([x_{bottom} - x_{top}]/\Delta Y_2) \tag{5.4}$$

The incidence angle α with respect to the perpendicular on the plane of the STC is given by:

$$\alpha = \pi - \text{acos}(\sin\theta \cdot \sin\phi) \tag{5.5}$$

In figure 5.4 the three angular distributions are presented. The distributions

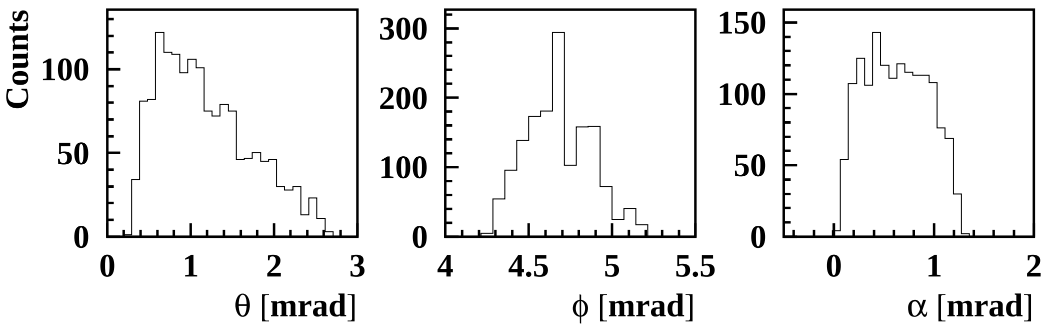

Fig. 5.4: Angular distributions as a function of θ, ϕ, and α.

presented show the expected shape, at least qualitatively. The ϕ distribution is symmetrical, as expected from the symmetric ϕ-acceptance of the STC, while for the θ distribution the acceptance in the backward region is clearly smaller, which can be understood from the geometry of the two detector planes. The α-distribution gives the angle with respect to the vertical. The distributions can be reproduced in Monte Carlo studies as shown in reference [58].

5.7.6 Energy calibration

To extract the energy deposited in the silicon detectors from the signal obtained in the ADC channels we use the correlation between the deposited energy in the two detectors. The deposited charge in the two planes was plotted, as shown in figure 5.5, and compared to the theoretical curve. The deposited charge was changed for the angle of incidence with the following factor:

$$C_{eff} = C_{exp} \cdot \cos(0.78 \cdot \alpha), \tag{5.6}$$

with α as introduced in the previous subsection. The factor 0.78 is introduced to compare the data with the curve determined for particles which traverse the silicon perpendicular to the surface. In principle, one should bin the obtained events in α and compare with the appropriate curve. However, the statistics available do not allow this.

It is derived from equation 5.7, written below, by comparing the exact energy loss as a function of α with the energy loss as a function of α multiplied by a fixed factor. One can write the thickness, t, in equation 5.7 as a function of the cosine of the angle of incidence α. The $cos\alpha$ term was expanded into a Taylor series of which only the first term was used to extract the factor 0.78. by expanding both in a Taylor series. Here only the first term was taken into account. The factor 0.78 obtained makes curves for different α overlap. The curves for proton and deuteron energy loss in silicon, both shown in figure 5.5, were calculated using the formalism from [59]:

$$\Delta E = E - \left(E^{\beta} - \frac{t}{C_R}\right)^{1/\beta} \tag{5.7}$$

with ΔE the deposited energy, E the energy before passage through the silicon, t the silicon thickness, C^R and β constants obtained from range tables [59]. The obtained result can be used for particle identification, but not for the energy determination as this information is lost in this procedure. The energy calibration factors and offsets were established for each plane separately by calculating the distance from each point to the theoretical curve and minimising the sum of these values. The following calibration factors and offsets were calculated according to the scheme below:

$$\text{plane } 1: \quad \Delta E_1 = a_0 \quad ADC_1 + a_1 \tag{5.8}$$

$$\text{plane } 2: \quad \Delta E_2 = b_0 \quad ADC_2 + b_1 \tag{5.9}$$

For each particle traversing the silicon layers we want to establish whether it was a proton or a deuteron and determine its energy before passing through the silicon detectors. Protons and deuterons can only be separated up to the point where the protons start to pass through the second layer, as from that point on the curves of the proton and the deuteron are too close to separate them considering the accuracy of the deposited energy. For the region where the curves are relatively far apart, for each point the shortest distance to

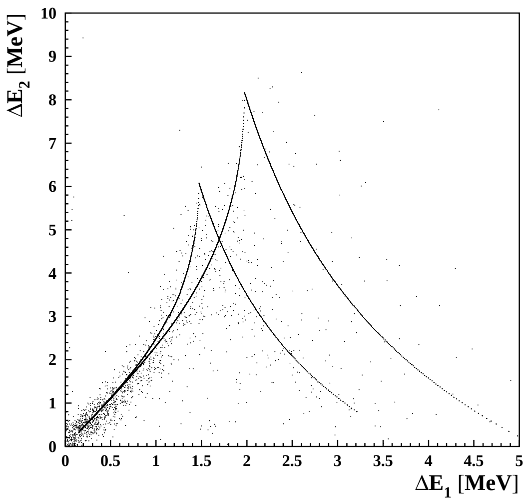

Fig. 5.5: Correlation between the energy loss in the top layer (ΔE_1) and the energy loss in the bottom layer (ΔE_2). The data have been calibrated using equations 5.8 and were corrected according to equation 5.6. The data are compared to the calculated energy-loss curves for protons and deuterons, with the upper curve for the deuterons and the lower one for the protons.

both curves is calculated. The nearest curve determines the particle type and immediately the energy of the particle before entering the silicon. However, as the events took place in the target-cell, the energy lost in passing through 75 μm aluminium has to be accounted for in the nucleon energy calculation. This is done by using eq. 5.7 again. The energy spectrum of the protons obtained in this way is used to extract the momentum distribution of the nucleons in deuterium, which is presented in the next section.

5.8 Nucleon momentum reconstruction

With the energy distribution of the protons from the deuterium target and the hydrogen target and the mass of the proton, the corresponding momentum distributions were calculated. They are presented in the top and middle panels of figure 5.6. The hydrogen distribution mainly consists of target fragmentation products from deep-inelastic scattering, since spectator protons cannot be produced on hydrogen. The deuterium distribution also contains the sought-after spectator protons. The method to obtain a normalised momentum distribution of these spectators is presented in the next subsection.

5.8.1 Absolute normalisation of the momentum distribution

To extract a normalised momentum distribution from the STC data, described as $N(x, Q^2, p, \theta)$, with p the recoil momentum and θ the polar angle of the recoil proton, we have to determine the following differential cross section

$$\frac{d\sigma}{dxdQ^2dpd\theta} = \frac{N(x, Q^2, p, \theta)}{\mathcal{L} \cdot \Delta x \Delta Q^2 \Delta p \Delta \theta}, \tag{5.10}$$

where $\mathcal{L}$ represents the integrated luminosity in [fm^{-2}], and Δv_i represents the bin size for each variable. The acceptance in x and Q^2 is governed by the HERMES spectrometer and is a complicated function which we represent by $V(x, Q^2)$. The acceptance of the STC is similarly expressed as $V_{STC}(p, \theta)$:

$$V_{STC}(p, \theta) = \int_{STC} d\vec{p} \approx p^2 \int_{STC} d\Omega = p^2 \cdot A_{STC}, \tag{5.11}$$

where the STC acceptance is assumed to be p-independent. Using a Monte Carlo simulation the angular acceptance of the STC, as expressed by the factor A_{STC}, can be estimated to be 1.2%. The simulation includes the target density distribution along z. Including these two acceptance functions the cross-section expression reads:

$$\frac{d\sigma}{dxdQ^2d^3p} = \frac{N(x, Q^2, p, \theta)}{\mathcal{L} \cdot V(x, Q^2) \cdot p^2 \cdot A_{STC}}. \tag{5.12}$$

The electron acceptance function, $V(x, Q^2)$, can be taken from the DIS cross section and its corresponding yield, $N^p_{incl.}$ on hydrogen

$$\frac{d\sigma_{DIS}}{dxdQ^2} = \frac{2\pi\alpha^2}{Q^2} \frac{1 + (1-y)^2}{x} F_2(x, Q^2) = \frac{N^p_{incl.}(x, Q^2)}{\mathcal{L} \cdot V(x, Q^2)} \tag{5.13}$$

where the last term describes the measured quantities. This can be used to extract $V(x, Q^2)$, which can then be inserted in eq. 5.12 to give:

$$\frac{d\sigma}{dxdQ^2d^3p} = \frac{N^d_{STC}(x, Q^2, |p|)/\mathcal{L}_{STC}}{N^p_{incl.}(x, Q^2)/\mathcal{L}_{incl.}} \cdot \frac{1}{p^2 \cdot A_{STC}} \frac{2\pi\alpha^2}{Q^2} \frac{1 + (1-y)^2}{x} F^p_2(x, Q^2). \tag{5.14}$$

In order to extract information on the proton momentum distribution in deuterium we make use of the expression for the cross section for DIS with the observation of a spectator [60]

$$\frac{d\sigma}{dxdQ^2d^3p} = \frac{2\pi\alpha^2}{Q^2} \frac{1 + (1-y)^2}{x} F^{tag}_2(x, Q^2) \cdot n(|p|). \tag{5.15}$$

Combining the last two equations yields:

$$F_2^{tag}(x,Q^2)\cdot n(|p|) = \frac{N^d_{STC}(x,Q^2,|p|)/\mathcal{L}_{STC}}{N^p_{incl.}(x,Q^2)/\mathcal{L}_{incl.}}\cdot\frac{1}{p^2\cdot A_{STC}}F_2^p(x,Q^2). \quad (5.16)$$

With this last equation it is possible to extract either $n(|p|)$ or $F_2^n\rfloor_{tag}/F_2^p$ from the data. The nucleon momentum distribution can be obtained by integrating over x and Q^2, if it is assumed that the total partonic number density is the same for the tagged and untagged structure function. It is seen that the absolute value of the nucleon momentum distribution in deuterium can be derived from the normalised yield for inclusive scattering and the normalised yield of the STC. As the luminosity enters twice it is sufficient to use relative measures of the luminosity as long as the same instrument is used for both.

5.8.2 Spectator proton momentum distribution

With all components now available we can use the energy distributions for the hydrogen and deuterium targets and calculate the momentum distributions. To obtain the pure spectator proton momentum distribution we have to subtract the momentum distribution of the fragmentation products as measured on the proton target from the deuterium distribution, assuming the large-angle fragmentation spectra for deuterium and hydrogen to be the same. In doing so, the distributions are normalised using the measured integrated luminosity on each target. This is expressed by the following equation.

$$n(p_{spec}) = \frac{N^d_{STC}(p) - \frac{\mathcal{L}^d_{STC}}{\mathcal{L}^p_{STC}}\cdot N^p_{STC}(p)}{\mathcal{L}^d_{STC}\cdot p^2\cdot A_{STC}}/(N^p_{incl.}/\mathcal{L}^p_{incl.}), \quad (5.17)$$

with $N^d_{STC}(p)$ and $N^p_{STC}(p)$ the number of events in the STC for deuterium and hydrogen targets binned in momentum, $\mathcal{L}^{p,d}_{STC,incl.}$ the integrated luminosity for hydrogen and deuterium for the STC events and the collected DIS events, and $N^p_{incl.}$ the total number of DIS events collected for hydrogen in HERMES run I. The result is presented in figure 5.6. The separate $N^d_{STC}(p)$ and $N^p_{STC}(p)$ spectra are shown in the upper and middle panels of figure 5.6.

The systematic uncertainty on $n(p)$ has an instrumental and a model-dependent component. The instrumental component is due to the uncertainty in A_{STC}, which we estimate to be 10%, the unmeasured efficiency of the STC, which is estimated to be 5%, and the neglected possible p-dependence of the acceptance, which is also estimated to be 5%. The model-dependent uncertainties stem from the assumed similarity of the fragmentation momentum distribution for hydrogen and deuterium and the assumed validity of equation 5.15. These uncertainties are hard to estimate without elaborate theoretical considerations and were assigned a fairly arbitrary 10% in this work. Taken together we arrive at a systematic uncertainty of about 16%. The result is shown in the lowest panel of figure 5.6. The first data point is

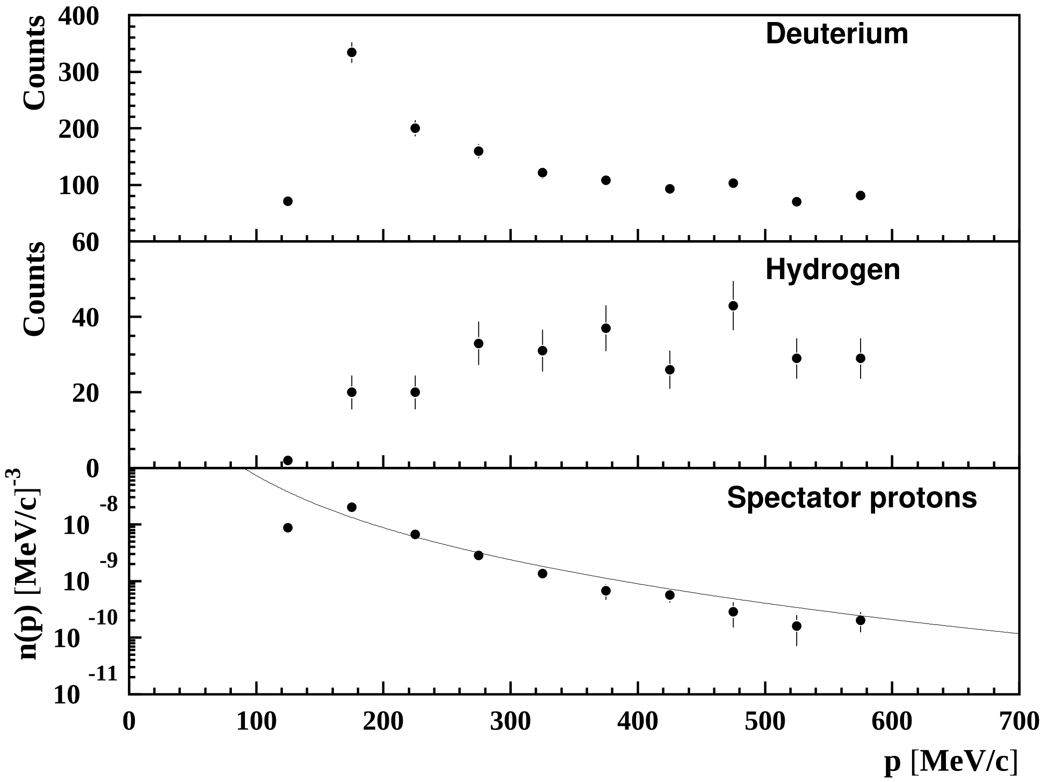

Fig. 5.6: Momentum distribution of deuterium (top panel), hydrogen (middle panel), and deuterium after the subtraction of the hydrogen data.

rather low compared to the other data because the STC acceptance is limited for the lowest momentum particles as we require the particles to traverse both detectors. They can be stopped in the first layer when they have an angle of incidence different from normal; only when they have a momentum of at least 125 MeV/c can they make it through both silicon detector layers for all possible impact angles. For lower momenta part of the proton spectrum will be stopped in the first layer at large angles.

The curve shown in figure 5.6 represents a parameterisation of the nucleon momentum distribution in the deuteron by Krautschneider [61]. This parameterisation is derived from $^2H(e,e'p)$ data measured in the quasi-elastic domain. It is surprising to see how well the STC data are described by the parameterisation, even on an absolute scale. This is remarkable as the scattering processes involved are different. In QES the electron scatters elastically off the proton which is subsequently detected, while in DIS the electron scatters off a quark in the neutron and the spectator proton is detected. This also implies that the final-state interaction processes are not necessarily the same in the two cases. For QES the knocked-out and recoiling nucleon will interact, while in DIS the particles produced in the current and target fragmentation processes may interact with the spectator proton. The latter processes were once believed to possibly cause a significant obstruction to the detection of spectator protons [62]. This is apparently not the case. The close correspondence of $n(p)$ derived from DIS and QES data proves that one can indeed use the spectator protons in DIS to tag neutron structure functions.

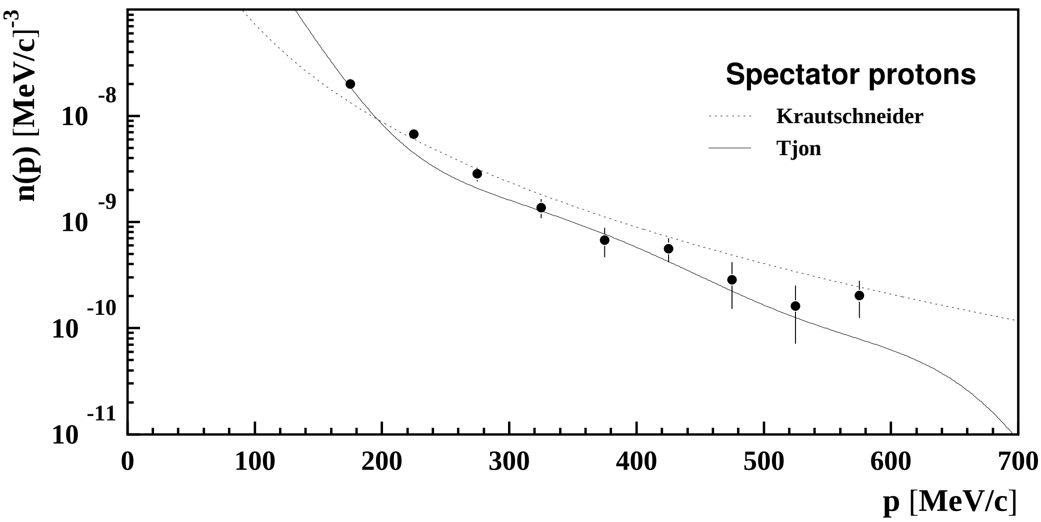

Fig. 5.7: Nucleon momentum distribution in deuterium as measured in DIS off deuterium. The systematic uncertainty is estimated to be 16%, except for the first bin where it is much larger.

It is of interest to compare the $n(p)$ data obtained with the STC to a relativistic plane-wave impulse approximation (PWIA) calculation of the deuterium wave function by Hummel and Tjon [63]. This comparison is presented in figure 5.7, where the calculation is seen to be in fairly good agreement with the experimental data. The agreement between data and the relativistic PWIA calculation implies that final-state interaction effects between spectators and target and current fragmentation products are small. As there can be no $\Delta(1232)$ or meson-exchange current contributions in DIS, we conclude that spectator data in DIS provide a surprisingly clean measurement of the nucleon momentum distribution in the deuteron. Future measurements with a large-angle recoil detector will enable a much more precise measurement of $n(p)$ using this method.

5.9 Extraction of $F_2^n\rfloor_{tag}/F_2^p$

Having proven that the spectator mechanism works very well in DIS, we can make one more step. It is now possible to use the detected spectator protons to tag events occurring on the neutron in deuterium and evaluate the structure function ratio $F_2^n\rfloor_{tag}/F_2^p$. Equation 5.16 was used in this procedure. In this case the equation is integrated over Q^2 and the result is plotted versus x for one momentum bin. The formula used to obtain $F_2^n\rfloor_{tag}/F_2^p$ is written as follows:

$$\frac{F_2^n\rfloor_{tag}(x,|p|)}{F_2^p} = \frac{N^d_{STC}(x,p)}{\mathcal{L}^d_{STC}\cdot p^2\cdot A_{STC}\cdot n(p)} / \frac{N^p_{DIS}}{\mathcal{L}^p_{incl.}}. \tag{5.18}$$

In the left panel of figure 5.8 the ratio $F_2^n\rfloor_{tag}/F_2^p$ is presented for the whole spectator momentum range, as presented in figure 5.6, i.e. from 125-625 MeV/c. The lowest momentum bin was left out of this analysis for the

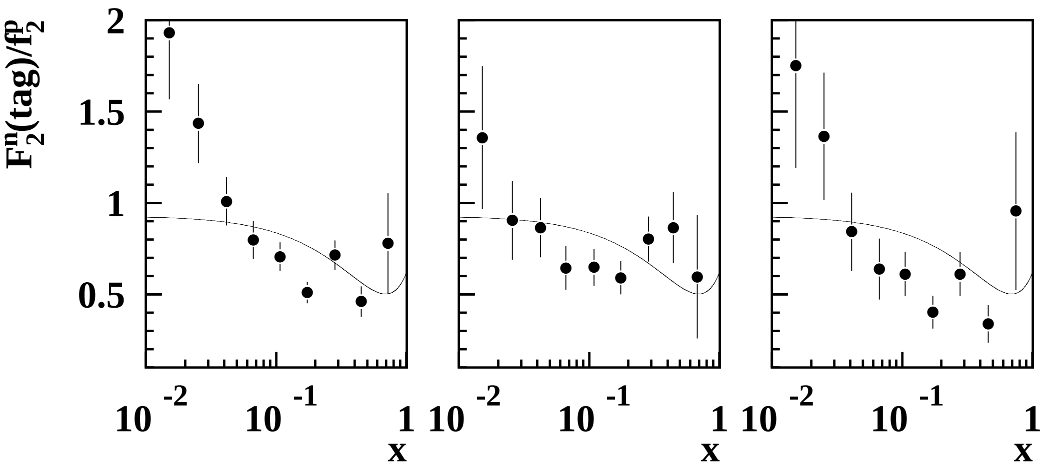

Fig. 5.8: The ratio $F_2^n\rfloor_{tag}/F_2^p$ presented for different spectator momentum ranges as mentioned in the text. The systematic uncertainty for the presented results is about 16%

reasons mentioned above. The curve corresponds to the fit of the HERMES σ^d/σ^p data discussed in section 4.6.1 and shown in figure 4.9. In this case the parameterisation was converted to F_2^n/F_2^p. In the middle panel the same quantity is presented, but for spectator protons with a momentum less than 225 MeV/c. These data are in agreement - albeit with poor statistics - with F_2^n/F_2^p as determined from the inclusive analysis. This demonstrates the feasibility of tagged structure function measurements in DIS. The right panel shows the $F_2^n\rfloor_{tag}/F_2^p$ ratio for the spectator protons with a momentum higher than 225 MeV/c. With the behaviour of $F_2^n\rfloor_{tag}/F_2^p$ available for the different momentum ranges we can investigate the relative behaviour of this ratio for the fast spectators relative to the slow ones. In figure 5.9 this ratio

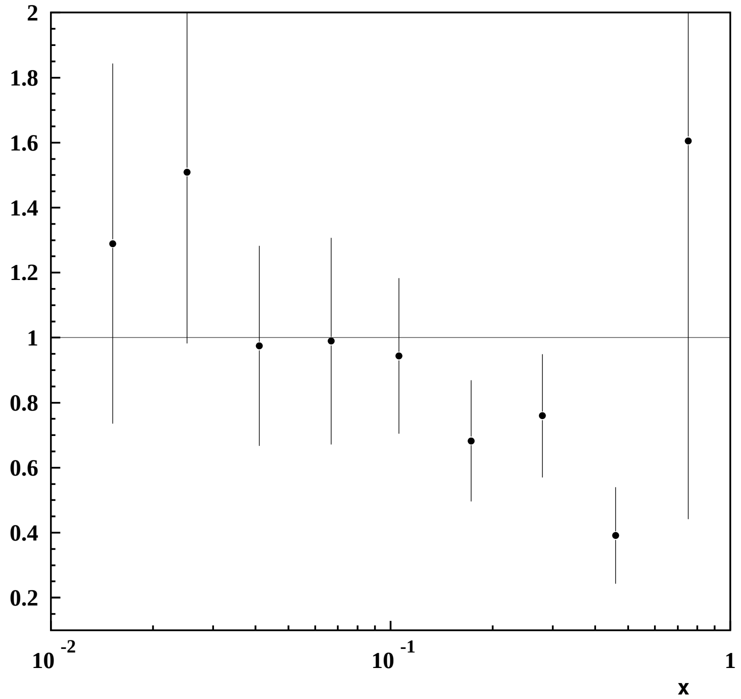

Fig. 5.9: The obtained ratio for $F_2^n\rfloor_{tag}/F_2^p$ with the high-momentum spectator protons (p > 225 MeV/c) divided by the ratio obtained for the low-momentum spectator protons (p < 225 MeV/c).

of $F_2^n\rfloor_{tag}/F_2^p$ for the fast protons over $F_2^n\rfloor_{tag}/F_2^p$ for the slower protons is presented. This shows that at higher x the ratio possibly drops below unity. It is remarkable that the possible deviation hinted at has the same shape as the EMC-effect, i.e. a reduction of strength in the x-domain between 0.3 and 0.7. These data can be interpreted - if confirmed by future high statistics data - as evidence for a p-dependence of the structure function ratio F_2^n/F_2^p. They support similar observations (with similar statistics) reported by the E745 experiment [4] based on deep inelastic neutrino scattering data using bubble chambers. However, in the E745 experiment no explicit measurement of the recoil proton momentum could be performed. Moreover, the interpretation of these neutrino data is obscured by the fact that it is assumed that the observed protons originate from correlated $n-p$ pairs in heavy nuclei. In this respect, the present experimental data represent a more direct observation of a possible p-dependence of $F_2(x)$, although statistically the data are of similar quality.

A full large solid angle recoil detector has to be constructed in order to provide high quality data on F_2^n/F_2^p for various momentum bins. Nevertheless, the first data on $F_2^n\rfloor_{tag}/F_2^p$ presented in this thesis already give a clear indication of the potential of this technique.

SUMMARY

In this thesis deep inelastic scattering (DIS) data on hydrogen and deuterium, obtained by the HERMES experiment at DESY, are presented. Two analyses are described. First, a high statistics study of deuteron - proton DIS cross section ratios yielding information on possible higher twist effects was discussed. Second, an exploratory study of the spectator proton mechanism in DIS, based on a newly constructed prototype silicon recoil-detector was presented. The study of deep inelastic scattering described in this thesis has yielded several results. One of the goals was to search for higher-twist effects at low and high x. This was accomplished by selecting 25 million events on hydrogen and deuterium from the HERMES run-I data and extracting the cross-section ratio of deuterium to hydrogen. The comparison of the cross-section ratios measured by HERMES showed a good agreement with data previously obtained at CERN and SLAC, both as a function of x and Q^2. In these comparisons it is clear that at similar values for x a region of lower Q^2 is probed at HERMES. As the cross section consists of two parts, namely a longitudinal and a transverse part, we studied besides the total cross section also the ratio of the two parts, R. The HERMES and NMC data are combined in a Rosenbluth-like fitting procedure to study the ratio, R, for deuterium relative to hydrogen. The extracted ratios are in good agreement with existing results and extend towards lower Q^2 at low x. Despite this extended kinematic domain, no evidence was found for higher-twist effects, which are different for the deuteron relative to the proton. To study a possible quark flavour dependence of higher-twist effects at high x, the cross-section ratio data of HERMES and NMC were again combined and compared to perturbative quantum chromodynamics (pQCD) next-to-leading-order (NLO) calculations, which are based on a recent parameterisation of parton distribution functions (PDFs). The obtained results were compared with earlier studies performed by NMC on the combined data of the BCDMS, SLAC and NMC experiments, using leading-order pQCD calculations based on older parton distribution functions. It can be concluded that both analyses are in agreement, but neither can provide unambiguous evidence for higher twist effects at high x due to the large uncertainties.

The inclusive DIS data on the proton and the neutron are also used

to determine the exhaustion of the Gottfried sum rule, which relates the difference between DIS off protons and neutrons to flavour asymmetries of the sea quarks. The present results are found to be in agreement with the only previous determination of the Gottfried sum rule by NMC. The agreement implies that the flavour asymmetry of the sea is not strongly dependent on Q^2.

The second (related) subject described in this thesis is an investigation of the possibility of recoil detection at HERMES. A prototype recoil detector, based on the use of silicon strip detectors, was built and installed underneath the internal target cell through which the HERA electron beam passes. It was operated successfully, thus proving that one can operate silicon detectors near a high intensity electron beam in ultra-high vacuum provided that proper precautions such as a Faraday cage, cooling and a radiation-hard readout chip are implemented. As it was a prototype with a limited acceptance rather few events were collected for physics analysis.

The data taken with the silicon test counter on both deuterium and hydrogen targets were used to extract the nucleon momentum distribution in the deuteron. This is the first time that such a measurement is reported, as previous neutrino experiments did not include an explicit momentum determination. Considering the uncertainties involved, the obtained distribution compares well with both the relativistic calculations and precise data obtained from quasi-elastic electron scattering (QES) experiments. This is a very interesting result as the processes in quasi-elastic scattering differ fundamentally from those in deep inelastic scattering. These results prove that the spectator mechanism is at work in DIS and that the final-state interactions are small and also that differences in final-state interactions between DIS and QES are relatively minor.

The measurement of the nucleon momentum distribution in DIS implies that it is possible to study tagged structure functions in DIS as well. For low spectator momenta the ratio $F_2^n\rfloor_{tag}/F_2^p$ was found to agree within large uncertainties with those obtained from the inclusive analysis. Moreover, these data enabled a search for a possible momentum dependence of the structure function ratio F_2^n/F_2^p. The ratio F_2^n/F_2^p for two different nucleon momentum regions was evaluated as a function of x. The ratio F_2^n/F_2^p for fast over slow spectator protons deviates from unity for x around 0.4, which can be interpreted as an indication of a nucleon momentum dependence of the structure function F_2. However, the present low statistics data do not enable us to draw definite conclusions. Nevertheless, the analysis shows the potential of a large-solid-angle recoil detector, which is under development at HERMES.

SAMENVATTING

In dit proefschrift worden resultaten gepresenteerd van experimenten waarmee de quarkstructuur van de materie is onderzocht. De metingen zijn gedaan door elektronen van zeer hoge energie te laten vertrooien aan de quarks in de kernen van zowel deuterium atomen (opgebouwd uit een proton en een neutron) als waterstof atomen (bestaande uit een proton). Deze experimenten werden uitgevoerd met het HERMES experiment bij de HERA elektron- en proton- versneller van het Duitse instituut voor hoge-energiefysica DESY in Hamburg. Twee analyses van de meetgegevens worden beschreven.

De eerste analyse is gebaseerd op metingen van de verhouding van de werkzame doorsnedes voor elektron-quark verstrooiing aan deuterium en waterstof. Deze verhouding van werkzame doorsnedes is gebruikt om te zoeken naar aanwijzingen voor het bestaan van correlaties tussen quarks. Deze mogelijke verschijnselen staan bekend onder de naam 'higher twist' effecten en worden gekarakteriseerd door de uitwisseling van een extra gluon tussen quarks tijdens het diep-inelastische verstrooiingsproces.

Bij het gebruik van meetgegevens verkregen op deuterium kan geen onderscheid gemaakt worden tussen verstrooiingsprocessen aan quarks in het proton of het neutron. Om diep-inelastische verstrooiing aan quarks in het neutron te isoleren moeten theoretische correcties toegepast worden die niet ondubbelzinnig bepaald kunnen worden. Enige tijd geleden is het idee gelanceerd om in dergelijke experimenten het 'toeschouwer-proton' van een interactie tussen het elektron en een quark in het neutron in deuterium waar te nemen. Hiermee kan vastgesteld worden dat de verstrooiing aan een quark in een neutron plaatsvond. De tweede analyse die in dit proefschrift wordt gepresenteerd omvat een studie, die uitgevoerd is om vast te stellen of dit 'toeschouwers-proton' model toegepast kan worden in diep-inelastische verstrooiing. Hiervoor is een prototype terugstoot (of 'recoil') detector gebouwd, waarmee deze 'toeschouwer-protonen' kunnen worden waargenomen. Door gebruik te maken van deeltjestellers gemaakt van silicium halfgeleiders kan de energie van deze protonen ook bepaald worden.

Voor de eerste analyse zijn 25 miljoen gebeurtenissen geselecteerd van de HERMES metingen die tussen 1995 en 2000 verkregen zijn. De verhouding van de werkzame doorsneden voor diep-inelastische verstrooiing aan deuterium en waterstof laat een goede overeenkomst zien met eerdere resultaten verkregen op CERN (NMC) en SLAC als functie van de kinematische variabelen x en Q^2. De variabele x representeert de fractie van de impuls van het nucleon die gedragen wordt door het geraakte quark. De variabele Q^2 is de gekwadrateerde 4-impuls van het virtuele photon dat uitgewisseld wordt tussen het elektron en het quark. Het verschil met eerdere metingen is dat bij gelijke waarde van x het HERMES experiment een gebied bestrijkt met lagere waarden van Q^2. Omdat de eerder genoemde quarkcorrelaties meer prominent zullen zijn bij lagere Q^2, kan een vergelijking van de HERMES data met eerdere metingen mogelijk aanwijzingen geven voor het bestaan van deze correlaties.

De gemeten werkzame doorsnedes bestaan uit een longitudinaal en een transversaal deel. In deze studie is niet alleen de som van beide delen bestudeerd, maar ook het verschil ΔR en de ratio R van de twee delen. De verhouding R is bij lage waarden van x gevoelig voor de eerder genoemde 'higher twist' effecten. Om de ratio R voor deuterium ten opzichte van de ratio R voor waterstof te bepalen zijn de HERMES en NMC metingen gecombineerd. In een procedure die verwant is aan de Rosenbluth methode, kan uit deze gecombineerde verzameling meetgegevens, de verhouding R^d/R^p bepaald worden. De verkregen waarden zijn in overeenstemming met 1, zoals ook al bleek uit eerdere resultaten. De huidige metingen strekken zich echter uit naar lagere Q^2 bij lage x. Ook in dit nieuw onderzochte kinematische domein zijn geen aanwijzingen gevonden voor 'higher twist' effecten die verschillend zijn voor deuterium t.o.v. waterstof.

Om te onderzoeken of er bij hoge x mogelijk quarkcorrelaties bestaan die verschillend zijn voor up en down quarks zijn de HERMES en NMC metingen ook samengevoegd in dit kinematische gebied. In dit geval zijn de data vergeleken met quantum chromodynamica (QCD) berekeningen, die gebaseerd zijn op parton-distributiefuncties die bepaald zijn bij zeer hoge bundelenergie waar 'higher twist' effecten verwaarloosd kunnen worden. Er kan geconcludeerd worden dat geen van beide resultaten eenduidige aanwijzingen leveren voor 'higher twist' effecten bij hoge x. Kennelijk zijn de quarkscorrelaties vrijwel gelijk in het proton en het neutron.

De metingen zijn tevens gebruikt om de Gottfried som te bepalen. De Gottfried som relateert het verschil van de werkzame doorsnedes voor diep-inelastische elektron-quark verstrooiing aan deuterium en waterstof aan de mogelijke verschillen tussen de bijdrage van de verschillende quarksmaken (up, down, strangeness en charm) aan de zee van quark-antiquark paren. De resultaten zijn in overeenkomst met eerder gevonden waarden voor de Gottfried som door NMC, waaruit al bleek dat de up-quarks minder prominent zijn in de quarkzee dan de down-quarks. De overeenkomst tussen de huidige bepaling van de Gottfried som en die van NMC impliceert dat de bijdrage van de verschillende quarks aan de zee niet sterk afhangt van Q^2.

Het tweede, gerelateerde, onderwerp beschreven in dit proefschrift omvat het onderzoek naar de mogelijkheid om toeschouwers-protonen te identificeren in diep-inelastische verstrooiingsexperimenten op deuterium. De gebouwde prototype detector is gebaseerd op het gebruik van stripdetectoren van silicium. Deze 'Silicium Test Counter' is direct onder de interne gasvormige trefplaat van het HERMES experiment geinstalleerd. Door deze open cel passeert de zeer intense HERA elektronenbundel. De detector werkte uitstekend, waarmee aangetoond is dat men nabij een intense elektronbundel in ultra hoog vacuum met succes silicium detectoren kan toepassen. Men dient echter wel een aantal voorzorgsmaatregelen te nemen, zoals een Faraday kooi om het geheel, koeling en het gebruiken van stralingsharde uitleeschips. Aangezien het een prototype detector was, zijn er slechts metingen beschikbaar van een beperkte statistiek. De metingen zijn gebruikt om de toepasbaarheid te onderzoeken van het proton-toeschouwermechanisme. De metingen zijn zowel verricht op deuterium als waterstof. Aangezien er geen toeschouwer-protonen van waterstof afkomstig kunnen zijn, leverde deze data een maat voor de achtergrond van zogenaamde quark fragmentatieproducten. Deze zijn afgetrokken van de deuterium data. Met de aldus opgeschoonde meetgegevens is de proton impulsverdeling in het deuterium bepaald. Dit is de eerste keer dat zulke resultaten verkregen zijn in diep-inelastische elektronverstrooiing. In eerdere neutrino geinduceerde experimenten, waarbij aanwijzingen gevonden werden voor het toeschouwersmechanisme, kon geen expliciete impulsbepaling uitgevoerd worden.

De beperkte statistiek in acht nemend is de verkregen impulsverdeling in goede overeenstemming met zowel relativistische berekeningen als nauwkeurige metingen verkregen uit quasi-elastische elektronverstrooiing aan deuterium. Dit is een interessant resultaat aangezien de elementaire interactie in quasi-elastische verstrooiing (aan het proton als geheel) verschillend is van de interactie in diep-inelastische verstrooiing (aan het quark) in het nucleon.

De resultaten laten tevens zien dat het 'toeschouwer-mechanisme' werkt in diep-inelastische verstrooiing en dat de wisselwerking tussen de uitgaande deeltjes klein is en weinig verschilt met de vergelijkbare eindtoestandswisselwerking in quasi-elastische verstrooiing. De meting van de nucleon impulsverdeling in diep-inelastische verstrooiing betekent dat het mogelijk is om gemerkte structuurfuncties in diep-inelastische verstrooiing te bepalen. Voor lage impuls van de 'toeschouwer-protonen' is de ratio $F_2^n\rfloor_{gemerkt}/F_2^p$ in overeenstemmming met de resultaten verkregen uit de eerder vermelde analyse, gebaseerd op inclusieve diep-inelastische verstrooiing. Tevens stellen deze metingen ons instaat om de mogelijke nucleon impulsafhankelijkheid van de structuurfunctie verhouding F_2^n/F_2^p te onderzoeken.

De ratio F_2^n/F_2^p is bepaald voor twee verschillende impulsgebieden als functie van x. De ratio van F_2^n/F_2^p voor snelle protonen gedeeld door dezelfde ratio van F_2^n/F_2^p voor relatief langzame protonen vertoont een afwijking van 1 bij x waarden van ongeveer 0.4. Dit kan geinterpreteerd worden als een indicatie voor een impulsafhankelijkheid van de structuurfunctie F_2. Omdat de huidige analyse gebaseerd is op zeer weinig meetgegevens is het niet mogelijk definitieve conclusies te trekken hierover. Maar wel is het potentieel van deze methode aangetoond, dat door de in ontwikkeling zijnde grote terugstootdetector bij HERMES kan worden uitgebuit.

DATA TABLES

Tables with the cross-scetion ratio σ^d/σ^p and the kinematic variables of interest for the analysis presented in chapter 5.

x	Q^2	ϵ	σ_d/σ_p	$\delta\sigma_d/\sigma_p$
0.0038	0.17	0.30	0.61	0.42
0.0043	0.19	0.30	1.01	0.11
0.0054	0.23	0.32	0.95	0.02
0.0066	0.27	0.35	0.96	0.01
0.0084	0.34	0.38	0.95	0.02
0.0096	0.41	0.33	0.93	0.04
0.0104	0.38	0.52	0.95	0.02
0.0117	0.45	0.46	0.95	0.00
0.0134	0.54	0.42	0.94	0.02
0.0145	0.61	0.33	0.89	0.09
0.0156	0.48	0.68	0.95	0.03
0.0167	0.56	0.62	0.95	0.00
0.0172	0.64	0.50	0.95	0.01
0.0183	0.74	0.41	0.95	0.02
0.0193	0.82	0.33	0.96	0.07
0.0212	0.58	0.76	0.96	0.02
0.0229	0.66	0.73	0.94	0.01
0.0242	0.75	0.67	0.95	0.00
0.0244	0.84	0.57	0.94	0.00
0.0253	0.94	0.50	0.96	0.01
0.0266	1.04	0.44	0.95	0.01
0.0278	1.14	0.39	0.95	0.02
0.0290	1.23	0.34	0.76	0.17
0.0298	1.30	0.29	1.05	0.37
0.0318	0.68	0.87	0.92	0.03
0.0336	0.76	0.85	0.93	0.01
0.0344	0.85	0.81	0.95	0.01

x	Q^2	ϵ	σ	δ
0.0346	0.94	0.76	0.94	0.01
0.0346	1.04	0.70	0.94	0.01
0.0346	1.14	0.62	0.94	0.01
0.0345	1.24	0.54	0.95	0.01
0.0349	1.34	0.46	0.94	0.01
0.0361	1.44	0.42	0.93	0.01
0.0374	1.54	0.38	0.93	0.02
0.0386	1.64	0.34	0.97	0.07
0.0395	1.71	0.31	0.98	0.16
0.0430	0.69	0.93	0.56	0.27
0.0437	0.77	0.91	0.90	0.02
0.0468	0.85	0.90	0.92	0.01
0.0484	0.95	0.89	0.92	0.01
0.0489	1.05	0.86	0.93	0.01
0.0491	1.14	0.83	0.93	0.01
0.0492	1.24	0.80	0.94	0.01
0.0491	1.34	0.76	0.93	0.01
0.0491	1.44	0.71	0.93	0.01
0.0491	1.54	0.66	0.93	0.01
0.0491	1.64	0.61	0.95	0.01
0.0492	1.74	0.55	0.94	0.01
0.0502	1.84	0.52	0.94	0.01
0.0515	1.94	0.49	0.93	0.01
0.0533	2.09	0.45	0.94	0.02
0.0558	2.28	0.39	0.97	0.26
0.0581	2.47	0.34	0.84	0.25
0.0597	2.61	0.29	0.82	0.17

x	Q^2	ϵ	σ	δ
0.0689	0.79	0.96	0.61	0.20
0.0663	0.87	0.95	0.90	0.02
0.0682	0.95	0.95	0.91	0.01
0.0689	1.05	0.94	0.92	0.01
0.0690	1.15	0.92	0.91	0.01
0.0694	1.24	0.91	0.91	0.01
0.0694	1.34	0.89	0.91	0.01
0.0694	1.44	0.87	0.93	0.01
0.0694	1.54	0.85	0.93	0.01
0.0694	1.64	0.83	0.93	0.01
0.0695	1.74	0.80	0.92	0.01
0.0694	1.84	0.78	0.93	0.01
0.0695	1.94	0.75	0.92	0.01
0.0694	2.09	0.70	0.92	0.01
0.0695	2.29	0.63	0.93	0.01
0.0694	2.49	0.54	0.93	0.01
0.0703	2.69	0.47	0.92	0.10
0.0729	2.89	0.43	0.91	0.03
0.0759	3.15	0.37	0.92	0.03
0.0797	3.50	0.29	0.72	0.53
0.0870	0.88	0.97	0.83	0.06
0.0878	0.96	0.97	0.92	0.02
0.0888	1.05	0.96	0.90	0.02
0.0892	1.15	0.95	0.89	0.02
0.0894	1.24	0.95	0.92	0.02
0.0894	1.34	0.94	0.91	0.02
0.0894	1.44	0.93	0.91	0.02
0.0894	1.54	0.92	0.90	0.01
0.0896	1.64	0.90	0.91	0.01
0.0894	1.74	0.89	0.91	0.01
0.0894	1.84	0.87	0.91	0.01
0.0895	1.94	0.86	0.92	0.01
0.0896	2.09	0.83	0.92	0.00
0.0896	2.29	0.80	0.91	0.00
0.0896	2.49	0.75	0.91	0.02
0.0897	2.69	0.70	0.92	0.00
0.0895	2.89	0.65	0.92	0.00
0.0898	3.23	0.55	0.92	0.00
0.0926	3.68	0.43	0.91	0.01
0.0974	4.08	0.36	0.91	0.04
0.1070	0.88	0.98	0.60	0.14
0.1082	0.97	0.98	0.87	0.02
0.1090	1.05	0.97	0.90	0.01
0.1093	1.15	0.97	0.91	0.00
0.1095	1.25	0.96	0.89	0.00
0.1095	1.35	0.96	0.90	0.00
0.1096	1.44	0.95	0.90	0.00
0.1096	1.54	0.94	0.91	0.00
0.1095	1.64	0.94	0.89	0.00

x	Q^2	ϵ	σ	δ
0.1095	1.74	0.93	0.89	0.00
0.1095	1.84	0.92	0.92	0.00
0.1097	1.94	0.91	0.91	0.00
0.1097	2.09	0.89	0.91	0.00
0.1096	2.29	0.87	0.90	0.00
0.1096	2.49	0.84	0.90	0.00
0.1096	2.69	0.81	0.91	0.00
0.1097	2.89	0.78	0.90	0.00
0.1096	3.23	0.71	0.90	0.00
0.1098	3.73	0.60	0.92	0.00
0.1109	4.20	0.49	0.91	0.01
0.1154	4.63	0.42	0.89	0.02
0.1452	0.87	0.99	0.59	0.42
0.1334	0.97	0.98	0.85	0.03
0.1364	1.06	0.98	0.86	0.01
0.1376	1.15	0.98	0.89	0.00
0.1384	1.25	0.98	0.89	0.00
0.1385	1.34	0.97	0.88	0.00
0.1384	1.45	0.97	0.89	0.00
0.1387	1.54	0.96	0.89	0.00
0.1386	1.64	0.96	0.88	0.00
0.1386	1.74	0.96	0.89	0.00
0.1389	1.84	0.95	0.89	0.00
0.1387	1.94	0.94	0.89	0.00
0.1386	2.09	0.94	0.89	0.00
0.1387	2.29	0.92	0.89	0.00
0.1388	2.49	0.91	0.90	0.00
0.1388	2.69	0.89	0.89	0.00
0.1389	2.89	0.87	0.88	0.00
0.1388	3.23	0.83	0.89	0.00
0.1387	3.73	0.77	0.90	0.00
0.1389	4.24	0.69	0.90	0.00
0.1404	4.73	0.61	0.89	0.00
0.1466	5.32	0.54	0.90	0.01
0.1578	6.05	0.47	0.90	0.09
0.1833	0.88	0.99	1.93	2.38
0.1732	0.97	0.99	0.84	0.08
0.1767	1.06	0.99	0.85	0.01
0.1778	1.15	0.99	0.87	0.00
0.1781	1.25	0.98	0.87	0.00
0.1786	1.35	0.98	0.87	0.00
0.1786	1.45	0.98	0.86	0.00
0.1787	1.54	0.98	0.88	0.00
0.1789	1.64	0.97	0.87	0.00
0.1789	1.74	0.97	0.87	0.00
0.1789	1.84	0.97	0.87	0.00
0.1787	1.94	0.97	0.87	0.00
0.1785	2.09	0.96	0.87	0.00
0.1786	2.29	0.95	0.88	0.00

x	Q^2	ϵ	σ	δ
0.1787	2.49	0.94	0.87	0.00
0.1791	2.69	0.94	0.87	0.00
0.1790	2.89	0.93	0.88	0.00
0.1789	3.23	0.91	0.87	0.00
0.1789	3.73	0.87	0.87	0.00
0.1790	4.24	0.83	0.87	0.00
0.1790	4.73	0.78	0.86	0.00
0.1798	5.44	0.69	0.87	0.00
0.1838	6.34	0.59	0.87	0.01
0.1958	7.08	0.54	0.77	0.06
0.2162	0.97	0.99	0.72	0.14
0.2213	1.07	0.99	0.83	0.02
0.2224	1.15	0.99	0.83	0.01
0.2225	1.25	0.99	0.85	0.00
0.2231	1.35	0.99	0.84	0.00
0.2228	1.45	0.98	0.85	0.00
0.2229	1.54	0.98	0.85	0.00
0.2231	1.64	0.98	0.86	0.00
0.2235	1.74	0.98	0.86	0.00
0.2234	1.85	0.98	0.86	0.00
0.2232	1.94	0.98	0.86	0.00
0.2233	2.09	0.97	0.85	0.00
0.2233	2.29	0.97	0.85	0.00
0.2231	2.49	0.96	0.86	0.00
0.2233	2.69	0.96	0.86	0.00
0.2232	2.89	0.95	0.86	0.00
0.2236	3.23	0.94	0.85	0.00
0.2234	3.73	0.92	0.86	0.00
0.2235	4.23	0.89	0.86	0.00
0.2234	4.74	0.86	0.84	0.00
0.2237	5.46	0.81	0.85	0.00
0.2251	6.44	0.73	0.85	0.00
0.2287	7.38	0.64	0.85	0.01
0.2425	8.14	0.61	0.81	0.04
0.2540	1.08	0.99	0.58	0.06
0.2606	1.16	0.99	0.85	0.02
0.2672	1.25	0.99	0.82	0.01
0.2725	1.35	0.99	0.84	0.00
0.2734	1.45	0.99	0.82	0.00
0.2732	1.54	0.99	0.83	0.00
0.2735	1.65	0.99	0.84	0.00
0.2731	1.74	0.98	0.85	0.00
0.2733	1.84	0.98	0.83	0.00
0.2735	1.95	0.98	0.82	0.00
0.2731	2.09	0.98	0.83	0.00
0.2733	2.29	0.98	0.83	0.00
0.2730	2.49	0.97	0.82	0.00
0.2736	2.69	0.97	0.85	0.00
0.2735	2.89	0.97	0.84	0.00

x	Q^2	ϵ	σ	δ
0.2734	3.23	0.96	0.83	0.00
0.2734	3.74	0.95	0.82	0.00
0.2736	4.23	0.93	0.84	0.00
0.2735	4.73	0.91	0.81	0.00
0.2735	5.46	0.88	0.82	0.00
0.2738	6.46	0.83	0.82	0.00
0.2742	7.43	0.76	0.83	0.01
0.2773	8.42	0.69	0.81	0.01
0.2921	9.16	0.67	0.81	0.05
0.3032	1.37	0.99	0.80	0.03
0.3088	1.45	0.99	0.85	0.01
0.3152	1.55	0.99	0.83	0.01
0.3217	1.65	0.99	0.81	0.01
0.3276	1.75	0.99	0.83	0.00
0.3324	1.85	0.99	0.81	0.00
0.3374	1.95	0.99	0.82	0.00
0.3442	2.09	0.99	0.81	0.00
0.3439	2.29	0.98	0.80	0.00
0.3434	2.49	0.98	0.81	0.00
0.3447	2.69	0.98	0.80	0.00
0.3438	2.89	0.98	0.80	0.00
0.3447	3.24	0.97	0.80	0.00
0.3438	3.74	0.96	0.80	0.00
0.3447	4.24	0.96	0.81	0.00
0.3443	4.74	0.94	0.80	0.00
0.3442	5.46	0.93	0.81	0.00
0.3443	6.47	0.89	0.81	0.00
0.3448	7.46	0.86	0.78	0.00
0.3478	8.44	0.81	0.79	0.01
0.3497	9.42	0.76	0.82	0.01
0.3712	10.35	0.75	0.84	0.02
0.3953	11.05	0.74	0.64	0.14
0.4443	2.09	0.99	0.79	0.00
0.4446	2.29	0.99	0.78	0.00
0.4438	2.49	0.99	0.76	0.00
0.4443	2.69	0.99	0.79	0.00
0.4452	2.89	0.98	0.77	0.00
0.4439	3.23	0.98	0.77	0.00
0.4444	3.74	0.98	0.79	0.00
0.4441	4.24	0.97	0.78	0.00
0.4438	4.73	0.96	0.76	0.00
0.4432	5.47	0.95	0.78	0.00
0.4454	6.47	0.94	0.78	0.00
0.4443	7.47	0.92	0.77	0.01
0.4450	8.45	0.89	0.76	0.01
0.4467	9.45	0.86	0.77	0.01
0.4451	10.46	0.82	0.74	0.01
0.4549	11.38	0.80	0.74	0.02
0.4846	12.22	0.80	0.84	0.09

x	Q^2	ϵ	σ	δ
0.5446	2.09	0.99	0.78	0.01
0.5445	2.29	0.99	0.77	0.01
0.5444	2.49	0.99	0.78	0.01
0.5461	2.69	0.99	0.77	0.01
0.5445	2.89	0.99	0.78	0.01
0.5443	3.24	0.99	0.77	0.00
0.5438	3.73	0.98	0.77	0.00
0.5437	4.24	0.98	0.74	0.01
0.5433	4.73	0.97	0.76	0.01
0.5441	5.47	0.97	0.77	0.01
0.5431	6.47	0.96	0.73	0.01
0.5422	7.48	0.94	0.76	0.01
0.5432	8.48	0.93	0.74	0.01
0.5434	9.46	0.91	0.73	0.01
0.5450	10.48	0.89	0.76	0.02
0.5444	11.46	0.86	0.78	0.03
0.5440	12.42	0.83	0.82	0.04
0.5844	13.29	0.83	0.63	0.08
0.6658	2.09	0.99	0.77	0.01
0.6650	2.29	0.99	0.76	0.01
0.6647	2.50	0.99	0.74	0.01
0.6631	2.69	0.99	0.76	0.01
0.6625	2.89	0.99	0.72	0.01
0.6635	3.23	0.99	0.74	0.00
0.6646	3.74	0.99	0.72	0.01
0.6619	4.24	0.98	0.72	0.01
0.6622	4.73	0.98	0.74	0.01
0.6596	5.47	0.98	0.74	0.01
0.6617	6.47	0.97	0.72	0.01

x	Q^2	ϵ	σ	δ
0.6609	7.46	0.96	0.73	0.01
0.6575	8.47	0.95	0.71	0.01
0.6576	9.49	0.94	0.75	0.02
0.6614	10.47	0.92	0.70	0.02
0.6582	11.44	0.91	0.75	0.03
0.6549	12.50	0.89	0.74	0.04
0.6644	13.43	0.87	0.69	0.04
0.6971	14.23	0.87	0.52	0.08
0.8021	2.09	0.99	0.73	0.01
0.8087	2.29	0.99	0.77	0.02
0.8102	2.50	0.99	0.75	0.02
0.8121	2.69	0.99	0.75	0.02
0.8134	2.89	0.99	0.75	0.02
0.8153	3.24	0.99	0.73	0.01
0.8205	3.73	0.99	0.72	0.01
0.8255	4.24	0.99	0.68	0.01
0.8232	4.73	0.98	0.79	0.02
0.8207	5.46	0.98	0.78	0.02
0.8282	6.47	0.98	0.72	0.02
0.8246	7.50	0.97	0.74	0.02
0.8271	8.45	0.96	0.71	0.03
0.8272	9.45	0.96	0.78	0.04
0.8240	10.43	0.95	0.74	0.04
0.8344	11.49	0.94	0.78	0.06
0.8135	12.51	0.93	0.64	0.06
0.8065	13.47	0.91	0.58	0.07
0.8348	14.46	0.90	0.85	0.13
0.8761	15.51	0.90	0.98	0.25

Table with the cross-scetion ratio σ^d/σ^p averaged over the x-bins and Q^2 for the analysis presented in chapter 5.

$\langle x \rangle$	Q^2	σ_d/σ_p	$\delta\sigma_d/\sigma_p$
0.0038	0.17	0.645	1.6553
0.0053	0.23	0.942	0.0954
0.0081	0.34	0.962	0.0246
0.0125	0.49	0.953	0.0131
0.0174	0.65	0.953	0.0103
0.0248	0.86	0.955	0.0061
0.0348	1.11	0.948	0.0055
0.0495	1.40	0.938	0.0036
0.0695	1.73	0.925	0.0037
0.0896	1.98	0.917	0.0037
0.1096	2.18	0.908	0.0029
0.1388	2.42	0.894	0.0021
0.1789	2.68	0.876	0.0022
0.2234	2.92	0.858	0.0020
0.2732	3.16	0.835	0.0023
0.3418	3.75	0.811	0.0020
0.4444	4.36	0.782	0.0028
0.5441	4.45	0.771	0.0037
0.6629	4.31	0.746	0.0041
0.8163	4.05	0.751	0.0070

BIBLIOGRAPHY

[1] M. Arneodo et al., *Accurate measurement of F_2^d/F_2^p and $R^d - R^p$.* Nucl. Phys. **B487**, 3 (1997), hep-ex/9611022.

[2] L.W. Whitlow, *Deep inelastic structure functions from electron scattering on hydrogen, deuterium and iron at* $0.6\ GeV^2 \leq Q^2 \leq 30\ GeV^2$. Ph. D. Dissertation, Stanford University, Stanford CA, USA, Report SLAC-0357, (1990).

[3] U.K. Yang and A. Bodek, *Studies of higher twist and higher order effects in NLO and NNLO QCD analysis of lepton nucleon scattering data on F_2 and $R = \sigma_L/\sigma_T$.* Eur. Phys. J. **C13**, 241 (2000).

[4] T. Kitagaki, *Results from FNAL E745 on neutrino-nucleus interactions (EMC effect and hadron formations),* in *Electronuclear Physics with Internal Targets*, p. 95. (1989).

[5] J.J. Aubert et al., *The ratio of the nucleon structure function F_2^N for iron and deuterium.* Phys. Lett. **B123**, 275 (1983).

[6] R. Kaiser et al., *A Large Acceptance Recoil Detector for HERMES*, Internal HERMES report 01-017, DESY, (2001).

[7] C.G. Callan and D.J. Gross, *High-energy electroproduction and the constitution of the electric current.* Phys. Rev. Lett. **22**, 156 (1969).

[8] A. Bodek et al., *Experimental studies of the neutron and proton electromagnetic structure functions.* Phys. Rev. **D20**, 1471 (1979).

[9] V.N. Gribov and L.N. Lipatov, *Deep inelastic ep scattering in perturbation theory.* Sov. J. Nucl. Phys. **15**, 438 (1972);
Yu.L. Dokshitzer, *Calculation of the structure functions for deep inelastic scattering and e^+e^- annihilation by perturbation theory in Quantum Chromodynamics [in Russian].* Sov. Phys. JETP **46**, 641 (1977);
G. Altarelli and G. Parisi, *Asymptotic freedom in parton language.* Nucl. Phys. **B126**, 298 (1977).

[10] M. Virchaux and A. Milsztajn, *A measurement of α-s and higher twists from a QCD analysis of high statistics F_2 data on hydrogen and deuterium targets.* Phys. Lett. **B274**, 221 (1992).

[11] F.E. Close, *$\nu\mathcal{W}_2$ at small ω' and resonance form factors in a quark model with broken SU(6).* Phys. Lett. **43B**, 422 (1973).

[12] R. Carlitz, *SU(6) symmetry breaking effects in deep inelastic scattering.* Phys. Lett. **58B**, 345 (1975).

[13] F.E. Close and A.W. Thomas, *The spin flavor dependence of parton distribution functions.* Phys. Lett. **B212**, 227 (1988).

[14] G.R. Farrar and D.R. Jackson, *Pion and nucleon structure functions near $x = 1^*$.* Phys. Rev. Lett. **35**, 1416 (1975).

[15] S.J. Brodsky, M. Burkardt, I. Schmidt, *Perturbative QCD constraints on the shape of polarized quark and gluon distributions.* Nucl. Phys. **B441**, 197 (1995), hep-ph/9401328.

[16] W. Melnitchouk and A. W. Thomas, *Neutron / proton structure function ratio at large x.* Phys. Lett. **B377**, 11 (1996), nucl-th/9602038.

[17] V.V. Burov, A.V. Molochkov, G.I. Smirnov, *Evolution of the EMC effect in light nuclei* (1998), hep-ph/9809541.

[18] G.I. Smirnov, *On the universality of the x and A-dependence of the EMC effect and its relation to parton distributions in nuclei.* Phys. Lett. **B364**, 87 (1995), hep-ph/9512204.

[19] J. Gomez et al., *Measurement of the A-dependence of deep inelastic electron scattering.* Phys. Rev. **D49**, 4348 (1994).

[20] Ackerstaff, K. et al., *Nuclear effects on $R = \sigma_L/\sigma_T$ in deep inelastic scattering.* Phys. Lett. **B475**, 386 (2000), hep-ex/9910071.

[21] The HERMES Collaboration, *Technical Design Report*, Technical Report DESY-PRC 93/06, DESY, (1993).

[22] K. Ackerstaff et al., *The* HERMES *spectrometer.* Nucl. Instr. & Meth. **A417**, 230 (1998), hep-ex/9806008.

[23] A. Sokolov and I.M. Ternov, *On polarization and spin effects in the theory of synchrotron radiation.* Sov. Phys. Doklady **8**, 1203 (1964).

[24] J.S. Dunham et al., *Polarised gas jet targets.* NIM **A219**, 46 (1984).

[25] N.Koch, *A study on the Production of Intense Cold Atomic beams for Polarized Hydrogen and Deuterium Targets.* Ph.D. Thesis, Friedrich-alexander Univ., Erlangen-Nürnberg, (1999).

[26] C. Baumgarten *et al.*, *An atomic beam polarimeter to measure the nuclear polarization in the HERMES gaseous polarized hydrogen and deuterium target* (2001). DESY-01-078.

[27] W. Wander, *Reconstruction of High Energy Scattering Events in the HERMES Experiment.* Ph.D. Thesis, Friedrich-Alexander-Univ. Erlangen-Nuernberg, (1997). DESY-HERMES 97/031.

[28] J. Blouw et al., *Design and performance of a large microstrip gas tracker for hermes.* Nucl. Instrum. Meth. **A434**, 227 (1999).

[29] S. Bernreuther et al., *The HERMES back drift chambers.* Nucl. Instrum. Meth. **A416**, 45 (1998), hep-ex/9803005.

[30] H. Avakian et al., *Performance of the electromagnetic calorimeter of the HERMES experiment.* Nucl. Instrum. Meth. **A417**, 69 (1998), hep-ex/9810004.

[31] D. Ryckbosch, *The HERMES RICH detector.* Nucl. Instrum. Meth. **A433**, 98 (1999).

[32] U.K. Yang and A. Bodek, *Parton distributions, d/u, and higher twist effects at high x.* Phys. Rev. Lett. **82**, 2467 (1999), hep-ph/9809480.

[33] T. Gousset and H.J. Pirner, *The ratio of gluon distributions in Sn and C.* Phys. Lett. **B375**, 349 (1996), hep-ph/9601242.

[34] I. Niculescu et al., *Experimental verification of quark hadron duality.* Phys. Rev. Lett. **85**, 1186 (2000).

[35] E.D. Bloom and F.J. Gilman, *Scaling, duality, and the behavior of resonances in inelastic electron-proton scattering.* Phys. Rev. Lett. **25**, 1140 (1970);
E.D. Bloom and F.J. Gilman, *Scaling and the behavior of nuclear resonances in inelastic electron-nucleon scattering.* Phys. Rev. **D4**, 2901 (1971).

[36] M. Beckmann, *Extraction of Polarised Quark Distribution of the Nucleon from Deep Inelastic Scattering at the HERMES Experiment.* Ph.D. Thesis, University of Freiburg, (1999).

[37] Y. Gaerber, *Messung der Proton-Spinstrukturfunktion* g_1 *bis zu kleinstmoeglichen Bjorken-x mit dem HERMES-Experiment.* Ph.D. Thesis, University of Berlin, (2001).

[38] M. Vincter, *private communications* (unpublished).

[39] D.Yu. Bardin, C. Burdik, P.Ch. Christova, T. Riemann, *Electroweak radiative corrections to deep inelastic scattering at HERA. charged current scattering.* Z. Phys. **C44**, 149 (1989).

[40] I. Akushevich et al., *Radiative corrections to the structure function ratios* F_2^n/F_2^p, F_2^{He}/F_2^d *and* F_2^N/F_2^d (1999).

[41] P. Amaudruz et al., *A reevaluation of the nuclear structure function ratios for D, He, Li-6, C and Ca.* Nucl. Phys. **B441**, 3 (1995), hep-ph/9503291.

[42] A. Miller, *Applying radiative corrections to ratios of cross sections of deeply inelastic scattering.* HERMES Internal note (2002).

[43] M. Vincter, *A determination of* $F_2^n/F_2^p(x)$ *from the 1996 HERMES Unpolarised Data* (unpublished). (1997).

[44] L.W. Whitlow, E.M. Riordan, S. Dasu, S. Rock, A. Bodek, *Precise measurements of the proton and deuteron structure functions from a global analysis of the SLAC deep inelastic electron scattering cross-sections.* Phys. Lett. **B282**, 475 (1992).

[45] P. Amaudruz et al., *The ratio* $F_2(n)$ / $F_2(p)$ *in deep inelastic muon scattering.* Nucl. Phys. **B371**, 3 (1992).

[46] A. Brüll, *Die Strukturfunktionen des Nukleons bei kleinen Werten von x.* Ph.D. Thesis, University of Freiburg, (1993).

[47] L.W. Whitlow, S. Rock, A. Bodek, E.M. Riordan, S. Dasu, *A precise extraction of* $R = \sigma_L/\sigma_T$ *from a global analysis of the SLAC deep inelastic e p and e d scattering cross-sections.* Phys. Lett. **B250**, 193 (1990).

[48] M. Botje, *A QCD analysis of HERA and fixed target structure function data.* Eur. Phys. J. **C14**, 285 (2000), hep-ph/9912439.

[49] A.D. Martin, J.W. Stirling, R.G. Roberts, *Parton distributions for low* Q^2. Phys. Rev. **D51**, 4756 (1995), hep-ph/9409410.

[50] M. Arneodo et al., *A reevaluation of the Gottfried sum.* Phys. Rev. **D50**, 1 (1994).

[51] *Proceedings of the '95-'96 workshop on future physics at HERA, working group on light and heavy nuclei at HERA - part 2,* in *Future Physics with Light and Heavy Nuclei at HERMES.* (1996).

[52] Pegasys collaboration, *Proposal for the 'PEP gasjet spectrometer system'* (1988).

[53] L.L. Frankfurt and M.I. Strikman, *Hard nuclear processes and microscopic nuclear structure.* Phys. Rept. **160**, 235 (1988).

[54] M. Amarian et al., *Proposal for the development of recoil detection at HERMES* (1997).

[55] O. Postma, *Vacuum outgassing measurements for the HERMES vertex detector*, NIKHEF report MT 99-03, NIKHEF, (1999).

[56] D. Pitzl, *private communications* (unpublished).

[57] R. Horrisberger and D. Pitzl, *A novel readout chip for silicon strip detectors with analog pipeline and digitally controlled analog signal processing.* Nucl. Inst. Meth. **A326**, 92 (1993).

[58] K.T. Fiedler, *Identification of Spectator Nucleons at HERMES.* Ph.D. Thesis, University of Erlangen, (2001).

[59] H. Bichsel and C. Tschalaer, *A range-energy table for heavy particles in silicon.* Nuclear Data A **3**, 343 (1967).

[60] W. Melnitchouk, M . Sargsian, M.I. Strikman, *Probing the origin of the EMC effect via tagged structure functions of the deuteron.* Z. Phys. **A359**, 99 (1997), nucl-th/9609048.

[61] F. krautschneider, *Photoproduction of negative pi-mesons between 900-MeV and 1800-MeV.* Ph.D. Thesis, Bonn, (1976).

[62] S. Simula, *Semi-inclusive deep inelastic electron scattering off the deuteron and the neutron to proton structure function ratio.* Phys. Lett. **B387**, 245 (1996), nucl-th/9605024.

[63] E. Hummel and J.A. Tjon, *Relativistic description of electron scattering on the deuteron.* Phys. Rev. **C49**, 21 (1994), nucl-th/9309004.

ACKNOWLEDGEMENTS

The fact that this thesis was actually completed would really not have been possible without the help of the following people, who helped me out with all the typing to be done in the long period I was not able to use my hands.

Johan, Ernst-Jan, Ivo, Rutger, Antonello, Erika and Andreas,
bedankt, grazie, danke!

Gerard, dat ik, ondanks alles, als eerste jou mijn promotor mag noemen is voornamelijk dankzij jouw oneindige optimisme en zeker ook de steun die je mij hebt geboden om dit proefschrift te kunnen af te ronden.

Jos, jouw doorzettingsvermogen en oog voor detail zijn voor mij een voorbeeld geweest waar niet alleen mijn proefschrift beter van is geworden.

Peter, de discussies met jou over de fysica hebben mij een ander perspectief geboden om mijn proefschrift te vervolmaken.

Michel, Holger, Peter, Beni and Othmane, my post-docs in order of appearance, with each of you I worked only shortly but fruitfully.

De ontwikkeling van de STC en de lambda wielen was een enorme uitdaging, met pieken en dalen, maar door de positieve inzet van alle betrokkenen van de mechanische en electronische afdeling was het altijd plezierig samen te werken als ook te eten en te drinken. Arnold, Curs, Michiel, Martin Doets, Joop, Yke, Peter, Martin van Beuzekom, Rob, Onno, Edwin en Erwin hartstikke bedankt!

Incontrare italiani e viaggiare qualche volte in Italia mi ha fatto capire che l'Italia mi ha preso un pezzo di cuore. Vorrei percio ringraziare tutte le persone che hanno contribuito facendomi conoscere la lingua, l'apprezzamento per la cucina e il modo di vivere. Erika, Chiara, Lara, Diana, Guia, Alessandra, Valeria, Pasquale, Davide, Fabio, Nicola Bianchi ,Marcello, Antonio, Antonello, Luigi, Nicola Neri, Alessandro, Peppone, Paolo, e Riccardo, grazie!

At DESY I had the pleasure to meet many nice people with whom my time spent in Hamburg passed very quickly. Many memories of massive food intake sessions come to mind featuring, among others, Greg, Steve, Jim, Maurice, Tom, Felix, Marc, Brendan, James, ... On a more serious note I'd like to thank the people who have been working on parts of my analyses and especially the understanding of the radiative corrections and the unfortunate complex problems which arose. Antje, Erika, Andy, Manuella, Henk, Louk and Gerard, thanks.

The HERMES group of PhD students at NIKHEF is a mixture of several nationalities, which made it all the more interesting to work and hang out with you. Armen, Chiara, Erika, Andreas, Vladas, David, Vanessa and Tim (for obvious reasons), Michiel, Paul, Jeroen, Machiel, Johan.

The other PhD students with whom the troubles of finishing a PhD were shared over many a dinner, movie, concert or games of AJAX. Tino, Ernst-Jan, Ivo, Niels, Rutger, Jaap, Martin, Bram, Aart, Rene, Joana, Mieke, Antonello, Maarten, Erika, Chiara, David,...
Thank you all and good luck to those still to finish up.

Physical sense, jullie visie op RSI heeft me in staat gesteld om mijn handen weer te gebruiken. Allemaal enorm bedankt, maar vooral Marieke die mij lang heeft begeleid om eigenlijk alles opnieuw te leren.

De laatste woorden zijn voor mijn ouders,... pa, ma bedankt voor alles!